Study of the Shadow of the Moon in Very High Energy Cosmic Rays with the Milagrito Water Cherenkov Detector

by

Morgan O'Hagan Wascko

B.A. (University of Chicago) 1993
M.S. (University of California, Riverside) 1996

A dissertation submitted in partial satisfaction of the
requirements for the degree of
Doctor of Philosophy

in

Physics

in the

GRADUATE DIVISION
of the
UNIVERSITY of CALIFORNIA at RIVERSIDE

Committee in charge:

Professor Benjamin Shen, Chair
Adjunct Professor Cyrus M. Hoffman
Professor Allen Zych

2001

The dissertation of Morgan O'Hagan Wascko is approved:

Chair — Date

Date

Date

University of California at Riverside

2001

Study of the Shadow of the Moon in Very High Energy Cosmic Rays with the Milagrito Water Cherenkov Detector

by

Morgan O'Hagan Wascko

Abstract

Study of the Shadow of the Moon in Very High Energy Cosmic Rays with the Milagrito Water Cherenkov Detector

by

Morgan O'Hagan Wascko

Doctor of Philosophy in Physics

University of California at Riverside

Professor Benjamin Shen, Chair

Milagrito was the first extensive air shower array sensitive to showers initiated by primary cosmic rays with energy below 1 TeV. The shadow of the moon observed in cosmic rays can be used to search for the presence of antimatter in the cosmic ray flux, as well as to study systematic pointing shifts and measure the angular resolution of EAS arrays. The moon shadow, offset from the nominal position, has been observed at the 10.2σ level with Milagrito. This is used to study and correct a systematic pointing error found in the Milagrito data. The average angular resolution of Milagrito is estimated to be $0.90° \pm 0.11°$. An upper limit on the $\overline{p}/p$ ratio in $\sim$ 3TeV cosmic rays is calculated to be 17%, at the 95% confidence level.

Professor Benjamin Shen
Dissertation Committee Chair

For my family.

Contents

List of Figures

List of Tables

Acknowledgements

As I come to end of my graduate career, tragically cut short as it was by the demands of the outside world, I look back on my time in Riverside and Los Alamos and I see a chain of great people that helped me get to this point. I don't think I can ever repay everything I've been given by these kind folk, but perhaps finishing up and putting their names here to sit on a shelf in effective anonymity for ages to come will be a good start.

First of all, I don't think I would have managed to become a grad student at all without the help of Rene Ong. Rene's advice and good humor while I was applying for grad school, for the second time, was invaluable.

Once in Riverside I was very lucky, as all of his students are, to have Jose Wudka as a professor. There is absolutely no way that I could have passed the comprehensive exams without Jose's help, and I don't know if I can ever repay that. Just as important as that help, though, were the pitchers of Guinness he bought on Friday nights at The Barn. And I do hope to repay that, as many times as possible.

I was also lucky to find myself the T.A. for Gordon Van Dalen when I first arrived in Riverside. In addition to being one of the wisest men I've ever met, he was the one who first told me about Milagro, and made damn sure that I attended a colloquium on the detector that Cy Hoffman gave during my first year in Riverside. Knowing my attendance record, that did take a bit of extra effort. During my second year in Riverside, Gordon's advice and especially his anecdotes about his days as a student

helped put my adventures in perspective.

I know that some graduate students feel plagued to have one advisor. I find myself in the unique position of being happy to have two. Ben Shen's patience with my pace has been more than I could have hoped for. And while it may have been burdensome to him, it has been great for me because each additional day that I spent as a student has been one more day that I was allowed to work with Cy.

I cannot easily express how important it has been for me to have worked for Cy Hoffman. Personally, he is a kind and generous man, but that does not make him ineffective in his role as a leader of the collaboration. He is very disciplined, far more so than I am, and his example has been very important in my development as a physicist, and as a person. Contrary to what he may believe, it is the example that he sets himself that motivates me, not the gentle kicks in the ass that he has so graciously offered me over the past three years. And his twisted sense of humor, so close to my own, has always made working with him enjoyable. Professionally, I cannot see how Cy could be a better physicist. He approaches every problem in the same way: in simple steps, attacking the fundamental aspects first, with frequent stops to look at the big picture. He's helped me more than anyone else to learn how to actually do physics, which turns out to be more difficult than it might appear at first. I remember the first time I felt like a real physicist was when I won my first argument about the behavior of the moon shadow with Cy. His response was classic: "Holy shit," he mused, "could it be that you're *right*?" [1]

The Milagro Collaboration is great group of individuals, and I feel very lucky to have been thrown into their lot. Everything I know about Milagro itself, the hardware, the software, the simulations, I learned from our postdocs. As far as I'm concerned, the salad days of Milagrito were the early days when Rich Miller, Andy Smith, and Stefan Westerhoff all shared an office with no door. This meant that they were unable to keep me out, and I poked my head in there at least twice an hour every day for nearly a year with some question. I am very grateful that they answered the dumb ones just as kindly and they answered the hard ones. An office full of postdocs with no door on it is a resource that every grad student should be lucky enough to find. The fact that it was those three in particular was especially lucky for me. Julie McEnery, a.k.a. Dr. McEnergy, brought a fresh breath of enthusiasm into Los Alamos, improving the work environment and the play environment for me.

I don't think anyone can ever say enough about the efforts of Scott Delay. He is the glue that holds the entire operation together; without his MacGyver-like ability to throw together working parts from what was thought to be trash, Milagro would vanish in a puff of smoke. And he's one of the nicest guys you could ever hope to meet, which makes him all the more amazing.

My fellow students have also been a great help to me, especially Joe McCullough and Robert Atkins. Take heart, gentlemen, and find inspiration in my example. If I can get a Ph.D., then you certainly can! The last month or so, while working until all hours of the night, these trailers have felt especially deserted without Kelin sitting

down the hall working on his. I've missed the late night discussions of everything from Chinese history to how beer is brewed. And if I live to 1000, I'll never forget Tom Yang. Tom was especially helpful and generous for the short time that we overlapped here in Los Alamos, and it was a loss to me when he left.

Great thanks go to Gus Sinnis, Bob Ellsworth, and Allen Mincer for many helpful discussions of the moon shadow.

My life over the past few years would have been a dismal bore here without the influence of a very great group of friends. Dave and Enrico made every day better and have been sorely missed. The same goes for Rob and Joe. I understand that you guys all wanted to be with your wives (except for you, Dave—HA HA!), but what about my feelings? Kim, my "wife", has helped me through the lean years of grad school with more than just food and beer, which were given freely and copiously. She's always been a great friend to have, during the fun times and the not-so-fun times. Julia is, well, she just plain rules in every way, and I'm damn glad to have her in my karass. I've been very lucky to have Jen around to help keep my feet planted firmly on the ground during the past few months of thesis writing. You, my dear, are the best. In summary: `<http://www.coolest.chicks.ever>`

And then there's the thread. It might be said that I would have been more productive without their influence, but it's also likely that without those magnificent bastards my life story would end with the phrase "and then he turned the gun on himself." Warm...

My last thanks are my most heartfelt, and they go to my family. I'm not exactly a word-smith, and I find it difficult to properly articulate just how wonderful my family is, and how much it means to me to have them. My mom and my sister and I have been through quite a bit together, and the only thing that made it all worthwhile to me was their love. I'm the luckiest guy ever because my all-time desert-island favorite people in the whole world and my family are the same people. Just imagine how much better the holidays are because of this! Every late night that I ever spent in front of this computer, and every time I re-made the same damn plot over again, was worth it because I can now tell them I made it.

Chapter 1

Introduction

The earth is under continuous bombardment by ionizing radiation from outside the solar system. This phenomenon is called cosmic radiation, or more commonly cosmic rays. These "rays" are now known not to be rays at all, but high energy subatomic particles. Nearly nine out of every ten of these cosmic rays are protons, with ionized Helium nuclei comprising most of the last tenth, and spare amounts of heavier nuclei and gamma rays making up the rest of the flux.

These charged particles swarm about the galaxy, their paths bent by the galactic magnetic fields to keep them circling inside the galaxy. Most of them follow such paths for millions of years, and some of them escape galactic confinement, hurtling off into intergalactic space. But some of them eventually find their way into our solar system, and some of these enter the earth's atmosphere, allowing us to study them.

This work describes a study of the shadow of the moon in very high energy cos-

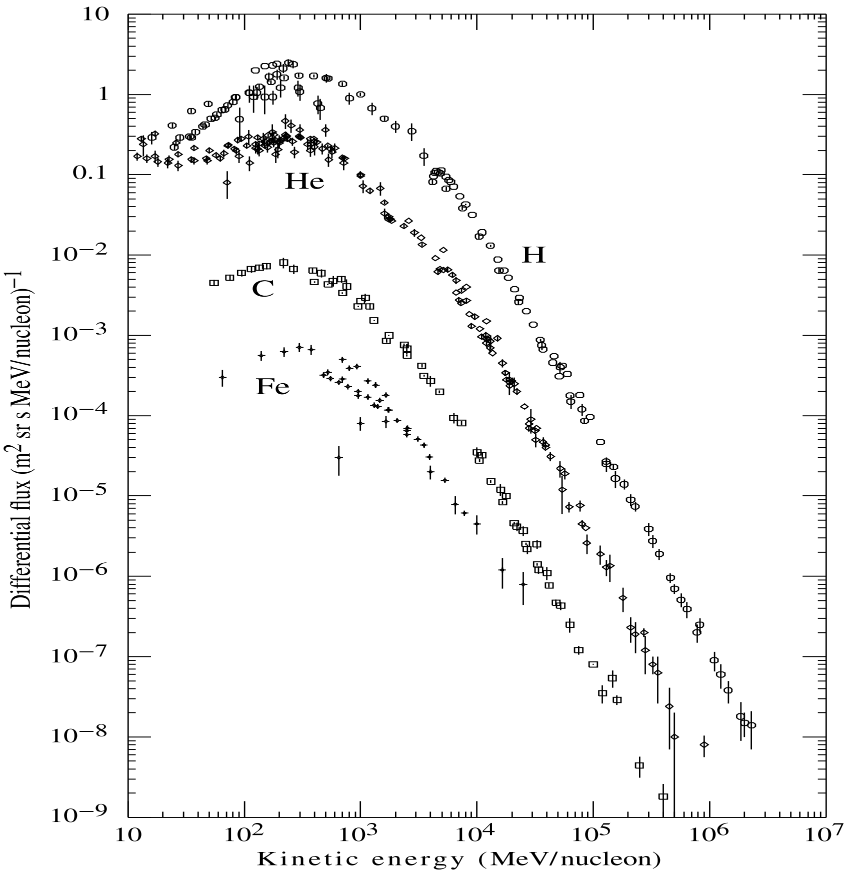

Figure 1.1: The cosmic ray energy spectrum, measured at solar minimum by [2]. The plot is taken from [3].

mic rays with the Milagrito Water Cherenkov Detector. The moon shadow is used to find the angular resolution of the detector and to study systematic shifts in its absolute pointing ability. The moon shadow is also used to make a measurement of the magnetic rigidity of the detected cosmic rays, and to search for antiprotons in cosmic rays. The first chapter discusses the physics issues involved in these studies, and the second describes the Milagrito Water Cherenkov detector. Chapter 3 is a discussion of the simulated data and results, and Chapter 4 describes the reconstruction of the data and study of the moon shadow. Chapter 5 discusses a maximum likelihood analysis method used on the moon shadow, and applies this technique to measure the magnetic rigidity of the cosmic rays detected by Milagrito and the search for antimatter. Chapter 6 describes a brief analysis of the shadow of the sun using the same techniques, and Chapter 7 summarizes the work and details the conclusions that can be drawn, and the potential for future measurements.

1.1 Cosmic Rays

Cosmic radiation was discovered by Hess [4] in 1912. It had been known for nearly a decade that there was ionizing radiation naturally present in the air, as evidenced by the slow discharge of electroscopes. Though initially thought to stem from the decay of radioactive elements in the earth, this ionizing radiation was demonstrated to come from above when Hess measured the rate of discharge of electroscopes from a balloon, and found that it increased rapidly with increasing altitude. Years later, Auger [5] and colleagues established the existence of extensive air showers initiated by cosmic rays. Using sets of two or three Geiger counters, they measured the coincidence rate between the counters as a function of the distance separating them. Expecting the coincidence to drop sharply and quickly disappear, they instead found the rate to drop quickly at first but then remain steady up to distances of 300 m, thus demonstrating that the most energetic components of the cosmic radiation can be studied at ground level.

1.1.1 Characteristics of Cosmic Rays

Cosmic rays have been observed with energies spanning 14 orders of magnitude, from a few 10^6 eV to over 10^{20} eV (see Figure 1.1). Above a GeV[1], cosmic rays follow a power law spectrum:

$$\frac{dN}{dE} \propto E^{\gamma}, \tag{1.1}$$

with differential index $\gamma \sim -2.7$Above 10^{15}eV the spectrum steepens, with the index dropping to ~ -3.0. This spectral feature is called the knee. The spectrum appears to flatten out again near 10^{20}eV. In keeping with the anatomical metaphor, this feature is called the ankle.

Cosmic rays are isotropic, but below energies of approximately 10^{10}eV [6, 7], charged particle emission from the sun adds to the flux of cosmic rays at the earth. This has the effect of obscuring the flux of extrasolar cosmic rays, since one 10 GeV proton looks exactly the same as any other 10 GeV proton, regardless of its source. Detectors of charged cosmic rays that are located well within the geomagnetic field, such as satellites in near-Earth orbit, balloon experiments and especially ground-based detectors, become ineffective below 4 GeV, since charged particles at these energies are turned away from the earth altogether by the geomagnetic field[2].

[1]In this dissertation, the following abbreviations will be used: MeV= 10^6eV, GeV= 10^9eV, TeV= 10^{12}eV, PeV= 10^{15}eV.

[2]The behavior of the geomagnetic cutoff varies with latitude, since the direction of the earth's magnetic field varies with latitude [8].

1.1.2 Acceleration and Propagation

Although they have been studied extensively since their discovery nearly nine decades ago, the origin of cosmic rays is still not well understood. Because the paths of cosmic rays are bent by magnetic fields, it is impossible to trace cosmic rays back to their sources. Thus, acceleration sites of cosmic rays have not been observed directly. Nevertheless, the specific characteristics of the cosmic ray flux themselves have suggested models of acceleration.

Like so many good ideas in high energy physics, the first model of cosmic ray acceleration was due to Enrico Fermi [9]. Fermi's was a stochastic acceleration model, in which charged particles are magnetically reflected at random by moving magnetic clouds. This results in small energy gains and losses for the charged particles, but the net effect is an average energy gain per collision, with the net energy gain per collision being proportional to square of the velocity of the cloud. The escaping charged particles follow a power law spectrum.

The current favorite picture of cosmic ray acceleration involves acceleration of charged particles by strong magneto-hydrodynamic shock fronts [10]. A shock is a discontinuity in the thermodynamic state of a body of material, propagating through that body. Figure 1.2 illustrates the propagation of a shock through a fluid. In the rest frame of the shock, the material on both sides of the shock front appears to be coming toward the shock. This can be understood qualitatively by noting that the shocked material appears to push the shock front forward into the unshocked

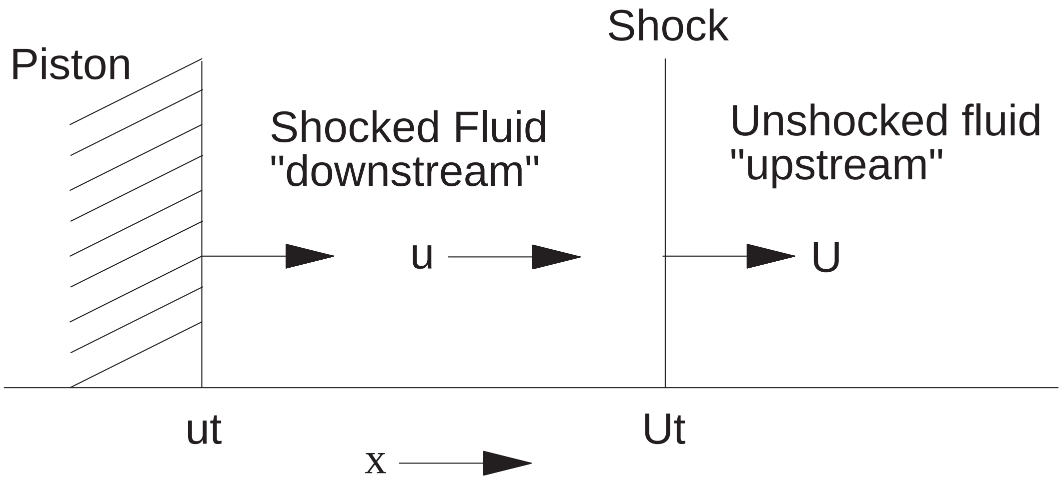

Figure 1.2: A schematic illustration of a shock produced by a piston in a fluid.

material. Thus particles crossing the shock front are met by oncoming material no matter which way they cross. All collisions are head-on, and thus energy-gaining collisions. This leads to an average energy gain per collision which is linear in β, and thus faster acceleration of cosmic ray particles. This model, sometimes called first-order Fermi acceleration, predicts a spectral index $\gamma \sim -2$.

While most cosmic rays are contained by galactic magnetic fields, some of the cosmic rays are able to escape confinement. The leaky box model [6] predicts that the probability of escape increases with increasing magnetic rigidity, $R = p/Z$. This is because particles of higher rigidity traverse circular paths of larger radius through magnetic fields than particles with lower rigidity, and these larger circular paths are more likely to lead out of the galaxy than are the smaller circular paths. This rigidity dependence alters the energy spectrum of cosmic rays, bringing the predicted spectral index of cosmic rays to $\gamma \sim -2.6$ for first order Fermi acceleration plus leaky box confinement. The same mechanism likely prevents the intrusion of low rigidity extra-galactic cosmic rays into the galaxy. The knee in the cosmic ray energy spectrum, which is thought to be related to the maximum energy attainable through shock acceleration in SNR's, could be evidence of a change in $\langle Z \rangle$, or a crossover between populations of galactic and extra-galactic cosmic rays.

1.2 Air Shower Physics

High energy cosmic rays incident upon the earth's atmosphere interact with the air molecules, causing cascade showers. If the primary particle is of sufficient energy, some of the interaction products in the cascade can reach ground level. The swarm of relativistic particles from such an event that reaches ground level is called an extensive air shower (EAS). As a shower develops in the atmosphere, the number of particles created by the cascade grows exponentially while the average particle energy falls. Eventually, the average energy of the shower particles drops to the point where more energy is lost to processes which merely reduce the energy of shower particles than to processes which create additional shower particles. After this energy, called the critical energy, has been reached the number of particles in the shower begins to fall off exponentially. The particles in an EAS are distributed in a thin pancake-like layer, several meters thick and hundreds of meters wide at ground level. This moving pancake of high energy particles is called the shower front. The shower front is centered around the so-called shower core, which follows the same path that the primary cosmic ray would follow if it did not interact with the atmosphere.

A cosmic ray EAS typically develops first via strong nuclear interactions, producing nuclear fragments and mesons. These strong interaction products form the so-called hadronic component of the EAS, which fuels the other two EAS components: the electromagnetic and the muonic components. Most of the secondary and tertiary particles produced are pions. The vast majority of neutral pions decay almost immediately into photon pairs. A charged pion most often interacts with the air nuclei to create additional pions, but can also decay into a muon and a neutrino. A smaller fraction of secondaries in the hadronic component are kaons, and these decay quickly into pions and muons. Both muons and neutrinos are unimportant to EAS development, except as a channel for energy loss, but the muons are very important for EAS measurement, as will be explained below. The gamma rays created by neutral pion decay initiate electromagnetic cascades.

An electromagnetic cascade is a process of alternating steps of Bremsstrahlung and pair production, starting with a high energy electron or photon and leading to a rapid increase in the number of particles. The theory of electromagnetic cascades is treated in detail in [11], and the most recent results and data are discussed in [3].

1.2.1 Particle-Creating Processes

Bremsstrahlung [11, 8], which is German for "braking radiation", is the process by which a high energy charged particle emits a photon when it is accelerated by an electric field. The Bremsstrahlung cross section has a $1/m^2$ dependence, so that Bremsstrahlung is more important for electrons than other charged particles in air showers. Thus can an electron emit a photon through its interaction with the Coulomb field of a nucleus of one of the atoms in an air molecule. The electron loses energy equal to the energy of the emitted photon in the process. In passing through an amount of matter X, measured in g/cm^2, the energy loss of an electron through Bremsstrahlung varies in direct proportion to the energy of the electron, whereas the energy loss through ionization is proportional to the logarithm of the electron energy. Thus at high energies the dominant energy loss mechanism is Bremsstrahlung, and the number of particles in a cascade can grow. The energy at which the energy loss through ionization equals the energy loss through Bremsstrahlung is called the critical energy, E_C. For electrons in air, the critical energy is $\sim$ 90 MeV[3]. Below this energy, the dominant energy loss mechanism for electrons is ionization, so when the average electron energy in an EAS falls below E_c, the number of particles begins to decline.

Pair production is the process by which a high energy photon is converted into an electron-positron pair through its interaction with an electric field . Thus can a high energy photon in an air shower cause the creation of an electron-positron pair by interacting with the Coulomb field of an air molecule's nucleus. Pair production is the

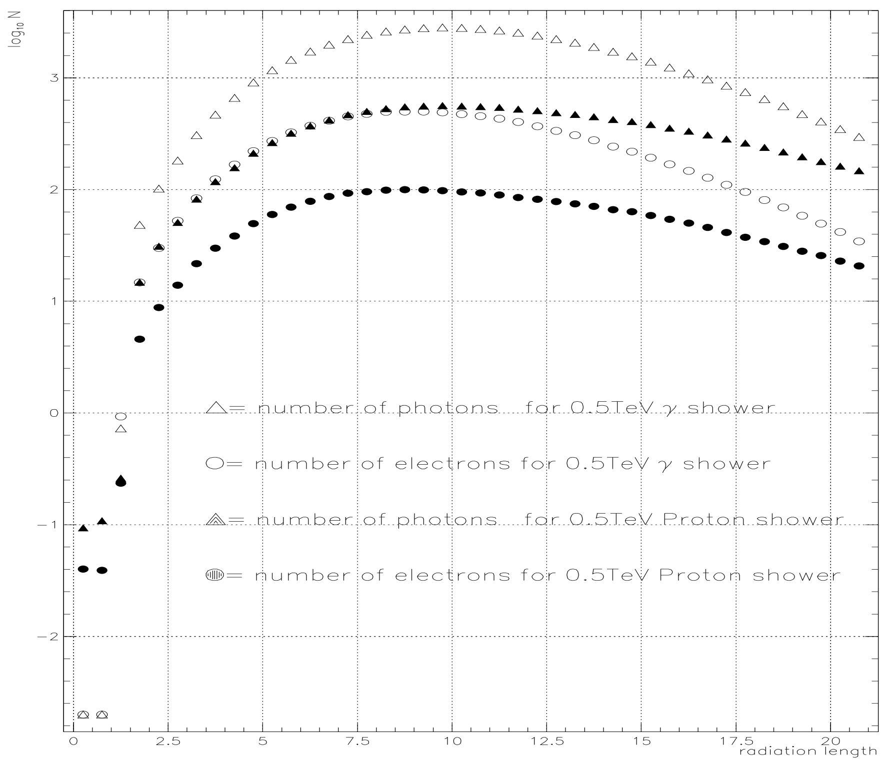

Figure 1.3: Longitudinal development of typical air showers, taken from simulated events [12]. Milagrito sits beneath an overburden of 20.75 radiation lengths.

dominant electron loss mechanism for photons passing through air at high energies, with Compton scattering becoming the dominant process below photon energies of ~ 20 MeV [13].

A useful quantity for measuring energy loss mechanisms at high energies is the radiation length, X_0 This is the average amount of matter through which a high energy electron loses all but $1/e$ of its energy through Bremsstrahlung. For air, $X_0 \approx 36$ g/cm^2. At sea level, the total depth of the atmosphere is about 37 radiation lengths. For photons, the amount of matter through which they must pass to lose $1/e$ of their energy is about $\frac{9}{7}X_0$ [3]. The energy lost by a high energy electron through

Bremsstrahlung after passing through an amount of matter X is given by:

$$E = E_0 e^{-(X/X_0)}. \tag{1.2}$$

The fact that the pair production interaction length is slightly larger than the Bremsstrahlung radiation length means that over the same distance through matter, the average number of pair production interactions is smaller than the average number of Bremsstrahlung interactions. This, combined with the fact that the ionization energy losses to electrons are slightly greater than the energy losses due to Compton scattering of secondary photons means that an electromagnetic cascade is likely to have more secondary photons than electrons after several radiation lengths. This is shown in Figure 1.3, which shows the average number of secondary electrons and photons in 500 GeV air showers as a function of the number of radiation lengths traversed. The plot is the result of computer simulated air showers.

Figure 1.3 also illustrates the fact that proton initiated showers tend to have smaller size than γ-ray initiated showers. In other words, a γ-ray shower has, on average, more secondary particles in it than a shower created by a proton of the same energy at the same atmospheric depth. This is because much of the energy of a proton showers goes into production of hadrons, muons, and neutrinos.

1.2.2 Cherenkov Radiation

If a dielectric medium has index of refraction, n, greater than one, then the phase velocity, v_ϕ, of light traveling through that medium is reduced to $v_\phi = c/n$. It is

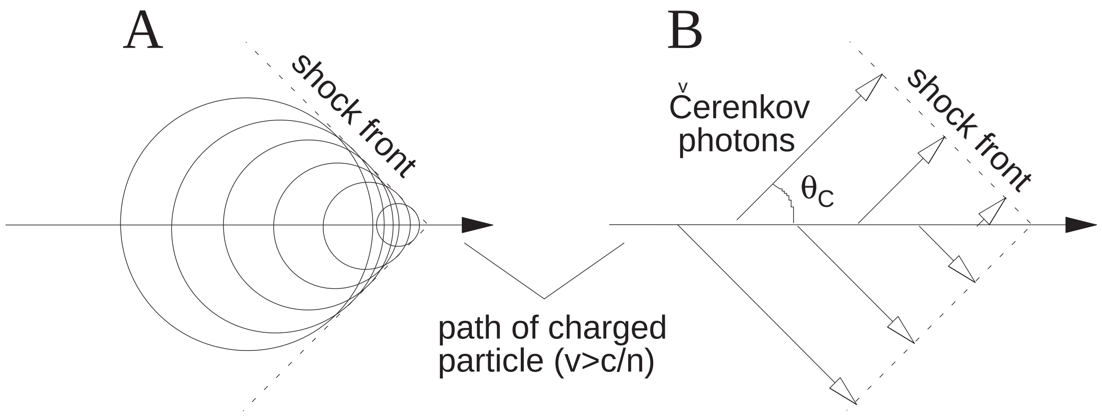

Figure 1.4: Schematic diagram of Cherenkov radiation emission.

possible for a charged particle to pass through this medium with speed greater than c/n, however. If this happens, the charged particle causes the medium to radiate light, called Cherenkov radiation after its experimental discoverer [14].

As the charged particle passes through the dielectric medium, its Coulomb field produces a coherent effect in the dielectric medium, not unlike a shock wave in the particle's wake. The shock wave front propagates away from the path of the particle at an angle that depends on the index of refraction of the medium. Figure 1.4 illustrates this process. This Cherenkov angle, θ_C is given by,

$$\cos\theta_C = \frac{v_\phi}{v_{particle}} = \frac{1}{n}\beta \tag{1.3}$$

Equivalently, Cherenkov photons are emitted in a cone, with half angle θ_C, centered about the path of the charged particle. In Figure 1.4, this is shown schematically in part B, while part A shows a Huygens construction of how a coherent shock front forms and propagates. The Cherenkov angle in water is $\sim$41°. The number of photons produced per unit path length per unit wavelength interval of the emitted photons for a singly charged particle is given by,

$$\frac{d^2N_\gamma}{dxd\lambda} = \frac{2\pi\alpha}{\lambda^2}\left(1 - \frac{1}{\beta^2 n^2(\lambda)}\right), \tag{1.4}$$

or equivalently

$$\frac{d^2N_\gamma}{dxdE_\gamma} = 370\sin^2\theta_C(E_\gamma)eV^{-1}cm^{-1}, \tag{1.5}$$

where α in Equation 1.4 is the fine structure constant, $e^2/\hbar c$ [3]. Since the index of refraction is a function of wavelength, the above expressions do not diverge at small wavelengths. This happens because real dielectric media are dispersive, with wavelength bands of resonant absorption. In these bands, what would be Cherenkov emission is immediately absorbed back into the medium [15]. Thus Cherenkov emission appears mostly as blue and ultraviolet light. Though not an important energy loss channel for high energy electrons, Cherenkov radiation is very useful for the detection of charged particles.

1.2.3 Air Shower Development

Rigorous calculations of the development of electromagnetic cascades have led to several analytical models for the longitudinal and lateral development of the electromagnetic component of air showers. The most often used model for the longitudinal development is the so-called "Approximation B" of Rossi [11, 10], which neglects energy losses due to Compton scattering but assumes constant ionization losses for electrons. It calculates the mean number of secondary electrons and positrons in a cascade with primary energy E_0 as a function of atmospheric depth X, measured in g/cm^2. It is given by,

$$N_e = \frac{0.31}{\sqrt{y}} e^{X(1-1.5\ln s)} \tag{1.6}$$

where

$$s = \frac{3}{1+\frac{2y}{X}} \tag{1.7}$$

$$y = \ln\left(\frac{E_0}{E_c}\right). \tag{1.8}$$

The parameter s is called the shower age, and the number of secondary electrons, N_e, is called the shower size. These equations indicate a complex relation between shower size, primary energy, and atmospheric depth. But the relation between the size of the shower when the average particle energy drops below E_C, called shower max, and the primary energy is simple: $N_{e_{max}} \propto E_0$. Figure 1.5 illustrates this. The solid curves show the results of Approximation B as a function of atmospheric depth for several different primary energies, E_0. The symbols represent the averages over 500 simulated vertical γ-initiated air showers at the indicated energies. It can be seen that the simulation results agree well with Approximation B.

It is important to note that these equations give the average number of secondary particles as a function of depth, but that each shower is likely to deviate from this. The deviation from shower to shower is highly dependent on the atmospheric depth of the primary particle when it undergoes its first interaction.

The lateral spread of an air shower is due mainly to multiple Coulomb scattering.

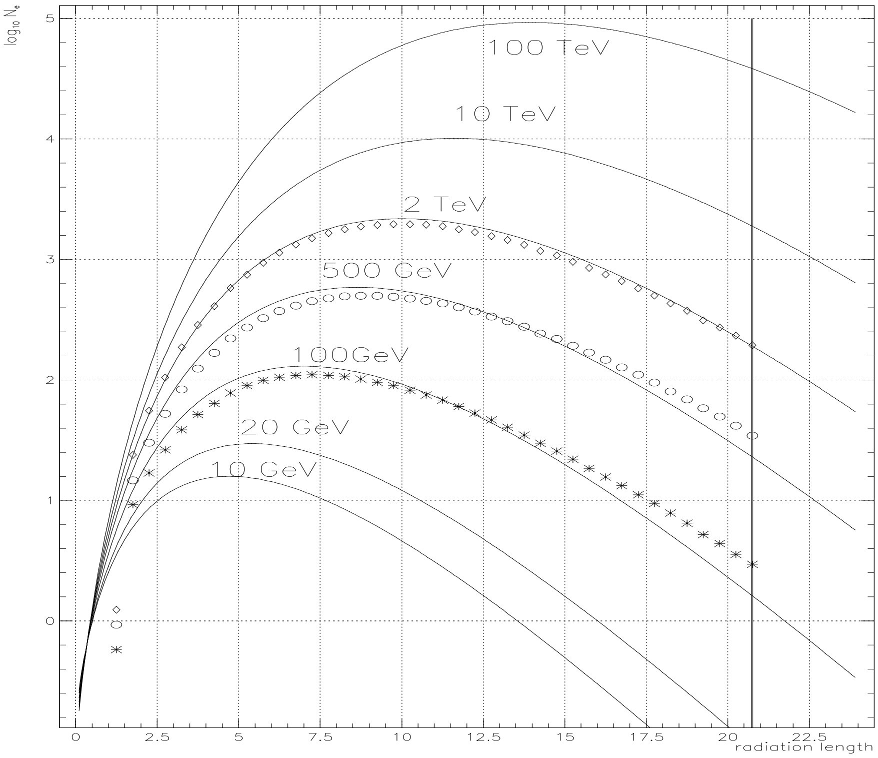

Figure 1.5: Longitudinal development of typical γ-ray air showers [12]. The vertical line shows Milagrito's atmospheric depth, which is 20.75 radiation lengths. The curves and symbols are explained in the text.

The particles in a VHE air shower have energies so high that most radiative processes are extremely forward-peaked, and so most of the lateral spread is due to multiple scattering of the secondary electrons in the Coulomb fields of the air nuclei. The problem of lateral development of an electromagnetic cascade has been studied extensively, and is well approximated by the so-called Nishimura, Kamata, and Greisen (NKG) function [16]. This function gives the average electron density as a function of lateral distance from the shower core. The function is,

$$\rho(r) = \frac{N_e}{r_0^2} f(s, \frac{r}{r_0}), \tag{1.9}$$

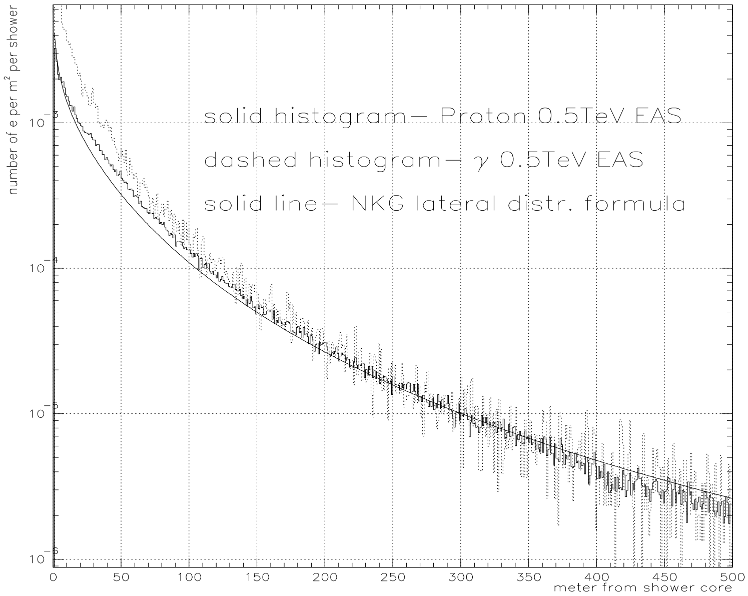

Figure 1.6: Lateral development an air shower [12]. The solid curve is the NKG function discussed in the text. The histograms show results from computer simulated air showers.

with $f(s, \frac{r}{r_0})$ given by,

$$f(s, \frac{r}{r_0}) = (\frac{r}{r_0})^{s-2}(1 + \frac{r}{r_0})^{s-4.5}\frac{\Gamma(4.5 - s)}{2\pi\Gamma(s)\Gamma(4.5 - s)}, \tag{1.10}$$

The parameter r_0 is called the Moliere unit, and for air it is $\sim 99\ m$. There is also a longitudinal spread of secondary particles in a cascade. The multiple Coulomb scattering not only causes many secondaries to end up far from the axis, but it leads to many secondaries being set back from the leading edge of the shower front. Although the NKG function was derived to describe purely electromagnetic cascades, it is found to accurately describe the lateral spread of hadronic air showers [16]. The NKG function is plotted in Figure 1.6 [12], along with the results of simulated air showers.

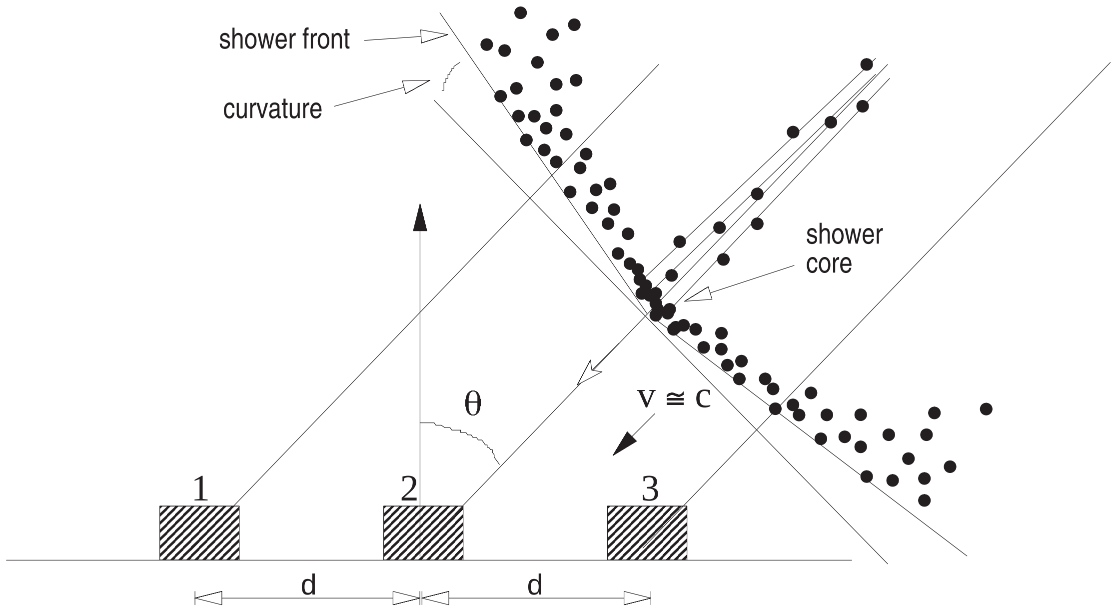

Figure 1.7: A schematic diagram of an extensive air shower array.

1.2.4 Extensive Air Shower Array

An extensive air shower array is an array of particle detectors used to detect the prompt particles in the shower front at ground level. The relative arrival times of the hits in the array and the distribution of energy over the array are used to reconstruct the direction and energy of the incident particle. This section will discuss the basic features of air shower arrays in a qualitative way, with quantitative matters left for Chapter 2.

Figure 1.7 shows a schematic diagram of an EAS array. This two-dimensional toy-model array is made of three stations of particle detectors. As the shower passes over and through the array, the shower front hits station 3 first because of the incident angle, θ, of the shower. The time of the hit is recorded. Next hit is station 2, and finally the front passes through station 1, with the times of those hits recorded also. Because the stations are separated by a distance d, and that the shower front moves very close to the speed of light, the angle θ can then be calculated. The detected air shower is usually called an "event" by experimenters.

This calculation is complicated by the fact that the shower front is not flat, i.e., the particles do not actually travel in a tight plane. The shower front is configured more like a cone centered about the shower axis with the point of the cone oriented in the direction of the shower, as illustrated in Figure 1.7. This is called the *curvature* of the shower. What it means to an extensive air shower array is that the shower front arrives slightly later than a plane-front would, as a function of distance from the shower core. Additionally, the longitudinal density of particles in the shower front is a function of lateral distance from the shower axis, as discussed Section 1.2.3. Because of this, the shower front particles near the core tend to be grouped together more tightly in time than the shower front particles farther from the core. This leads to the so-called *sampling* effect. Together, sampling and curvature cause a delay in the arrival times of shower front particles as a function of lateral distance from the shower axis.

These effects can be corrected, but first the shower core must be located. In order to locate the position of the core, an extensive air shower array must also record the density of secondary particles along with the arrival times when the stations are hit by an air shower. Then the particle density distribution can be fit to a smooth function, such as the NKG function, Equation 1.9, whose peak should coincide with the position of the shower core. Once the shower core is located, the curvature and sampling corrections can be applied to the arrival times of the hits in the stations, starting at the shower core and moving out to the edges of the array. The magnitude of the corrections are usually found by studying computer simulated air showers. Such corrections are not perfect, however, and there is still some error in calculating the arrival directions of incident cosmic rays. The average error in reconstructing the directions of cosmic ray induced air showers is called the angular resolution.

Based on the number of secondary particles and their distribution across the array, one can use Equations 1.6 and 1.9 to estimate the shower size, and from this and Equation 1.8 the energy of the primary cosmic ray. This method, or some variant of it, has been used by most previous air shower arrays to measure the energies of the detected air showers.

1.2.5 Past Experiments

Three notable detectors of extensive air showers are the CYGNUS array, the Tibet air shower array, and the Whipple Telescope. These three are mentioned because of their contributions to the main topic of this dissertation: studying the shadow of the moon in cosmic rays. It should be mentioned that all three of these experiments were designed to search for point sources of cosmic γ-rays. But because of the low flux of γ-rays compared to the background of hadronic cosmic rays, they must each sift through a vast background of cosmic ray events in order to find γ-ray showers.

The CYGNUS experiment [17] was an extensive air shower array comprised of 108 scintillation counters in Los Alamos, NM. CYGNUS ran for 10 years starting in 1986, with an energy threshold of ~50TeV and angular resolution $\sim 0.8°$. The Tibet array [18] is an array of 221 scintillation counters, located in Yangbajing, Tibet. The experiment has an energy threshold of a few TeV, and angular resolution $< 1.0°$. Both of these arrays are comprised of ~1m^2 scintillator sheets optically connected to photomultiplier tubes (PMTs), with the scintillator stations spread out over large areas. Thus the full area of the detector is quite large, while the active detector area is quite small, being the number of stations times the area of each station. In other words, these arrays sample the air shower particles in small regions spread out across a large area. Additionally, since scintillation light is the result of ionization from charged particles, scintillator detectors are sensitive mainly to the electrons and positrons in air showers, and not the photons.

The Whipple telescope is not an extensive air shower array at all, but instead employs the air Cherenkov technique; this instrument uses the Cherenkov radiation caused by the passage of an air shower through the atmosphere [19] to detect cosmic rays. It is comprised of a segmented structure of 248 small mirrors that collect the UV and optical Cherenkov emission. The distribution of the Cherenkov radiation is used to form an image, and image analysis algorithms have been developed by the

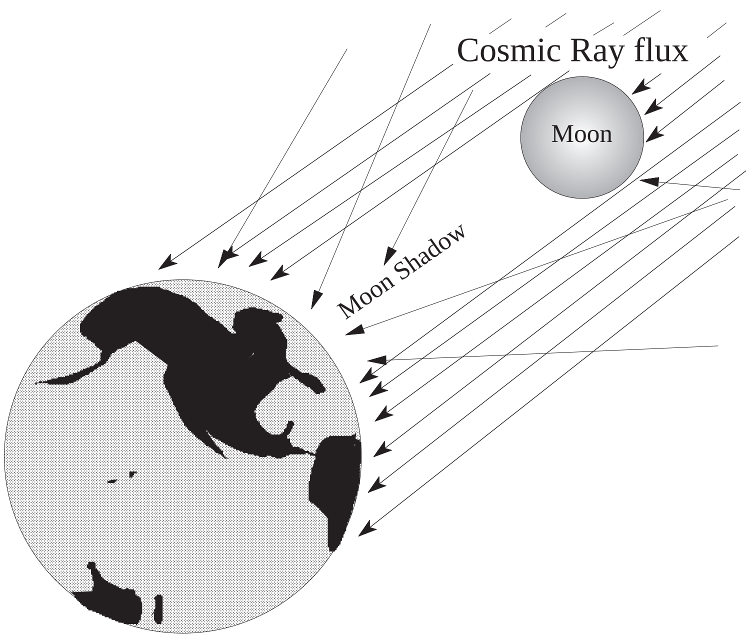

Figure 1.8: A schematic diagram of how the moon shadow is created.

Whipple collaboration which allow them to reject the hadronic background events with high certainty. The instrument also has very good angular resolution, $< 0.15°$, and a lower energy threshold than the extensive air shower arrays mentioned above, with their peak sensitivity to γ-ray showers near $\sim$few 100 GeV.

1.3 Moon Shadow Concept and History

As it passes overhead, the moon blocks the cosmic rays that would otherwise hit the earth. By observing the events from the vicinity of the moon, a deficit of events due to the moon's presence can be seen; this is the moon shadow [20]. The same shadowing effect can be seen with the sun.

CYGNUS reported the first observation of the moon and sun shadows [21] in 1991 as a deficit of events 4.9 σ below the cosmic ray background. The effect was soon confirmed by several other experiments. In 1993, the Tibet array reported a detection of both the moon and sun shadows [22], with a shift in the position of the center of the deficit of the sun shadow, attributed to the magnetic field of the sun.

With a perfect detector, the moon shadow should appear as a circular deficit of events centered at the moon's position and with radius $0.26°$, since that is the angular width of the moon as seen from the surface of the earth. The deviation from the ideal case has been used to estimate the angular resolution of EAS detectors [21], as well as to verify correct pointing [22]. At TeV energies, the geomagnetic deflection of cosmic rays is noticeable, meaning that the magnitude of the deflection is on the same order as the angular resolution of detectors. Thus, the geomagnetic deflection of cosmic rays can be observed in the shadow of the moon as a displacement of the center of the deficit of events relative to the true position of the moon.

It should be possible to use the moon shadow to develop an absolute energy calibration at TeV energies, since the deflection of a cosmic ray in the geomagnetic field can be used as a measure of the rigidity. The geomagnetic field acts as a spectrometer, and cosmic rays with lower rigidity will be deflected more as they pass through the magnetic field than cosmic rays at higher rigidity. Thus by separating the moon shadow into smaller sub-shadows comprised of events of different size, one might expect to see the centroid of the deficit of the shadows displaced more for the small sized, lower energy, events, and less for the large sized, higher energy, events.

1.4 Cosmic Antimatter

It is expected that some small flux of antimatter be present in the cosmic radiation, created by the interaction of high energy protons and nuclei with the interstellar medium. Secondary $\overline{p}$'s are expected to be seen at a level of $\sim 10^{-4}$ times the proton flux, with a characteristic peak around 2 GeV [23], due to the kinematics of $\overline{p}$ production. Above that the spectrum of secondary $\overline{p}$'s in the cosmic ray flux should follow a power law, just as the spectrum of cosmic rays does.

Antiprotons have been measured in cosmic rays up to energies around 10 GeV. The measured $\overline{p}$ flux is consistent with secondary production [24] described above. Figure 1.9 shows the measured $\overline{p}$/p ratio as a function of energy. The measurements were compiled by the BESS experiment, which is described below. The curves in Figure 1.9 show recent theoretical curves for the $\overline{p}$/p flux due to secondary production of $\overline{p}$'s at solar minimum [23]. The measured low energy fluxes can be extrapolated to higher energies with a power law spectrum, and this can serve as the model for $\overline{p}$ flux expectations at TeV energies.

If the $\overline{p}$ flux in cosmic rays is due to cosmic rays escaped from anti-galaxies and entering our own galaxy, their flux can be expected to follow a power law spectrum with a spectrum harder than the cosmic ray flux [25, 26]. This would lead to an increase in the $\overline{p}$/p ratio with increasing energy, with this rise flattening near 100 TeV.

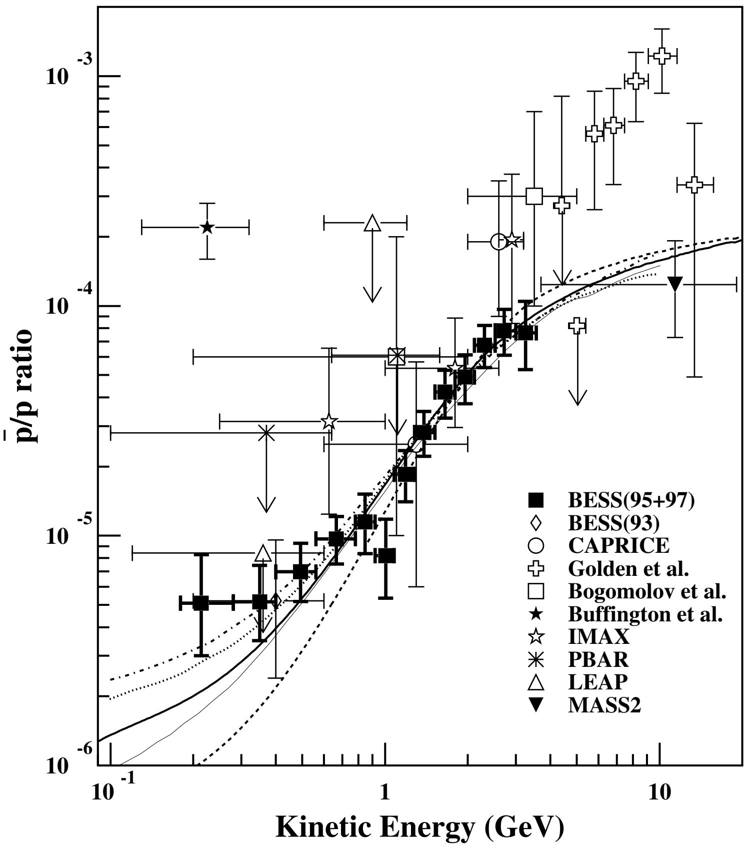

Figure 1.9: The measured $\overline{p}$/p ratio [23] in the GeV regime. The curves show expectations based on several theoretical models.

This increase could make the $\overline{p}$/p as high as 1% at TeV energies.

1.4.1 Low Energy Measurements

At energies below 10 GeV, the fluxes of cosmic rays are high enough that satellite and balloon borne experiments, which are necessarily small, can gather enough events to make precise measurements of fluxes.

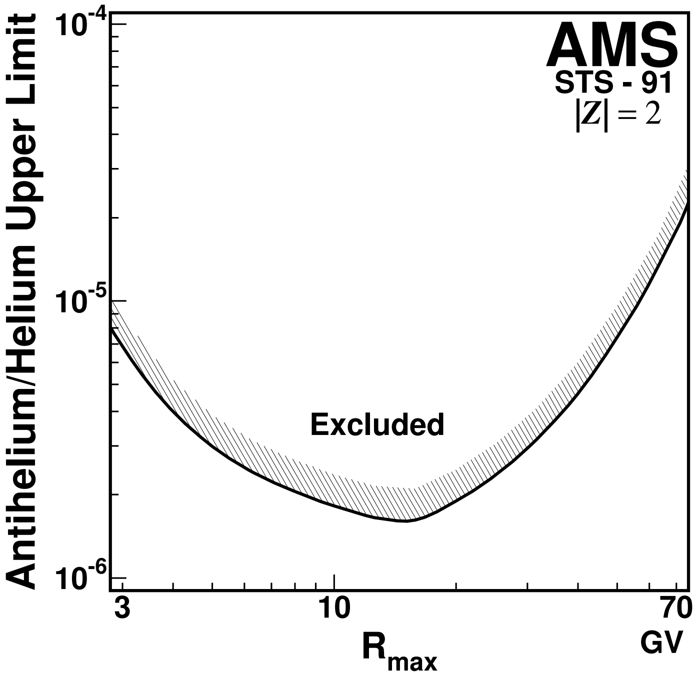

Figure 1.10: The $\overline{He}/He$ ratio [28].

BESS

The Balloon Borne Experiment with Superconducting Solenoidal Spectrometer (BESS) is a high resolution spectrometer designed to search for rare cosmic rays. The experiment is equipped with a 1 T magnet which provides mass and charge identification capabilities. They recently reported on their 1997 flight, in which they saw 415 unambiguous $\overline{p}$'s up to 3 GeV in energy. Figure 1.9 shows the results of this flight compiled with older $\overline{p}$/p ratio measurements [23, 27].

AMS

The Alpha Magnetic Spectrometer (AMS) experiment is a high-precision spectrometer with a powerful magnet, making it capable of measuring the absolute magnitude and sign of the charge of detected particles [29]. It will be installed on the International Space Station and should begin taking data in earnest in 2003.

On a test flight aboard the Space Shuttle, AMS set a new upper limit of the $\overline{He}/He$ ratio as a function of rigidity, up to 70 GV/c. The results are shown in Figure 1.10. The presence of anti-helium in cosmic rays could suggest a global antimatter/matter symmetry in the universe [30]. AMS will also be able to measure the $\overline{p}$ energy spectrum up to 100 GeV. The AMS Collaboration expects to push the upper limits on the $\overline{He}/He$ ratio down several orders of magnitude during its operation aboard the Space Station [28].

1.4.2 High Energy Measurements

There have been no detections of antimatter in cosmic rays above 10 GeV. But detection is possible, using the moon's shadow in cosmic rays. As negatively charged particles, $\overline{p}$'s are deflected in the direction opposite to the direction that p's are deflected by magnetic fields. So, in energy regimes where there is significant deflection due to the magnetic fields, another shadow shifted in the opposite direction from the sun or moon shadow would be evidence for antimatter in the cosmic ray flux. In 1994, Chantell *et al.* used the Tibet array's moon shadow result to establish an upper limit of 30% on the $\overline{p}/p$ ratio [31]. The Tibet Collaboration then claimed a 22% upper limit [32] on the $\overline{p}/p$ ratio through analysis of the sun shadow in ~ 10 TeV cosmic rays [32] in 1995.

The ARTEMIS experiment used a special optical filter to suppress moonlight, in an attempt to use the Whipple Telescope to study shadowing of the moon and search for an antimatter component of the cosmic ray flux at TeV energies. They have discovered that the sensitivity of the instrument to look at the shadow is too low to perform the $\overline{p}$ search [33].

Chapter 2

The Milagrito Detector

Like the other EAS arrays mentioned in Chapter 1, the Milagrito Water Cherenkov Detector was built to search for point sources of cosmic γ-rays. But, also like the other EAS arrays described, Milgarito must search for these γ-rays amidst the vast background of cosmic rays. It is this background of otherwise unwanted cosmic rays, however, that serves as the signal for this analysis.

Milagrito was comprised of an array of PMTs that all faced upward inside a covered pond of water. It was designed to detect the Cherenkov emission of air shower secondaries entering the water in the pond. Unlike the other EAS arrays described in Chapter 1, Milagrito was sensitive to all the secondary particles in an air shower, since the photons in EASs contributed to the shower detection after undergoing pair production in the water. The resulting electron/positron pairs caused Cherenkov emission in the pond water. This is illustrated in Figure 2.1. The sensitivity to all

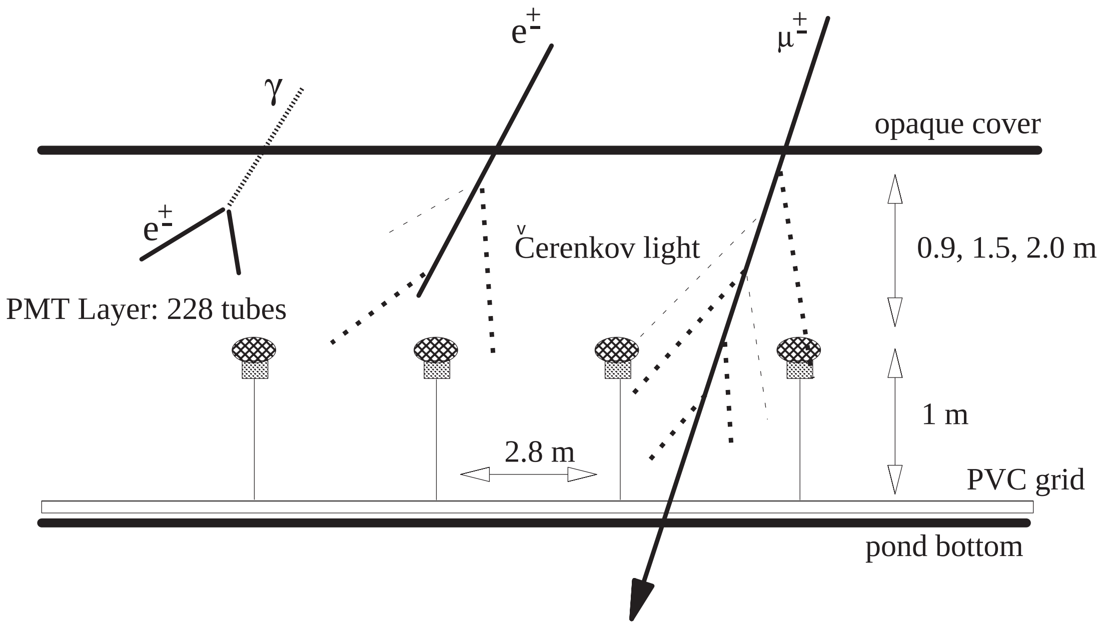

Figure 2.1: A schematic view of the Milagro detector.

shower particles distinguished Milagrito from the other EAS arrays mentioned by giving it a large detector area, because the entire pond area was an active detector of air shower particles. This allowed Milagrito to make a much denser sampling of EAS particles than did previous detectors, which resulted in a lower energy threshold for Milagrito than for any previous EAS array.

Milagrito served as the prototype stage for the Milagro detector. Much of what was learned though the operation of Milagrito and through the analysis of the Milagrito data served as a foundation for improvements in the final design and operation of Milagro. But Milagrito was also a valuable detector in its own right, as the reader shall see.

2.1 Detector Description

2.1.1 Sketch of Milagrito

The Milagrito detector site is located at the Fenton Hill Observatory, 35 miles northwest of Los Alamos, NM, at 35.9° North and 106.7° West. At an altitude of 2646m, the atmospheric overburden at the Milagro site is approximately 750g/cm^2, roughly 70% of that at sea level. Figure 2.2 shows an aerial photograph of the pond.

The detector consisted of an array of 228 photomultiplier tubes (PMTs) submerged in a covered, artificial 21 million liter pond of water. The pond is 60m x 80m at the top and has sloping sides which lead to a 30m x 50m bottom, with a mean depth of 8m. The pond is lined with black polypropylene, and is covered by a light-tight layer of the same material. A water purification system circulated the water from the pond in order to reduce the attenuation and scattering of the Cherenkov light.

Milagrito's PMTs were deployed in a single horizontal layer. Milagrito began as one layer of PMTs suspended at a depth of 0.9m below the water's surface. The depth of water above the PMTs is an important parameter for the optimal operation of the detector. The water must be deep enough to allow the shower particles to emit enough Cherenkov radiation to be detected, but not be so deep that the Cherenkov emission is absorbed by the water before it can be detected by the PMT array. The water must also be deep enough to allow most of the shower γ-rays to pair-produce in the water so that they can cause Cherenkov emission and be detected by the PMT

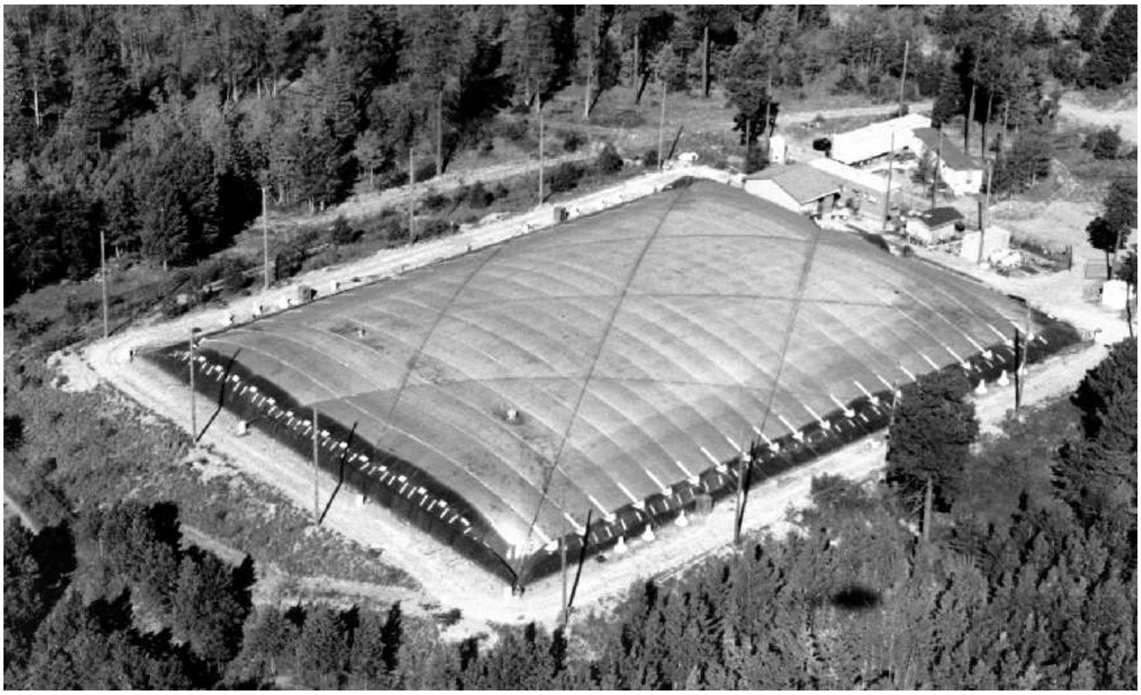

Figure 2.2: Aerial photograph of the Milagro pond.

array. These considerations were tested with simulations and in the operation of Milagrito, by changing the depth of the water above the PMTs. After several months of operation, more water was added to the pond so that the PMTs were at depths of 1.5m, and then 2m. Through analysis of the Milagrito data, it was decided that Milagro's main PMT layer would sit 1.5m below the surface of the water.

The tubes floated face-up in the pond, and were arranged in a square grid pattern, 2.8m to a side. Each PMT was suspended by a Kevlar string anchored to a sand/water-filled polyvinyl chloride (PVC) grid structure. This grid rested on the bottom of the pond and provided ballast to anchor the PMT array. Each PMT was encapsulated in a water tight PVC cylinder that covered the bottom portion of the glass and the electronics base, but left the photocathode unobstructed. A single coaxial cable, which carried HV from the power supplies to the PMT and signal from the PMT to the data acquisition system, was connected to each PMT through a waterproof HV connector built into the encapsulation.

Water System

The water purification system was of a design similar to that used by the IMB detector[34]. Water was drawn in from the pond and could be sent first to a water softener. The flow was next directed through several filters: a sand/gravel media filter, a charcoal filter, and then a micron filter. Next the water was exposed to ultraviolet light, to prevent the growth of algæ and any other organisms in the water. Before being recirculated back into the pond the water was sent through a final sub-micron particle filter.

The water quality was somewhat erratic throughout the lifetime of Milagrito, as demonstrated by periodic tests of the absorption length of samples taken from both the water recirculation system and the pond itself. This is shown in Figure 2.3. The filter system was rebuilt over the summer of 1998, and the new system improved the water quality as shown in Figure 2.3.

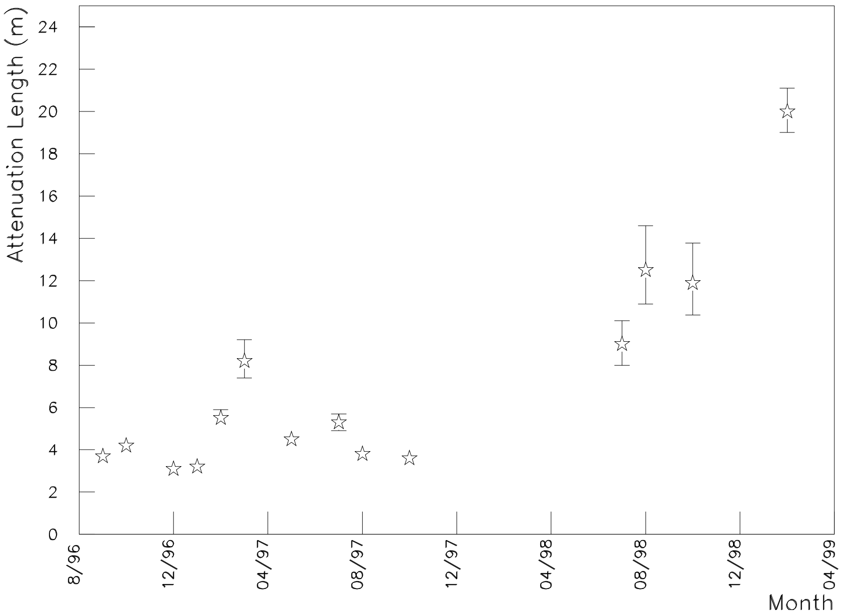

Figure 2.3: Measured attenuation length of pond water. The points before 1998 are for Milagrito, and the points after are for Milagro. Note the improvement in water quality with the new filtration system.

Cover and Liner

The pond is lined and covered with a woven polyester mesh sandwiched between two layers of black polypropylene. The material is waterproof and opaque, but buoyant. The cover of the pond is the same size as the liner, so that when the pond is empty the cover rests along the sides and bottom of the pond directly over the liner. The cover is sealed around the edges of the pond and equipped with many straps which can be used to suspend it into a catenary state. There is a door built into the cover on the north end of the pond. The pond is equipped with fans which can be used to raise the cover when work needed to be done under the cover. The top of the cover was painted silver, so that it would reflect the majority of sunlight incident upon it, to help control the temperature inside the pond when the cover was raised.

Photomultiplier Tubes

The Hamamatsu 20.3 cm R5912 photomultiplier tube (PMT) was chosen for Milagrito because of its excellent performance characteristics. It has good time and charge resolution, as shown in laboratory tests by a single photoelectron (PE) timing resolution of 2.7 ns at full width at half maximum (FWHM) and good linearity in its charge output up to 75 PEs. The quantum efficiency of the PMT is in the range 20-25% at 325-450 nm, with peak sensitivity to photons at 420 nm. At an average operating voltage of 1720 V, the anode signal rise-time of the PMT was measured to be 4 ns, and the electron transit time was measured to be 55 ns. This PMT also showed low incidence of single-PE prepulsing, 0.2-0.3%. The PMTs did show some late pulsing, which was found to occur 8-60 ns after the main pulse at 5.5% rate, and afterpulsing, which was found to occur 100 ns to 16 μs after the main pulse at a 5% rate. A solution to these problems was implemented in the electronics, as described below in Section 2.1.1.

The glass vacuum tube of the Hamamatsu R5912 is rounded, with the photocathode applied to the interior of the bulb. This is done to give a more uniform electron transit time from all parts of the photocathode. But it also has the side-effect of making the PMT sensitive to photons approaching the PMT from the side. This would

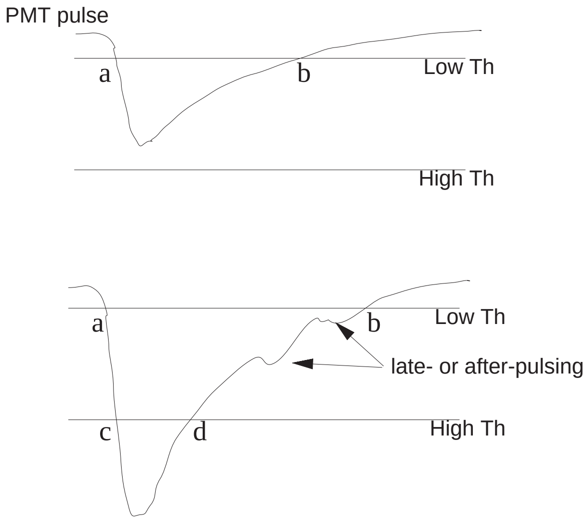

Figure 2.4: Time-over-threshold (TOT) diagram.

have unforeseen consequences for Milagrito, which will be described in Section 3.2.2.

Several PMTs failed during the lifetime of Milagrito. These were due mainly to resistor failure in the bases, but some failures were due to water leaking through the connectors.

Electronics

A brief description of the Milagrito electronics is presented here. They are described in greater detail elsewhere [35, 12, 36].

The reconstruction of an extensive air shower depends on accurate time and charge measurement of the pulses the PMTs. To accomplish these goals with as little cost as possible, the Milagrito detector used a two threshold *time-over-threshold* (TOT) system to measure and record the pulse heights and arrival times of the PMT signals.

A conceptual illustration of the TOT method is shown in Figure 2.4.

The output pulse of a PMT was sent through a capacitor pickoff into two parallel paths through the electronics. In one path, the signal was amplified by a factor of 15 and the other path had no amplification. The amplified signal was sent to a low threshold discriminator set at a voltage equivalent to 1 / 4 PE, and the unamplified signal was sent to a high threshold discriminator set to the voltage equivalent of 7 PEs.

If the output pulse from a PMT hit was small, then the pulse did not cross the high threshold. This is illustrated in Figure 2.4. A PMT pulse rises quickly and decays exponentially, and it crosses the threshold again on the way down. The points where the pulse crosses the discriminator threshold are labeled “a” and “b” in Figure 2.4. The times of these threshold crossings are recorded as t_a and t_b. The time difference between the discriminator crossings is called the *time-over-threshold*, and is proportional to the logarithm of the pulse height of the PMT hit,

$$\Delta t = t_b - t_a \propto \ln(N_{PE}). \tag{2.1}$$

The times when the threshold is crossed by the PMT pulse are sent to a time-to-digital converter (TDC), which digitizes the TOT with 0.5 ns resolution.

In the case of a large pulse height, the voltage rises past the low threshold, “a”, and proceeds past the high threshold, “c” in Figure 2.4. Then during the decay period, the voltage level crosses the high threshold, “d”, again and then the low threshold, “b”, on the way back down. Now, $(t_d - t_c)$ can be used as a measure of $\ln(N_{PE})$, as

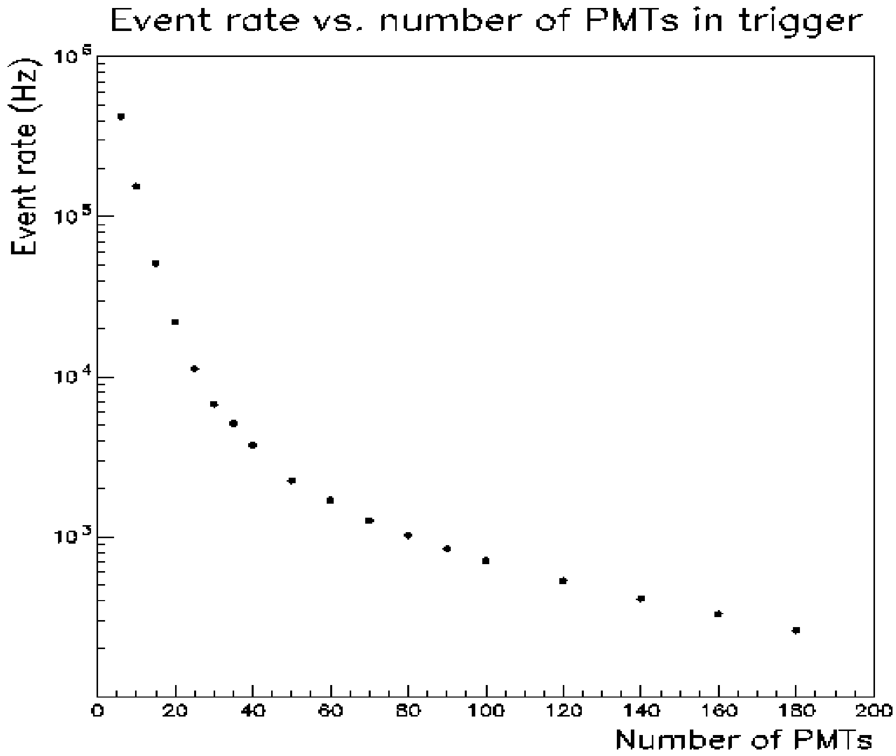

Figure 2.5: The Milagrito trigger rate versus the number of PMTs required to be in coincidence..

well as $(t_b - t_a)$.

The low TOT level is used for pulse heights of just a few PEs, and the high TOT is used for pulse heights above that. This expands the dynamic range of pulse heights that can be accurately measured, and it solves the problem of prepulsing associated with high pulse height hits by allowing the pulse height to be measured at a high voltage level above the level of smaller random hits. This also solves the problems of late-pulsing and afterpulsing in large pulse height hits. This is because both late-pulsing and afterpulsing appear as low pulse hits trailing the main hit. They therefore tend to increase $(t_b - t_a)$, but have no effect on $(t_d - t_c)$

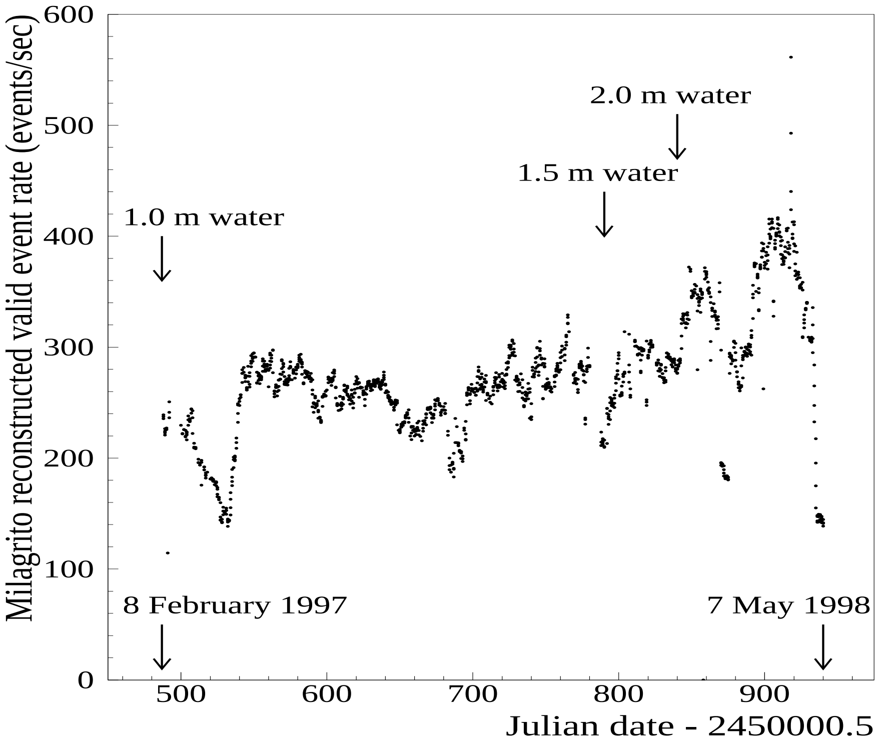

Figure 2.6: The daily trigger rate over Milagrito's lifetime. Milagrito was turned on 8 February 1997, and turned off 7 May 1998. The dates when the water depth was changed are indicated.

Milagrito also employed several *analog-to-digital conversion* (ADC) circuits, which were used for calibration of the TDCs.

A logical output signal, 150 ns wide, from each PMT discriminator was fed to the trigger electronics, and these were added together. If the sum of the logical output pulses exceeded the equivalent of 100 PMTs fired, then a trigger was recorded. The output of all the TDC and ADC boards were sent to the data acquisition computers, along with a signal from the GPS clock to give the absolute time of the event.

The rate of triggers varied strongly as a function of the number of PMTs required to fire in coincidence. This is shown Figure 2.5.

2.2 Detector Performance

Milagrito began recording data on 8 February 1997. It amassed a data set of $\sim 8.9 \times 10^9$ events by recording air showers at a rate of 300-400 events per second before it was shut off on 7 May 1998 to begin the installation of the full Milagro detector.

Figure 2.6 shows Milagrito's average daily trigger rate as a function of time. The rate dropped in the winter of 1997, mjd 50500-50550, due to snow on top of the pond cover. It was then roughly constant until the water depth was changed, around mjd 50790 and then again around mjd 50870. Shortly after the water depth was increased to 2.0m, the rate dropped again due to snow on the cover, but it then rose again after the snow melted and was pumped off the cover. The rate dropped off quickly at the very end because data were recorded while the pond was drained of water.

2.2.1 Calibrations

Nitty-gritty details of the Milagrito calibration can be found elsewhere [37]. What follows here is a quick summary of the major issues.

There were four main issues in the calibration of Milagrito:

- The *time pedestal*, which is the time offset between the arrival of a signal at a PMT and the arrival of a digital signal at the trigger electronics,

- The *time slewing*. This stems from the fact that the rise-time of a PMT signal

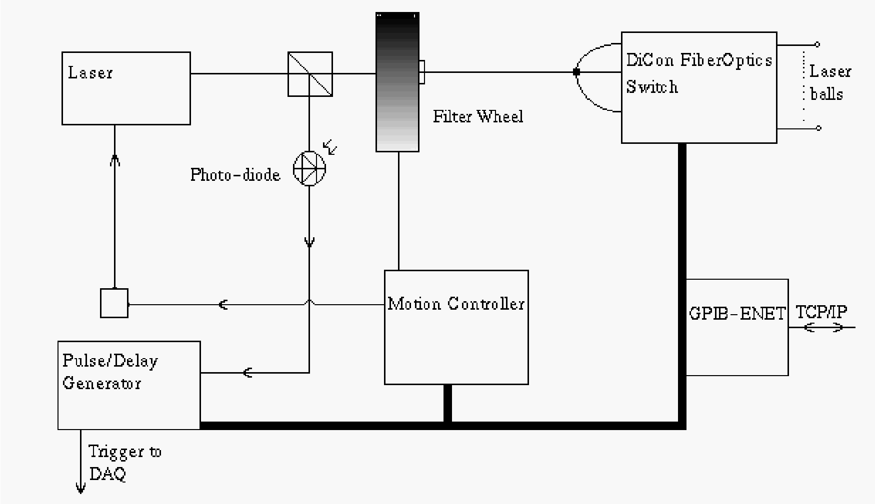

Figure 2.7: Milagrito's laser calibration system.

does not change as a function of pulse height, but the slope of the voltage versus time curve does. So, a low pulse height hit, which has a relatively low rise-time slope, crosses the discriminator threshold later than would a high pulse height hit, because of the larger slope of the high pulse height hit,

- The conversion factor between TOT and the number of PEs emitted by the PMT,

- When to stop using the low TOT and switch to high TOT to measure and record the pulse height of a hit.

The Milagrito calibration system is illustrated in Figure 2.7. A pulsed nitrogen laser was used as a source of 500 nm light, which was directed into a beam splitter. One of the beams was sent to a photodiode and from there to a pulse generator used to trigger the DAQ electronics. The other beam was sent through a filter wheel that

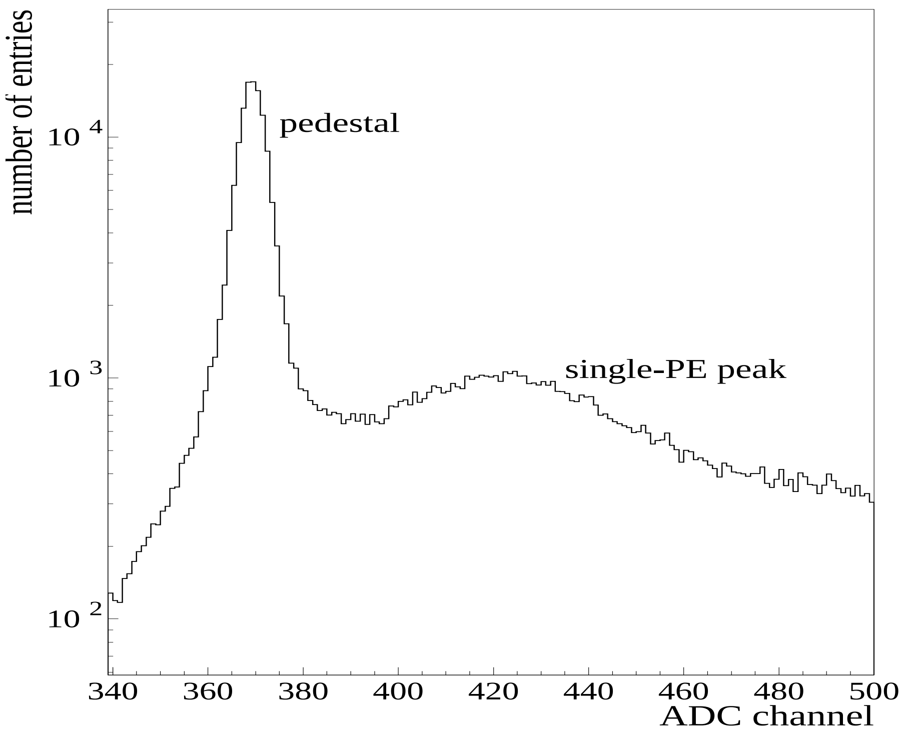

Figure 2.8: ADC spectrum of a typical Milgarito PMT. The pedestal and single PE peak are indicated.

could be used to vary the intensity of the light by over four orders of magnitude. The output from the filter wheel was sent through a system of fiber optic cables into the pond. An isotropic diffuser, in the form of a small bead of epoxy, was installed at the end of each fiber optic cable. These were called the laser-balls. The laser calibration system was used to determine the slewing and time pedestals for each PMT, and the high TOT threshold. The TOT-PE calibration was done using the ADC circuits.

Figure 2.8 shows a typical ADC spectrum for a Milgarito PMT. Each entry in the histogram is the ADC output of this PMT for a Milagrito trigger, i.e. for an air shower event. The spectrum displays two prominent features: the pedestal and the single PE peak. The pedestal represents the PMT output when it was not hit by any Cherenkov light, and the single PE peak is the PMT output when it was triggered by a single proton. Thus there is a natural way to calibrate a PMT using an ADC: measuring the separation between the pedestal and the single-PE peak gives the average ADC value that results from a single photon triggering the PMT. Thus the ADC value of any PMT pulse divided by the number of ADC counts between pedestal and single-PE gives the amount of charge in the PMT output pulse, in units of PEs. It should be noted that the ADC pedestal is not the same as the timing pedestal discussed earlier.

Now to calibrate the TOT, the PMTs are read by both ADC and TOT systems simultaneously. Comparing the TOT output for each to the calibrated ADC output for the same PMTs yields a calibration between TOT and PEs.

2.2.2 Event Reconstruction

As mentioned in Section 1.2.4, the first step in the reconstruction of an air shower event is the location of the shower core. Milagrito employed a simple center-of-gravity core finder, based on the number of PEs from each PMT hit by Cherenkov light. If N PMTs are hit, the x and y position of each PMT are designated x_i and y_i where i runs from 1 to N, and x and y are the local pond coordinates. Then the x position of the core is given by,

$$x_c = \frac{\sum_i^N PE_i \times x_i}{\sum_i^N PE_i}, \tag{2.2}$$

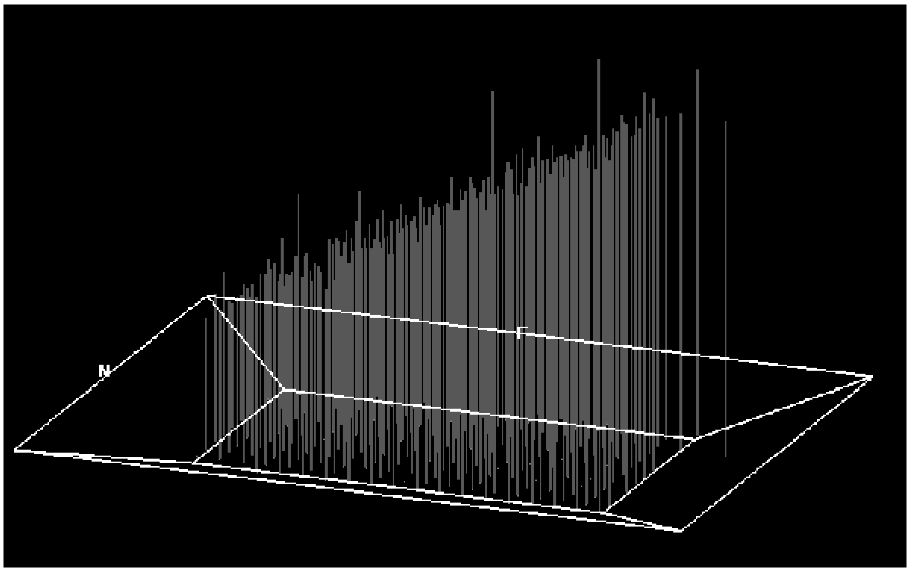

Figure 2.9: A typical Milagrito event. The height of each vertical line is proportional to the relative arrival time of the first Cherenkov photon to hit the PMT located at that spot in the pond.

and the y position is found similarly.

Milagrito's angular resolution suffered from poor core resolution, stemming from the physical area of the detector, which is smaller than the lateral size of typical TeV air showers at altitudes around 2500m. This leads to an inability to distinguish a shower whose core impacted the top of the pond from a shower whose core impacted the ground away from the pond. A large shower whose core hit the ground away the pond, called an *off-pond* event, can still trigger the detector. The distribution of particles across the pond from such an event could be very similar to the distribution of particles from a smaller shower that landed on the pond, called an *on-pond* event. The center-of-gravity core finder never places a core off the pond, so the result is that the two showers can be mistakenly reconstructed as similar events, when in fact they

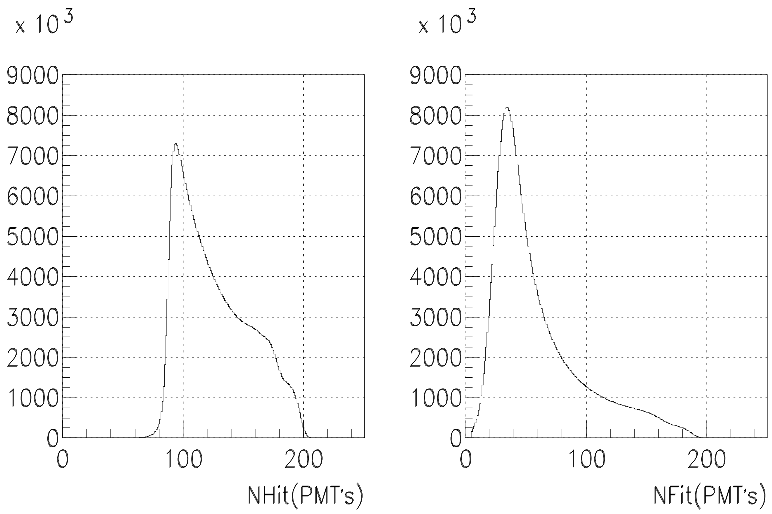

Figure 2.10: Nfit and NHit distributions, from Milagrito moon data: events in the declination band of the moon. The left plot shows NHit, the number of PMTs hit with Cherenkov light, and the right plot shows NFit, the number of PMTs used in the reconstruction of the incident angle of each shower. Each plot contains 4.05×10^8 events.

were quite different. More advanced core-finding algorithms, capable of placing cores off the pond, are being developed for use in Milagro.

Once the core of the shower is located, the direction of the shower plane can be determined. First the sampling and curvature corrections are applied, which is done to bring the times of the PMT pulses into a plane. The shower plane is fit by minimizing χ^2,

$$\chi^2 = \sum_{i=1}^{NHit} w_i(ct_i - ct_0 + \hat{\imath}x_i + \hat{\jmath}y_i + \hat{k}z_i)^2, \tag{2.3}$$

where t_0 is the arrival time of the shower plane, and t_i and the x_is are the times and locations of the PMTs hit by Cherenkov light. NHit is the number of PMTs

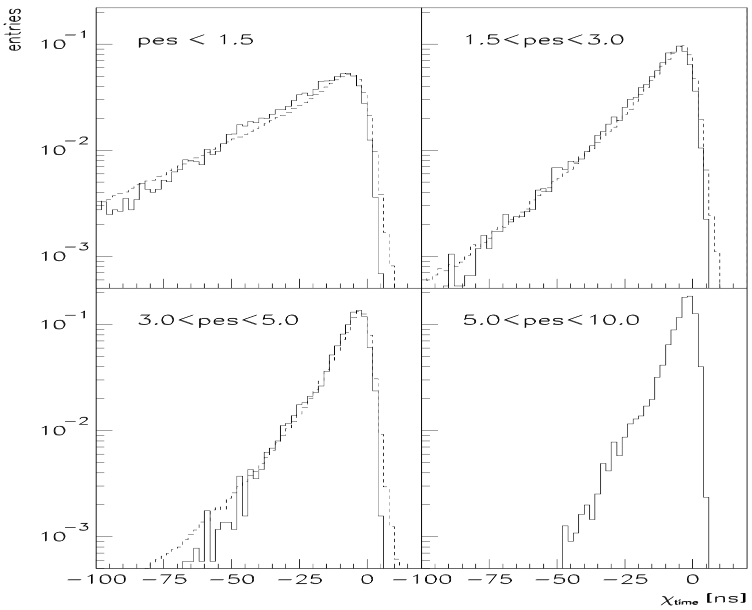

Figure 2.11: χ_{time} distributions for Milagrito data. χ_{time} is the difference between the shower plane and the measured PMT time. Negative values of χ_{time} correspond to later times.

hit. The $\hat{\imath} - \hat{\jmath}$ plane is parallel to the surface of the pond and the $\hat{k}$ direction is down. The parameters w_i are the weights given to each PMT pulse, based on the measured pulse height and the distance of the PMT from the core position. The angle fitting algorithm performs four iterations, with varying w_i cuts for each step. All PMTs hit with fewer than 2 PEs were rejected by the angle fitter. The number of PMTs used in the final iteration is called NFit. Figure 2.10 shows the NHit and NFit distributions for a typical Milagrito data run. Approximately 90% of Milagrito's triggers were successfully reconstructed as air shower events. The other 10% of the triggers are believed to be due to energetic muons passing horizontally across the pond, and single hadrons.

As described in Section 1.2.3, the average size of extensive air showers at a given

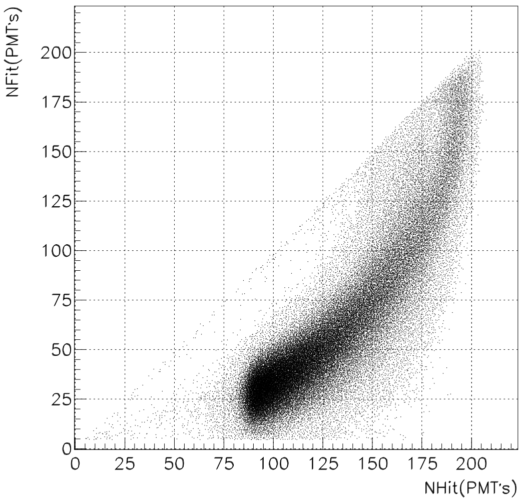

Figure 2.12: Scatter plot of NFit versus NHit for the Milagrito moon data.

atmospheric depth depends on the energy of the primary cosmic ray. Since NHit depends on the number of shower particles in the pond, it is related to the shower size. Thus NHit also depends on the energy of the primary particle. Figure 2.12 shows a scatter plot of nFit versus NHit for the data shown in Figure 2.10. The relationship between the two is not linear, but it can nonetheless be seen that the lowest nFit events correspond to the lower NHit events, and the high nFit events are the high NHit events. It follows, therefore, that nFit depends on the energy of the primary particle. This will be demonstrated more convincingly in Section 3.14.

Figure 2.9 shows a diagram of a typical Milagrito event. Each of the vertical lines represents a PMT that was hit by Cherenkov light from the shower front. The height of the line is proportional to the relative arrival time of the pulse at that

PMT. The shower plane is clearly seen. As mentioned in Section 1.2.3, the shower front is not actually planar, but conical. Therefore, timing corrections are made to the PMT pulses based on the pulse heights of the hits and the distance from the core. The pulse height corrections are meant to overcome the sampling error, which stems from the longitudinal distribution of particles relative to the shower front. The timing corrections are meant to overcome the curvature of the shower. Monte Carlo simulations indicate that the application of a 0.04ns/m correction to the arrival time of the PMT pulses improves the angular resolution of the detector.

Even with the above corrections, the time distributions of the PMT pulses are not normally distributed. The quantity χ_{time} is defined as the difference in time between the shower front arrival time and the arrival time of a given PMT pulse. Figure 2.11 shows the χ_{time} for four different pulse height ranges. If timing errors were due only to random fluctuations, one would expect the χ_{time} distributions to be well fit by Gaussian functions. However, each χ_{time} distribution has a non-Gaussian tail due to late light, and the tails are longer for low pulse height events. Much of the late light stems from the PMTs sensitivity to horizontally moving Cherenkov light. This is discussed in greater detail in Section 3.2.2.

2.2.3 Angular Resolution

Because of the issues discussed above, the reconstruction of air shower events by Milagrito was imperfect. The degree to which the reconstruction was imperfect must

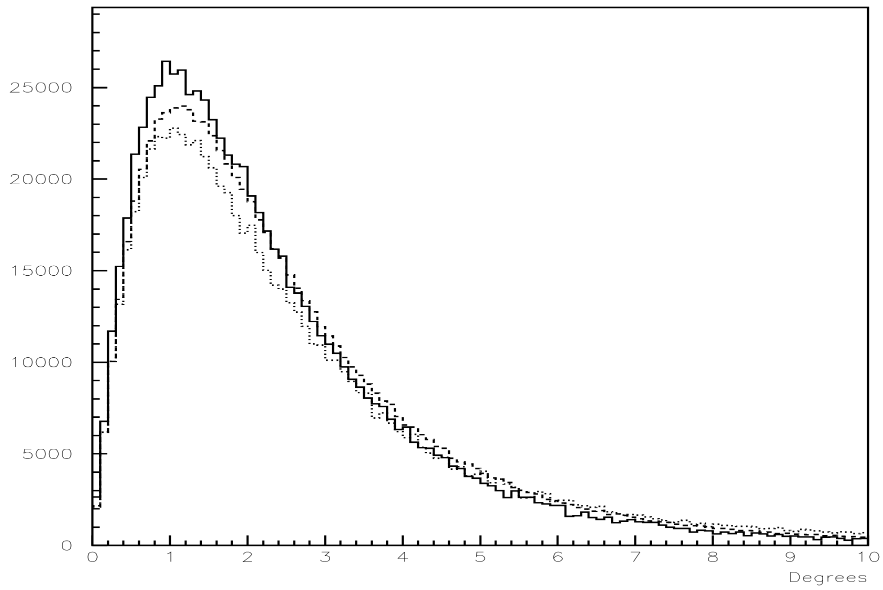

Figure 2.13: DELEO of distribution of Milagrito events.

be studied in order to judge the results of any analysis done on Milagrito data. The average error in reconstruction of the incident direction of cosmic ray triggers is called the angular resolution, and it is one of the most useful parameters for gauging the capabilities of an EAS array.

Milagrito's angular resolution is expected to vary with NFit. As anyone who has ever performed a χ^2 minimization can attest, the accuracy of the procedure is generally improved with more data points. So it is with Milagrito's event reconstruction: more PMTs used in fitting the shower front to a plane means a better fit. Thus events with high NFit are expected to be better fits than events with low NFit.

The quantity DELEO is a quick measure of the angular resolution of any EAS array, and it requires only the data itself to calculate it. DELEO is found by separating the array into two interspersed sub-arrays and reconstructing each event as if it were two separate events detected by the two separate sub-arrays. Then DELEO is defined as the space angle difference between the reconstructed angles of the two events. The name DELEO comes from the way the array is divided up. Alternating tubes are assigned to each sub-array as if they were simply numbered and the odd numbered tubes were assigned to one array and the even numbered tubes assigned to the other array. Thus DELEO is Δ-Even-Odd.

DELEO is used, for example, to find the proper curvature and sampling corrections for the event reconstruction algorithms. By applying the different corrections on a small data set and plotting DELEO each time, a judgment can be made about the effectiveness of the corrections. Additional discussion of DELEO and more ways of measuring the angular resolution are to be found in Section 3.2.2 and 4.6.

2.3 Online and Offline Data Processing

Milagrito's triggered events were reconstructed automatically in real time by the DAQ system, and stored on DLT-format digital magnetic tape. The raw data, meaning all the TOT information for each PMT and the GPS times, were also saved and stored on DLT. After Milagrito was turned off, all of the raw data were reconstructed again offline using the final calibration data and sampling and curvature corrections. The re-reconstructed data were stored in a compressed format on disk in Los Alamos and made available for analysis work. In addition to the full data set, several “stripped” sub-sets were created. These consisted of only those events in the declination bands of specific objects to be studied, such as the Crab Nebula or the moon.

Chapter 3

Simulations

The formulas given for Rossi's Approximation B and the NKG function in Chapter 1 (Equations 1.6-1.8 and 1.9-1.10, respectively) accurately describe the average development of an electromagnetic cascade. However, as noted in Section 1.2.3, individual showers are expected to deviate from these average distributions; this does not even take into account the deviations stemming from the nuclear interactions in the hadronic core of an air shower. Thus to study the variety and scope of deviations an experiment is likely to see, it is useful to simulate individual cosmic ray showers. While not a simple task, to be sure, it greatly facilitates the interpretation of data to have a large set of simulated events to compare to the data.

The results of an air shower simulation can give, for example, the number of secondary particles at ground level, and their positions, directions, and energies. But the data are comprised of times and heights of PMT pulses, so another important

Species	*Spectral Index*	Percentage of Milagrito Triggers
Protons	-2.80	68%
Helium	-2.64	28%
Nitrogen	-2.67	4%

Table 3.1: Specifics of Milagrito Simulations.

step remains. Simulated air shower events must be put into a detector simulation if any meaningful comparison to data is to be made.

3.1 Air Shower Simulations

The Milagro collaboration uses the CORSIKA routines developed by the KASCADE group to simulate extensive air showers [38, 39, 40]. This software can be used with several different high energy hadronic simulation packages. The Milagrito simulations were done using the VENUS (Very Energetic Nuclear Scattering) [41] package. VENUS simulates particle creation through interaction and fragmentation of color strings, but does not produce jets. Below energies of 20 PeV this is omission is valid and the authors of CORSIKA recommend the use of the VENUS package [38]. For low energy hadronic interactions, Milagrito simulations used the GHEISHA package, and for electromagnetic cascades the EGS4 package was used.

Extensive air showers initiated by protons, helium nuclei, nitrogen nuclei, and γ-rays were simulated using CORSIKA, and stored on disk for input into the detector simulation. All primary particle energies were distributed according to a power law energy distribution. Table 3.1 gives the spectral indices used for each species, and the percentage of Milagrito's triggers comprised by each species.

3.2 Detector Simulations

The Milagrito detector was simulated using the GEANT package (Version 3.2) from CERNLIB [42]. The GEANT code was used to simulate the pond, the PMTs, and the electronics. It simulates the hadronic and electromagnetic interactions of the shower particles with the pond water, including the production of $\delta - rays$ and Cherenkov radiation.

The CORSIKA output is used as input for the GEANT simulation. The CORSIKA output file specifies the incident angle and energy of the primary particle along with the information for the secondary particles; the core location with respect to the pond is chosen randomly. The secondary particles from the air shower are then distributed across the top of the GEANT pond accordingly. Next they are propagated and allowed to interact, causing emission of Cherenkov photons. These photons are tracked, and some of them interact with the PMTs resulting in simulated electronic signals. The PMTs and electronics are also simulated, taking into account such things as the quantum efficiency of the PMTs, and the timing jitter of the output pulses. If at least 100 PMTs produce 1 PE or more, this is called a triggered event. The pulse heights and arrival times of the Cherenkov photon hits in the PMTs are stored in the standard Milagrito data format as if they were from a real event. This process is

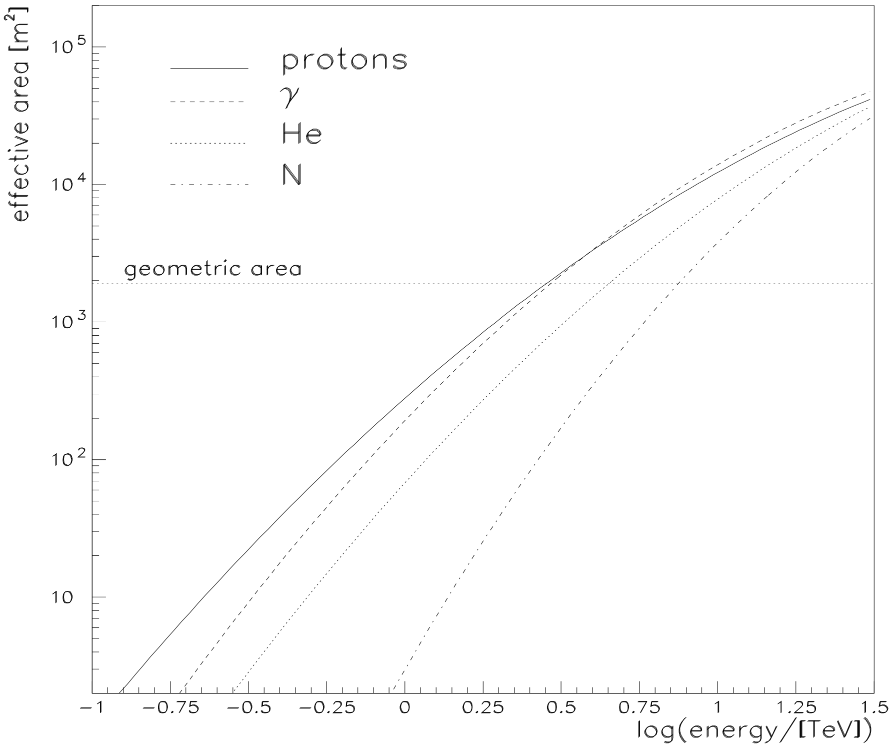

Figure 3.1: Effective Area of Milagrito, calculated by throwing events uniformly in solid angle for zenith angles from 0° to 45°.

called *throwing* a Monte Carlo event.

3.2.1 Effective Area

The effective area of an air shower detector is a parameter similar to the cross-section used in particle and nuclear physics. It is calculated through simulations in the following way. Many air showers are thrown uniformly over a large area, A_{throw}, much larger than the area of the detector itself, and those that trigger the detector are counted, N_{trig}. The effective area, A_{eff}, is given by,

$$A_{eff} = A_{throw} \frac{N_{trig}}{N_{throw}} \tag{3.1}$$

where N_{throw} is the number of thrown events. This can be done for different nuclear species, and over various energies and incident angles. The results of the Milagrito simulation are shown in Figure 3.1. This plot shows the effective area as a function of energy for the different primary species. It was made by randomly throwing events uniformly in solid angle from all zenith angles up to 45°.

Some interesting properties of air showers can be seen from this plot. Consider the effective area curves for protons and for γ-rays. At high energies, above $\sim$3 TeV, the effective area of Milagrito as seen by γ-ray initiated showers is larger than the effective area for proton-initiated showers at the same energies. But as energy decreases, the effective area of proton showers falls off more slowly than does the effective area of γ-ray showers, so that below $\sim$3 TeV, the effective area of protons is larger than that for γ-rays.

Recall from Figure 1.3 that the average number of secondaries in a 500 GeV γ-ray shower is greater than in a proton shower of the same energy. This is what causes the γ-ray effective area to be larger at higher energies. Since the γ-ray showers tend to have more secondary particles than showers initiated by protons of comparable energy, they are likely to produce more Cherenkov light in the pond than proton showers.

This tendency is strengthened by the distribution of secondary particles. A 1 TeV proton initiated air shower can be thought of as a superposition of smaller size γ-ray showers, each of whose cores is pointed slightly off-axis from the core of the main shower. This is due to the nuclear fragmentation that occurs early in the development of a proton shower. The nuclear fragments lead to electromagnetic cascades, but the cascades are not centered about the shower axis. A proton shower can therefore have more lateral spread in its secondary particle distribution. On average, the lateral spread follows the NKG function quite closely [16], but there tend to be more fluctuations in proton showers than in γ-ray showers. And it is this lateral spread fluctuation that causes the proton shower effective area to fall off more slowly than the γ-ray effective area. A proton shower that has a large nuclear fragment form early on in its development and project itself off the core axis can trigger the detector even if the core lands far from the pond. But a γ-ray shower is essentially one large electromagnetic cascade, so the average particles distribution of γ-ray showers is smoother than it is for hadronic showers. This contributes to the problem of core location, making it more difficult to locate the cores of hadronic showers than γ-ray showers.

3.2.2 Angular Resolution

This section continues the discussion of angular resolution started in Section 2.2.3.

Delangle

The parameter Delangle is defined as the space angle difference between the simulated incident direction and the reconstructed direction. Hence the name "Delangle"

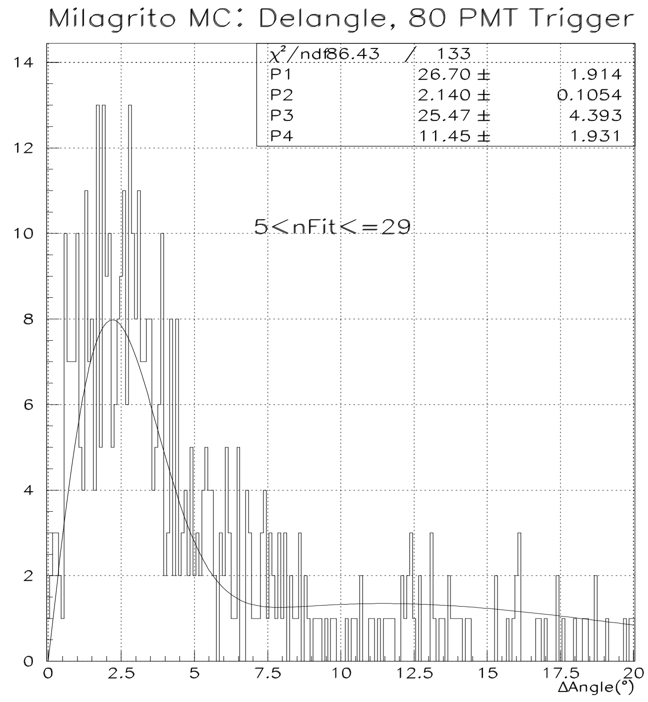

Figure 3.2: An example Delangle distribution. The histogram is assumed to be distributed as a sum of two Gaussian functions. One Gaussian describes the peak of the distribution, and the other Gaussian describes the tail. Fits are made to find the widths of the two Gaussians, and the widths are used in Figure 3.3.

is an abbreviation of ΔAngle. It is the truest measure of angular resolution, but it exists only for Monte Carlo events. It was calculated for each Monte Carlo event, and the results were assembled into histograms in seven bands of NFit. The Delangle distributions were then fit to Gaussian functions. Delangle was found to be a strong function of NFit, as expected.

Delangle was assumed to be distributed in θ-ϕ space as a symmetric 2-dimensional Gaussian. In other words, it was assumed that there was no bias in either the $\hat{\theta}$ or $\hat{\phi}$ directions. With only one major exception, discussed in Section 3.2.2 below, this

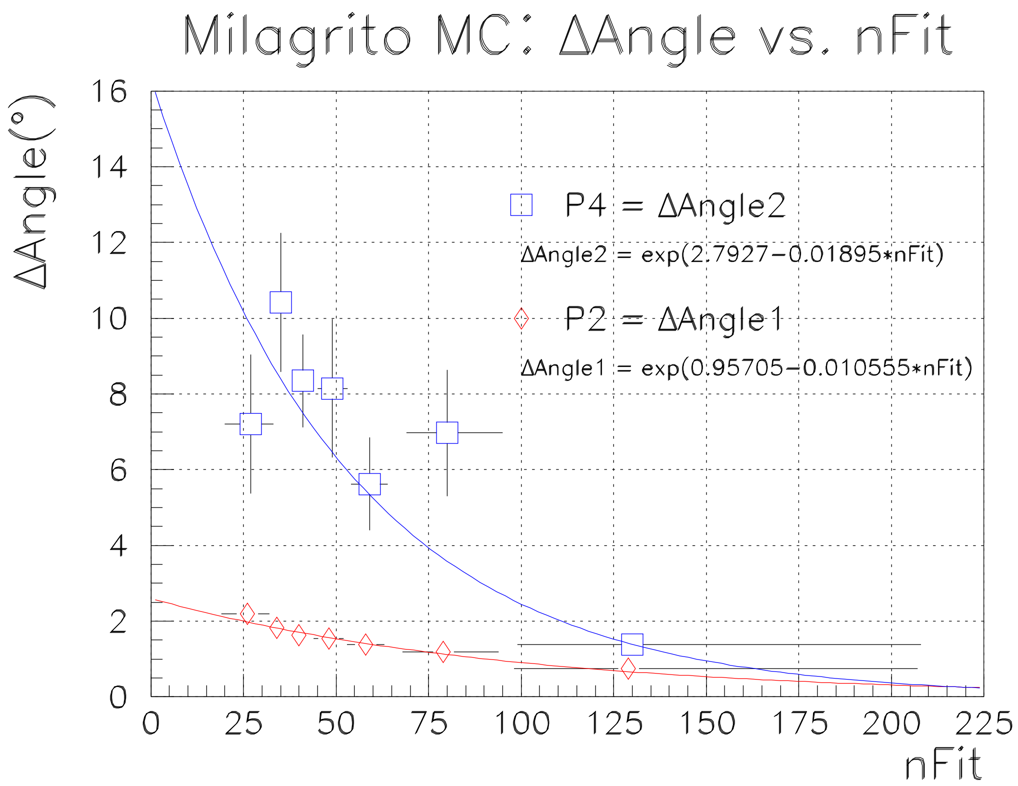

Figure 3.3: Delangle Gaussian peaks shown as a function of NFit. The points plotted here are taken from fits similar to Figure 3.2. On the abscissa, the position of the point is placed at the median value of NFit, and the error bars represent the band containing 90% of the data for that NFit band.

was found to be true.

The projection in r of a 2-dimensional, symmetric Gaussian is $r \times Gaussian$, so the Delangle distributions should be well fit by $r \times Gaussian$ if the assumption is correct. This was found to be the case, with the exception of some long tails on the high side of the peak that were more prevalent in the low NFit bands than in the high. To account for this, Delangle was taken to be the projection in r of a sum of two

2-dimensional Gaussian distributions, allowing the width and overall normalizations of the Gaussians to vary independently. The use of two Gaussians yielded better fits to the data, shown by lower χ^2 of the fits using two Gaussians. With two Gaussians in the fits, one of the Gaussians accounts for the peaks and the other for the tails of the distributions. This is illustrated in Figure 3.2. The effect of each Gaussian is clearly seen: the "peak" Gaussian has a width of 2.14°, and the "tail" Gaussian has a width of 11.45°. The effect of the sum is to fit the distribution, incorporating the long tail more effectively than a single Gaussian.

With this method, Delangle was characterized by two widths, each of which was found to be a strong function of NFit, as shown by Figure 3.3. The widths (σ) of the Gaussians used in the Delangle fits are plotted against NFit in this figure, and these were fit to exponential functions; the "tail" widths and the "peak" widths are each fit separately as an exponential function of NFit. The results of the fits were used in further simulations to characterize the angular resolution of the detector. The fit parameters are shown in Figure 3.3.

DELEO

Delangle can be calculated only for Monte Carlo events, because it is the difference between the incident angle of the primary cosmic ray and the reconstructed angle. The true incident angle of a detected air shower is, of course, unknown, so Delangle cannot be used with data. The quantity DELEO (see Section 2.2.3) is used instead

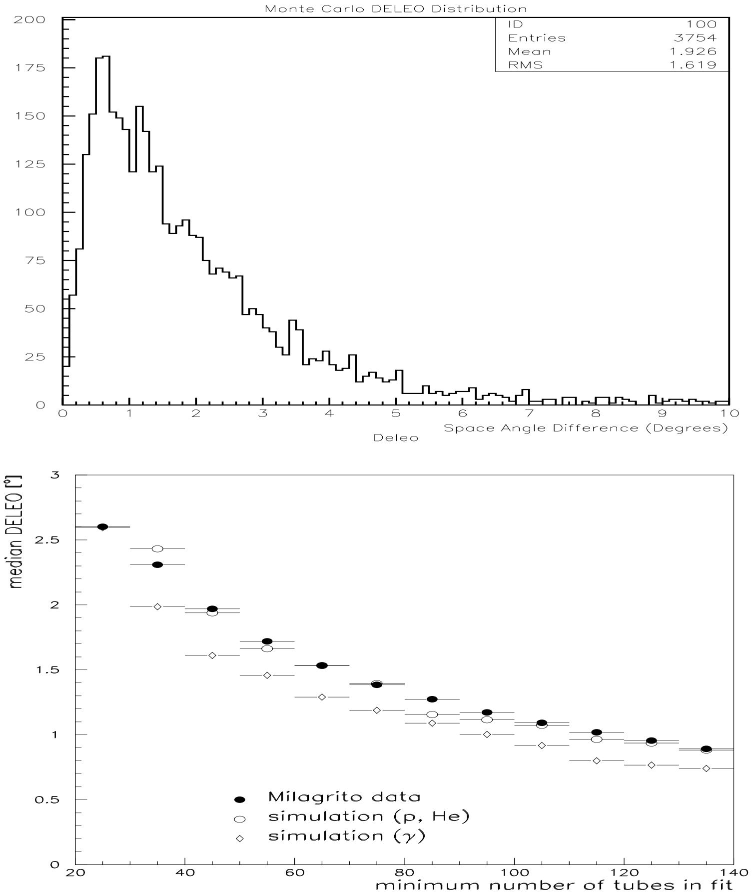

Figure 3.4: DELEO plots. The top plot shows the DELEO distribution of simulated Milagrito events. The bottom plot shows the median values of DELEO as a function of NFit. Simulated events and data events are plotted.

to characterize the angular resolution of data.

DELEO is expected to be approximately twice the angular resolution of the detector [43]. This was tested for simulated Milagrito events by comparing the peaks and median values of the DELEO and Delangle distributions. This was found to be true, so it was then concluded that DELEO is a good measure of the angular resolution for Milagrito data. Figure 3.4 shows the DELEO distribution for simulated events; compare this to Figure 2.13 which shows the DELEO distribution for Milagrito data.

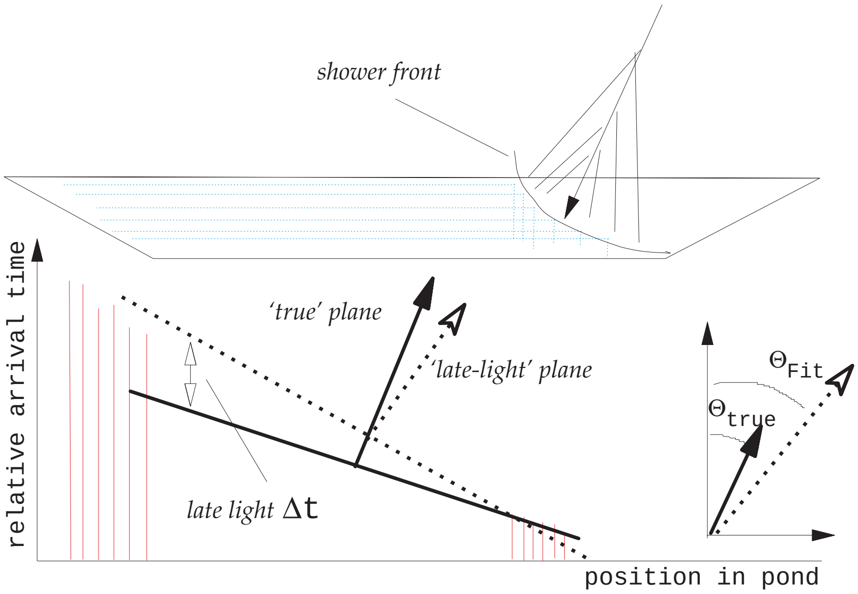

Figure 3.5: Simplified diagram of the cause of the $\Delta\theta$ versus θ systematic offset. The shower front particles cause Cherenkov emission vertically and horizontally, as shown in the upper part of the diagram. The lower part shows the relative arrival times of hits in pond PMTs. If the shower were fit to a plane using only the PMT hits on the right, which are the PMTs hit by the prompt light, then the reconstructed angle would be θ_{TRUE}. But with the late PMT hits on the left side of the pond, the fitted plane indicates an incident angle θ_{FIT}.

Figure 3.4 also shows the median DELEO values as a function of NFit for data and simulated events. It can be seen that the data and the simulated hadronic events are in good agreement.

Systematic Pointing Errors: $\Delta\theta$ versus θ

Delangle and DELEO are excellent measures of the uncertainties in event reconstruction that stem from things like random PMT timing and pulse height errors. But they are both incapable of exposing the effects of systematic biases in the detector. DELEO is also insensitive to core resolution errors. So additional checks on the angular resolution are needed. By applying such checks, a systematic reconstruction error in Milagrito was found.

The reconstruction of Milagrito events is affected by horizontally moving Cherenkov light from the shower front. Figure 3.5 illustrates the effect. As described in Section 1.2.2, shower front particles cause Cherenkov emission in a cone of opening angle 41°. For charged particles entering the pond from zenith angles near 45°, some of the light is emitted downwards and is detected promptly by the nearby PMTs. Some of the light, however, is emitted approximately horizontally, and travels across the pond before being detected by more distant PMTs. Since the horizontal Cherenkov light traverses a longer path length to reach a PMT than the downward emission from shower front particles that enter the far end of the pond, this horizontal light arrives later than the prompt Cherenkov emission from the shower front particles as they pass through the far end of the pond. Thus if the PMT is hit by the horizontal light from the shower front particles at the far end of the pond and not the prompt light from the nearer shower front particles, the PMT pulse will be late compared to the shower front plane. The effect is exacerbated because the Cherenkov light travels at c/n in the pond, which is slower than the shower particles themselves, which travel very close to c. These late PMT hits, if not rejected by the angle fitter, will cause the shower plane fits to be skewed systematically toward the horizon, as illustrated in Figure 3.5. This will tend to make θ_{Fit} larger than θ_{Throw}, causing the so-called $\Delta\theta$ *versus* θ systematic pointing error.

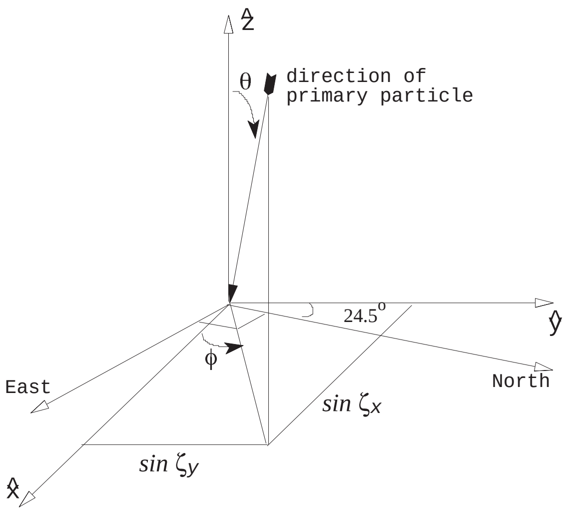

Figure 3.6: Diagram of the definitions of the parameters ζ_x and ζ_y. Each is the projection of a unit vector in the direction of the primary particle onto the x or y axis.

To study this effect, a new parameter was defined. A projection of the unit vector in the direction of the incident particle's momentum onto the x-y axis of the pond was made. The x-axis of the local pond coordinate system lies 24.5° north of east; it runs through the center of the pond the long way. Two parameters, ζ_x and ζ_y, were then defined as follows:

$$\zeta_x = \sin^{-1}(\sin\theta \cdot \cos\phi) \tag{3.2}$$

$$\zeta_y = \sin^{-1}(\sin\theta \cdot \sin\phi). \tag{3.3}$$

Figure 3.6 illustrates the definitions of the new parameters. (In the text, ζ is used with no subscript to mean *both* ζ_x and ζ_y.) For each Monte Carlo event, $\Delta\zeta = \zeta_{Fit}$ - ζ_{Thrown} was calculated, and fit to a straight line as a function of ζ. Because the Monte Carlo events were thrown only out to 45°, there is an "edge effect" at large

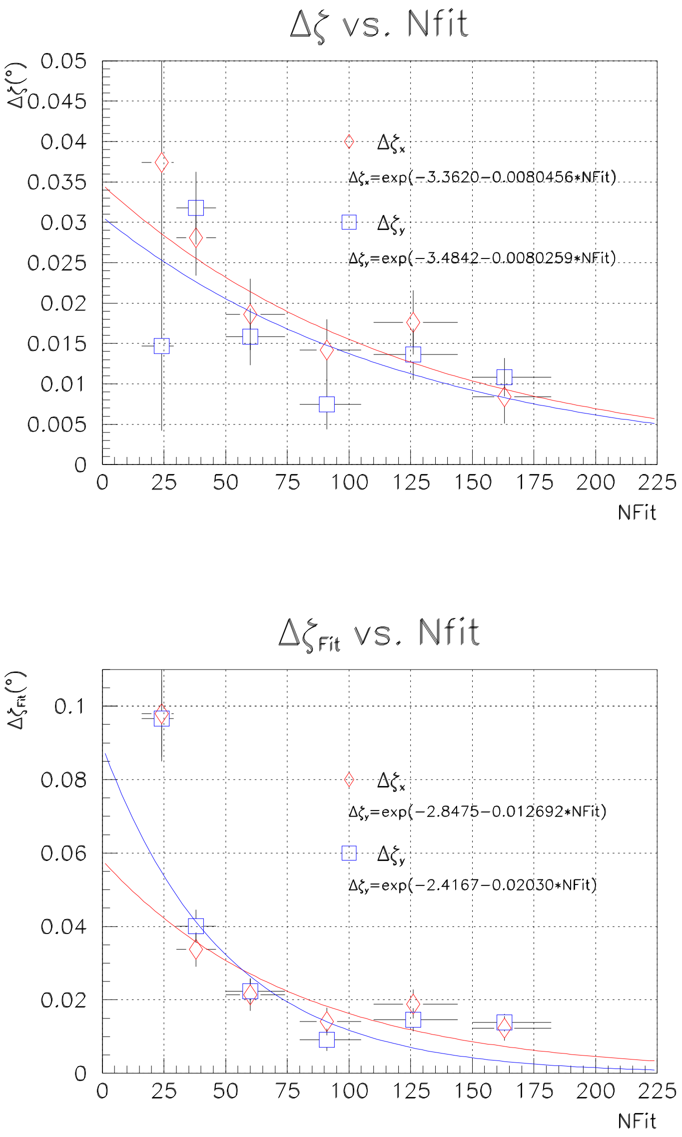

Figure 3.7: Simulated $\Delta\zeta$ plots. The top plot shows $\Delta\zeta$ values versus NFit. These values are used in the simulation of the moon shadow. The bottom plot shows $\Delta\zeta_{Fit}$ values versus NFit. These values are used to correct the $\Delta\theta versus \theta$ systematic offset in the data, and in the simulation of the shadow of the moon.

angles. This is because it is possible for primary events below 45° to be reconstructed above 45°, but there are no compensating events from primaries above 45° to get reconstructed below 45°. This will lead to an exaggeration of the systematic offset near 45°, which gets worse as the magnitude of the offset, or the width of Delangle, gets larger. Edge effects notwithstanding, the Monte Carlo predicts that the systematic offset is a function of NFit, as shown in Figure 3.7.

All fits were generated using the same Monte Carlo events. The $\Delta\zeta$ versus ζ fits can be thought of as the systematic offset itself, since they show the systematic pointing error as a function of the true incident angle. The $\Delta\zeta$ versus ζ_{Fit} fits can be used to correct the systematic offset, since they give the offset as a function of the fit angle. This is an event by event correction, but it can be applied after reconstruction of the events. For each event, with local coordinates θ and ϕ calculated using the χ^2 angle fitter, the parameters ζ_x and ζ_y are calculated from θ and ϕ. The magnitude of the correction is taken from the curves in the bottom plot of Figure 3.7. These quantities $\Delta\zeta$ are subtracted from ζ_x and ζ_y, and the new parameters, ζ'_x and ζ'_y, are converted back into local coordinates and assigned to the event, which then has a new direction in local coordinates, θ' and ϕ'.

It is interesting to note that the two parameters, ζ_x and ζ_y, affect the moon shadow differently. This stems from the fact that the majority of the moon data come from the southern part of the sky. This means that most events in the moon shadow data have negative values of ζ_y, whereas they are symmetric about ζ_x=0. The $\Delta\zeta$ systematic offset tends to increase a positive ζ and decrease a negative ζ, so that the effect of the systematic on a set that is distributed about 0, like ζ_x, is to spread the shadow but cause no net offset. In the case of ζ_y, on the other hand, the data are mostly negative, and so the effect is a net offset toward smaller ζ_y along with spreading the shadow. Because of this, the δ offset of the moon shadow can be corrected with just a ζ_y correction, but using both ζ_y and ζ_x corrections should also tighten the moon shadow.

3.3 Cosmic Ray Tracking

Figure 3.8 illustrates the cosmic ray tracking method. The geomagnetic deflection of cosmic rays is simulated by starting with a cosmic ray of known charge, Ze, and mass, m, located at the pond and projecting that cosmic ray toward the position of the moon, designated *"moon"* in Figure 3.8. This is the direction opposite to the direction actually traversed by real cosmic rays coming from the moon to the earth. The geomagnetic field bends the path of the particle, so that it does not finish its motion at the position *"moon"*, but rather at some new position, *"moon′"*. The path traced by the cosmic ray in this way is the same it would trace had it started at *"moon′"* and moved *toward* the earth rather than away from it.

Two vectors can now be defined: one, $\vec{X}$, from the *pond* to the position *"moon"*, and a second, $\vec{X}'$, from the *pond* to the position *"moon′"*. The interpretation of these vectors in the context of the moon shadow simulation is tricky, but crucial. The vector

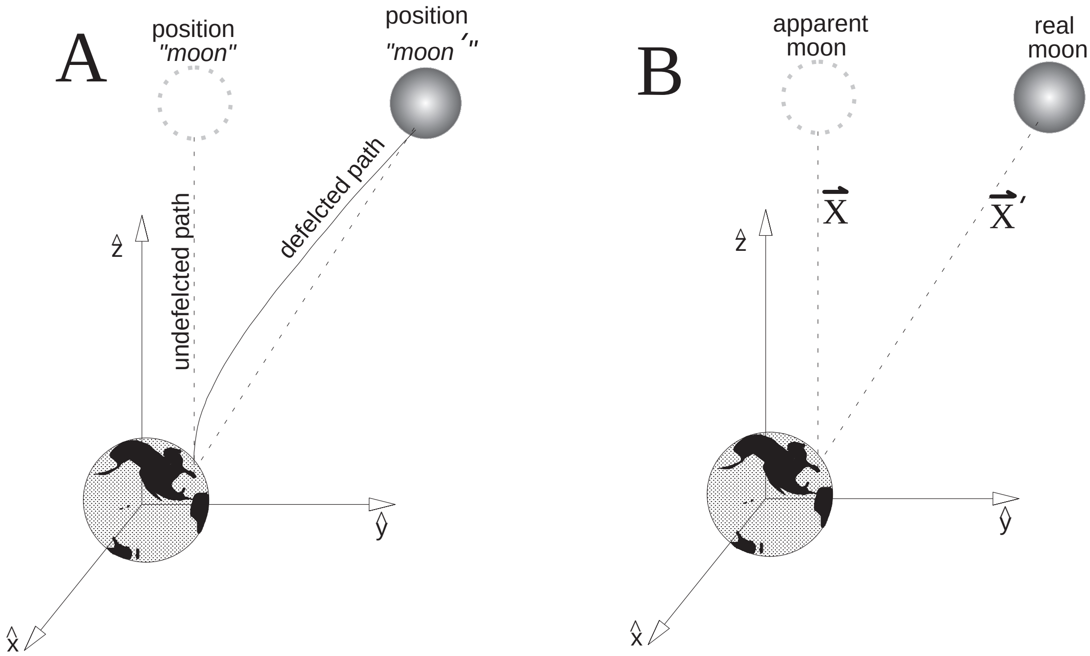

Figure 3.8: Diagram illustrating the cosmic ray tracking method. Cosmic rays are projected from the top of the atmosphere above Milagrito toward the position *"moon"*, and traced as they are deflected by the geomagnetic field. The deflected path leads to the position *"moon′"*, which is the true position of the moon.

$\vec{X}\prime$ is the line of sight from the pond to the true position of the moon, and $\vec{X}$ is the line of sight from the pond to the apparent position of the moon. In other words, $\vec{X}$ designates the path that photons would travel as they passed from the apparent moon position to the earth. But since cosmic rays are charged particles moving through a magnetic field, they follow a curved path between the moon and the earth. The cosmic ray paths are bent by the geomagnetic field, so that the momentum vector of a cosmic ray that traveled from the true moon position ("moon′" in Figure 3.8) to the earth is aligned with the vector $\vec{X}$ when it arrives at the pond. Thus projecting the direction of the final momentum vector of that cosmic ray back away from the

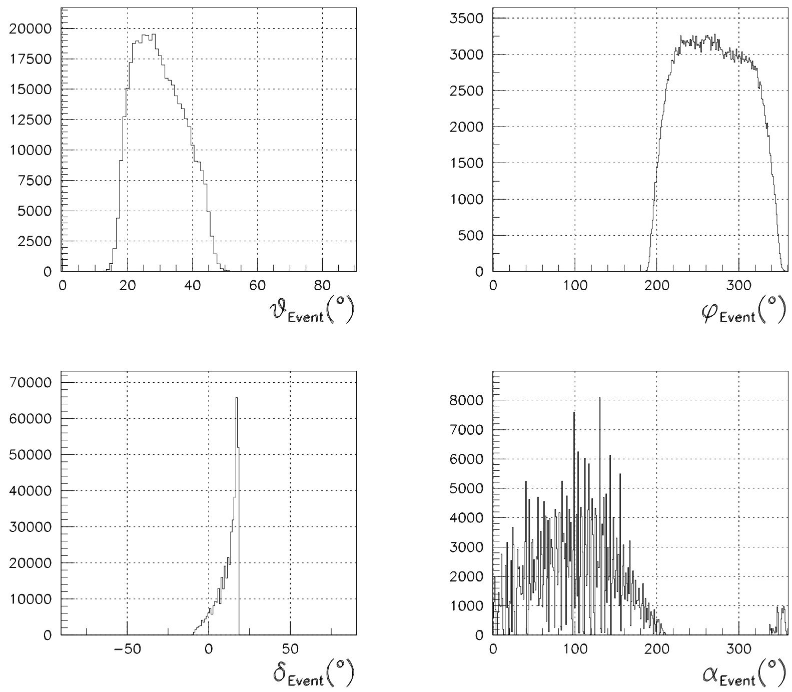

Figure 3.9: Simulated Milagrito angular distribution of events from the vicinity of the moon. The bottom two plots show in declination, δ, and right ascension, α, and the top two in zenith angle, θ, and azimuthal angle, ϕ. The absence of events from right ascensions between 200° and 300° is due to the fact that events were simulated only for zenith angles up to 45°. The event rate is a strong function of zenith angle.

earth makes it appear as if the cosmic ray originated at the position *"moon"*.

A look-up table of deflection values was assembled by projecting cosmic rays in the above manner for all positions of the moon in steps of 1°, and for several values of magnetic rigidity, from 100 GV/c up to 500 GV/c. Above 500 GV/c, the deflection of cosmic rays by the geomagnetic field was found to change inversely with the rigidity, so the deflection of cosmic rays above this rigidity is found by extrapolating the deflection of a 500 GV/c cosmic ray up to the higher rigidity.

The coordinate system used for the simulation is Cartesian, with the origin placed at the center of the earth. The z-axis intersects the geographic north pole, and the x-axis intersects prime meridian at the equator. The center of the earth is chosen as the origin, rather than Milagrito, because the distance from the moon to the center of the earth is very nearly constant, while the moon-Milagrito distance is not. The geomagnetic field used is a simple dipole field, with the point dipole itself pointed in the direction of the magnetic pole closest to the south geographic pole. The dipole field,$\vec{B}(\vec{x})$, at any point was calculated using a formula from [15]:

$$\vec{B}(\vec{x}) = \frac{3\vec{n}(\vec{n}\cdot\vec{m}) - \vec{m}}{|\vec{x}|^3}, \tag{3.4}$$

where $\vec{m}$ is the dipole moment and $\vec{n}$ is a unit vector in the direction of $\vec{x}$. The dipole approximation was tested by calculating the deflection of a 1.0TeV proton between the moon and the earth using the dipole field, and also using the World Magnetic Model [44]. The difference in the deflection between the two magnetic field models was less than 0.1°overall, and the difference stemmed primarily from low zenith angles, which were not used in this analysis. The dipole approximation was therefore deemed reasonable.

The bending is done in small steps, over which the magnetic field is assumed to be constant. In traversing a constant magnetic field, a charged particle follows a circular path whose radius, r, is determined by the rigidity, R, of the particle and the strength of the magnetic field, B,

$$r = \frac{R}{0.3B} \tag{3.5}$$

where r is measured in m, B in T, and R in GV/c [3]. So, in each step the magnetic field is calculated and the particle, located at $\vec{x}$ with momentum $\vec{p}$, is sent through its circular path. At the end of the step, the new position and momentum, $\vec{x'}$ and $\vec{p'}$, of the particle are calculated and used at the beginning of the next step. The steps are parameterized as a function of time; the new position and momentum of each step are found by calculating the motion of the particle at the old position with the old momentum and for a set period of time, Δt. The step size was determined by varying Δt for a test particle's trajectory until it was small enough that there was no noticeable change in the outcome by reducing it any further.

3.4 Moon Shadow Simulation

The results of the above analyses are used in the simulation of the moon shadow. The fake moon shadow is generated by throwing events from the moon's direction and then subtracting them from a simulated background. The energy and species of the primary particle are selected randomly from the proper distributions, as is NFit. Starting with the moon's position for a given day and time, the geomagnetic deflection is first applied. This is done as a function of rigidity for the three species of primary particles. The resulting deflected direction is taken as the incident direction of the cosmic ray, and this direction is smeared using the Delangle distributions and offset using the $\Delta\zeta$ fits. This accounts for the angular resolution of the detector and the systematic offset due to late light.

Figure 3.9 shows the angular distribution of the simulated triggers in the moon

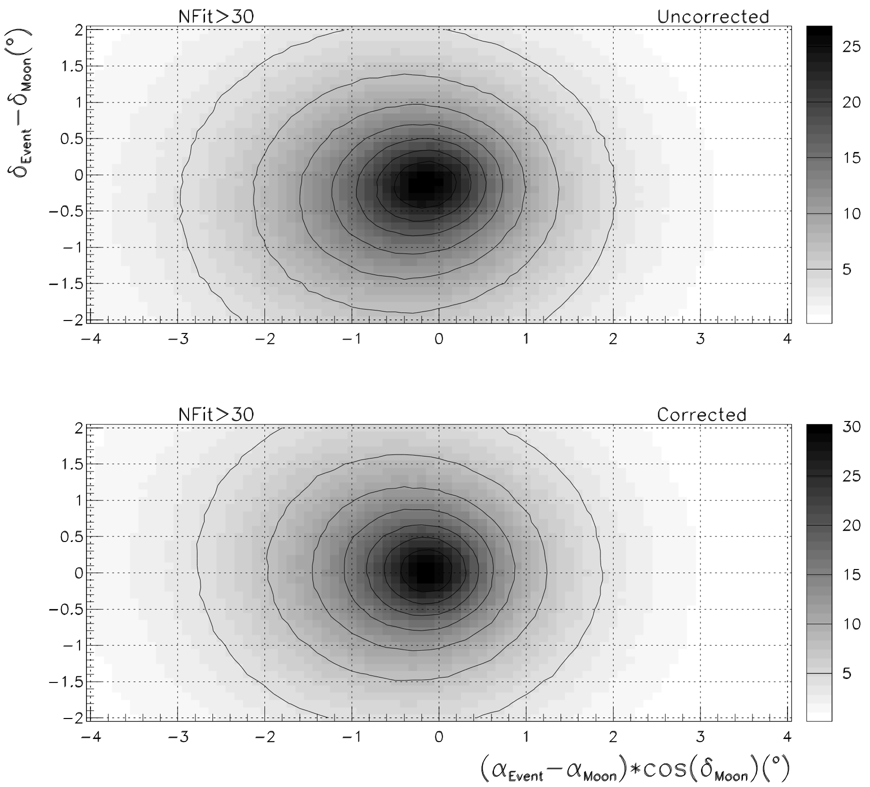

Figure 3.10: Simulated Milagrito moon shadow, "corrected" and "uncorrected" for the systematic pointing shift. This is the simulated shape of only those events that are blocked by the moon. The grey-scale given on the right of each plot indicates the number of events per 0.1°×0.1° bin.

shadow simulation. Only those events which would have come from the moon's position, but are blocked by its presence, are plotted. The peak of the zenith angle, θ, distribution is ~25°, and the tail of the distribution extends past 45°. Although no events were thrown from beyond 45°, some were reconstructed past this point. The azimuthal angle, ϕ, distribution is centered about 270°. The Milagrito simulations used a coordinate system in which ϕ was measured counterclockwise from the east.

Thus ϕ=270° is directly south.

The results of the moon shadow simulation are shown in Figures 3.10-3.14. These plots show the shape of moon shadow itself, meaning just those events that would be blocked by the moon. The behavior of the shadow is more easily studied this way, and then the shadow shape is subtracted from a background data set to generate the simulated moon shadow maps. The overall size of the shadow to be subtracted is determined by calculating the event density in the background data set, and multiplying the event density by the apparent solid angle of the moon ($\pi \times (0.26°)^2$). This is the true number of events that are blocked by the moon.

Over the course of a transit, the offset in declination, δ, due to the magnetic field is much smaller than the angular resolution of the detector. This is due to the direction of the geomagnetic field and the fact that the moon passes nearly symmetrically across the α component of the field. Thus, the only measurable net offset due to geomagnetic deflection is in right ascension, α, although the field does *smear* the moon shadow in δ. As mentioned in Section 3.2.2, it is the $\Delta\theta$ systematic offset that noticeably shifts the shadow of the moon in the δ direction. Because Milagrito sits in the northern hemisphere and, during Milagrito's lifetime, the moon's declination oscillated between $\pm \sim 18°$, the moon always appears in the southern part of the sky as viewed from Milagrito. Thus there is a systematic offset that is negative in declination. Applying the reverse offset to the data, event by event, should correct the $\Delta\theta$ systematic offset, and sharpen the shadow.

Median Magnetic Rigidity of Simulated Milagrito Triggers		
Species	*Moon Shadow*	*Sun Shadow*
Protons	2.4 TV/c	2.0 TV/c
Helium	10.0 TV/c	10.0 TV/c
Nitrogen	15.1 TV/c	18.0 TV/c
All	2.7 TV/c	3.0 TV/c

Table 3.2: Median magnetic rigidity of simulated Milagrito events.

Figure 3.10 shows the simulated moon shadow shape, with the systematic offset uncorrected and corrected. It can be seen from these plots that the effect of the correction does in fact move the centroid of the moon shadow back to the axis in the declination direction, but does not significantly affect the position of the shadow in right ascension. The projections of the 2-dimensional maps are shown in Figure 3.11. These plots more clearly illustrate the effect that the $\Delta\theta$ systematic bias has on the position of the center of the shadow. Note also that the FWHM of the projections of the shadow decreases by $\sim 10\%$ after the correction. As mentioned in Section 3.2.2, the effect of the correction "tightening" the shadow was expected.

Figure 3.12 shows the contributions to the moon shadow from the different primary cosmic ray species. These projections illustrate the dominance of protons in the moon shadow. This is expected, of course, since protons comprise nearly 70% of Milagrito's triggers. It can also be seen that the offset of the peak position in α of the shadows cast by the heavier species is smaller than the peak-offset of the proton shadow. In fact, the centroid of the full shadow is deflected less than the centroid of the proton shadow, because of the effect of the helium and nitrogen shadows. This means the net deflection of the heavier primary particles detected by Milagrito is less than the deflection of the protons by the geomagnetic field.

Milagrito's sensitivity to the heavier species peaks at a higher magnetic rigidity than it does for protons. The median rigidities of the different nuclear species used in the moon shadow simulation are shown in Table 3.2. Milagrito's effective area, Figure 3.1, falls off more steeply at low energies for heavier species, so the median of the rigidity spectrum is higher for heavier primaries. A helium nucleus of energy 1.0 TeV has a lower magnetic rigidity, R $\sim$ 0.5 TV/c, than does a 1 TeV proton, R $\sim$ 1 TV/c, and so one might naively think that since the deflection of helium nuclei of comparable energy is greater, that the heavier nuclei should increase the net deflection of the moon shadow. But Milagrito's relative insensitivity to the low end of the rigidity spectrum for heavier cosmic rays means that the deflection of the heavy component of the moon shadow is, in fact, smaller than the deflection of the proton shadow.

Figure 3.14 shows projections of the moon shadow events in four different bands of NFit. As mentioned in Section 2.2.2, NFit is expected to be related to the energy of the primary particles. This is demonstrated by the fact that the deflection in α of the center of the moon shadow increases as NFit decreases. This means that the average energy of the events is lower in the lower NFit bands. However, the angular resolution is also a strong function of NFit, and so the effect of the shadow deflection is less significant in the lower NFit bands, as will be shown in Section 4.2.

Figure 3.15 shows how the overall magnitude of the deflection of the peak of the moon shadow depends on energy scale. In this plot the logarithm of the magnitude of the deflected position of the centroid of the simulated moon shadow is plotted versus NFit. The moon shadow was then simulated anew with the overall energy scale of the primary particles increased and then decreased by 50%. The energy change was applied only during the geomagnetic deflection portion of the simulation, so that the NFit distribution and angular resolution of the trigger events is unaffected. Only the deflection of the primary cosmic rays is being tested in this plot. The plot indicates that the magnitude of the offset of the centroid of the moon shadow varies directly with the overall energy scale of the primary particles.

The final step in the moon shadow simulation is to subtract the simulated shadow shape from a background map. This is done to put the simulation in the same form as the data. When done, the result should be simulated "data" maps that can be used in the same analysis routines as the data. The analysis is described in Chapters 4 and 5, and the background estimation method is described in Section 4.2.1.

3.5 Antiproton Shadow Simulation

The effect of antiprotons on the moon shadow was also simulated. The 2-dimensional maps of the shape of the shadow from antiprotons, or "anti-shadow", is shown in Figure 3.16. This figure shows the shape of the shadow as if it were composed entirely of antiprotons. The antiprotons were thrown from the same energy spectrum as the proton events were thrown. The anti-shadow behavior is just as expected: there is a net offset in declination exactly like the net δ offset of the shadow due to the $\Delta\theta$ systematic bias, and there is a net offset in right ascension due to the geomagnetic deflection. But the offset in α is *positive*, rather than negative like the shadow offset is, because antiprotons are positively charged particles and are therefore bent in the opposite direction by the geomagnetic field.

The anti-shadow was added to the simulated moon shadow maps to determine Milagrito's sensitivity to detecting the antiprotons. This is discussed in Chapter 5. Note that the effects of anti-Helium or any anti-nuclear species were not simulated.

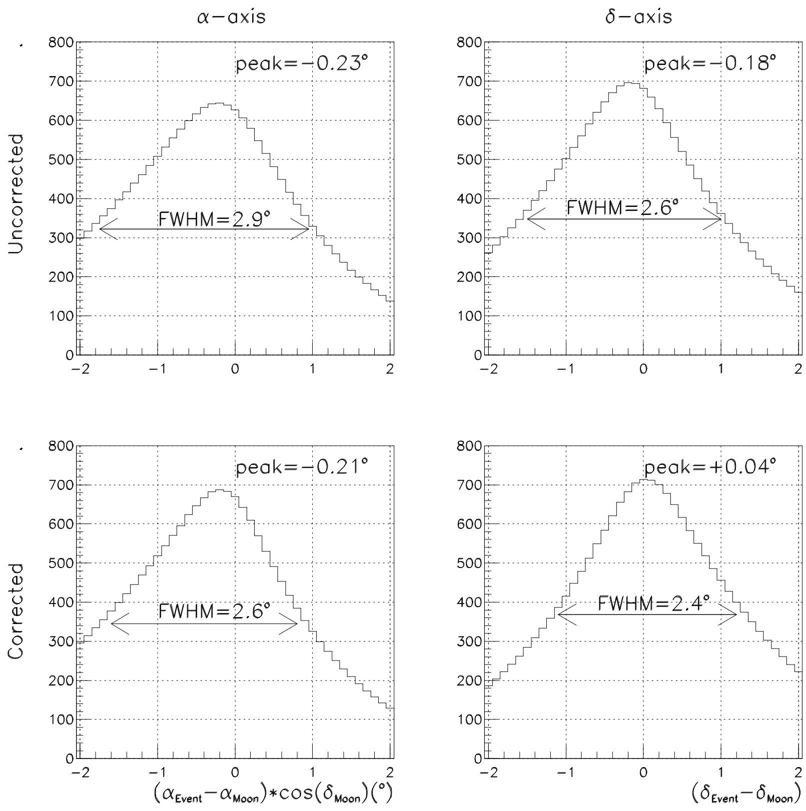

Figure 3.11: Projections of the 2-dimensional maps shown in Figure 3.10. The top plots are the projections of the "uncorrected" moon shadow map, and the bottom plots are the projections of the "corrected" shadow map. The left hand plots are the projections onto the α-axis, and the right hand plots are the projections onto the δ-axis. The effect of the $\Delta\theta$ systematic bias, and its correction, can be seen: the uncorrected plots are $\sim$10% wider than the corrected plots, and the peak of the shadow in the corrected plot is not significantly offset from the center in δ.

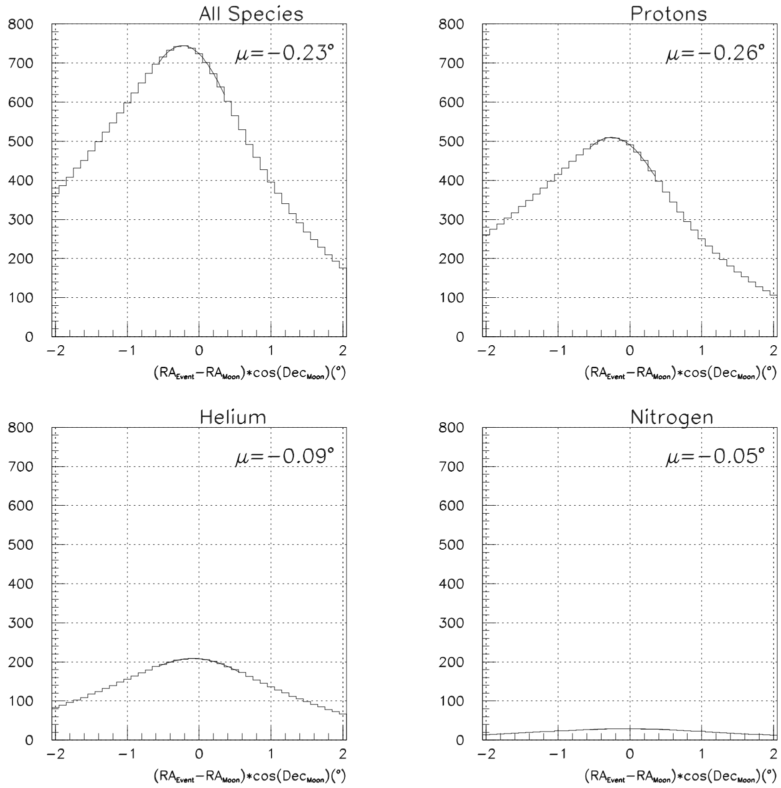

Figure 3.12: Projection onto the α axis of the simulated shape of the moon shadow, shown for each of the simulated species. This is the simulated shape of only those events that are blocked by the moon. The events shown have not been corrected for the $\Delta\theta$ systematic bias.

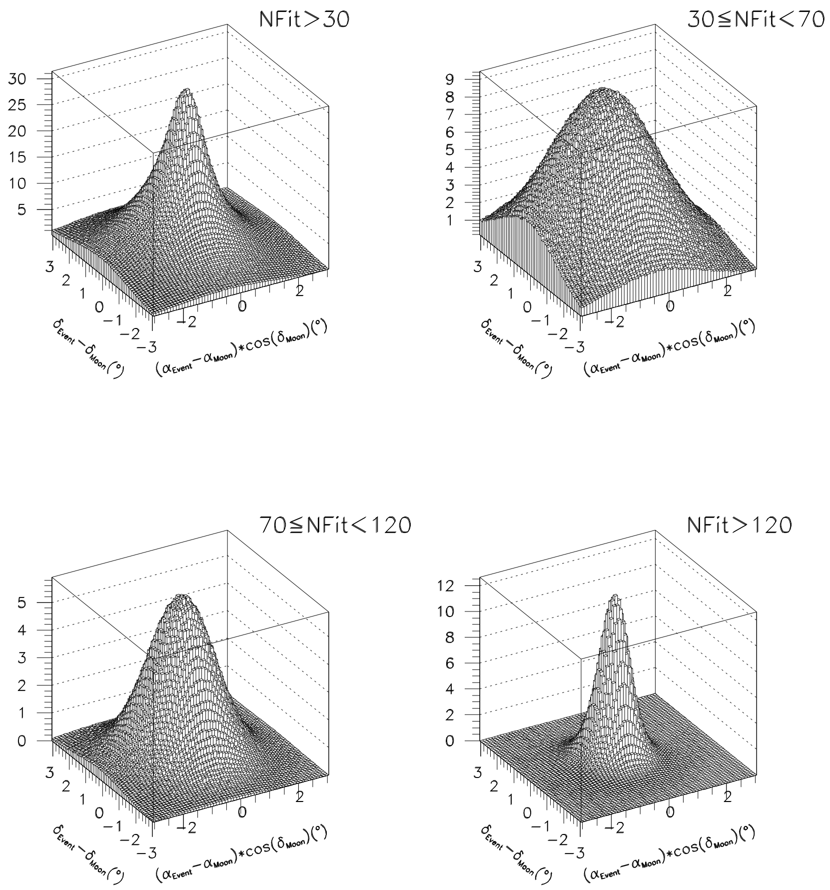

Figure 3.13: Simulated Milagrito moon shadow shape, shown for different NFit bands. This is the simulated shape of only those events that are blocked by the moon. The events shown have been corrected for the $\Delta\theta$ systematic bias.

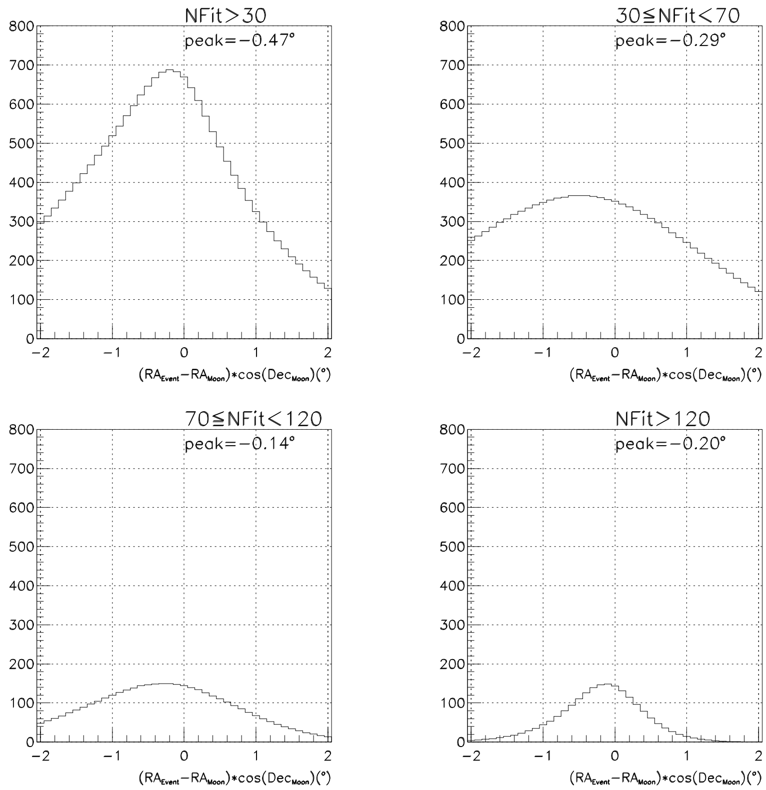

Figure 3.14: Projection onto the α axis of the simulated shape of the moon shadow, shown for each NFit band. The deflection grows greater as NFit decreases. This demonstrates that the average energy of the events in the lower NFit bands is lower than the average energy of the events in the higher NFit bands, as was expected.

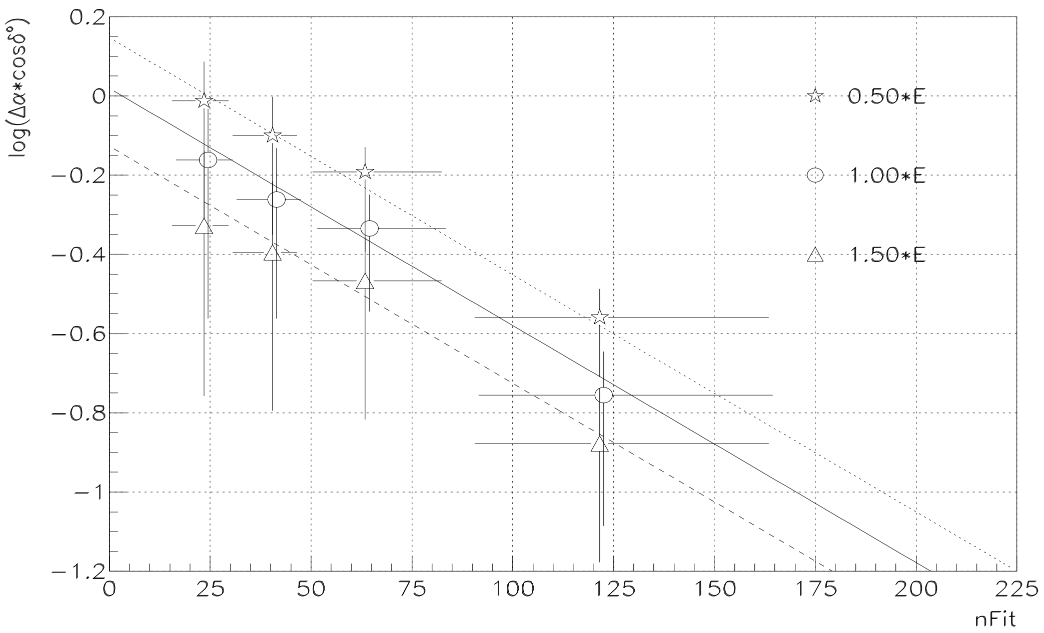

Figure 3.15: Deflection in α of the center of the simulated moon shadow deficit, shown as a function of NFit, for different overall energy scales.

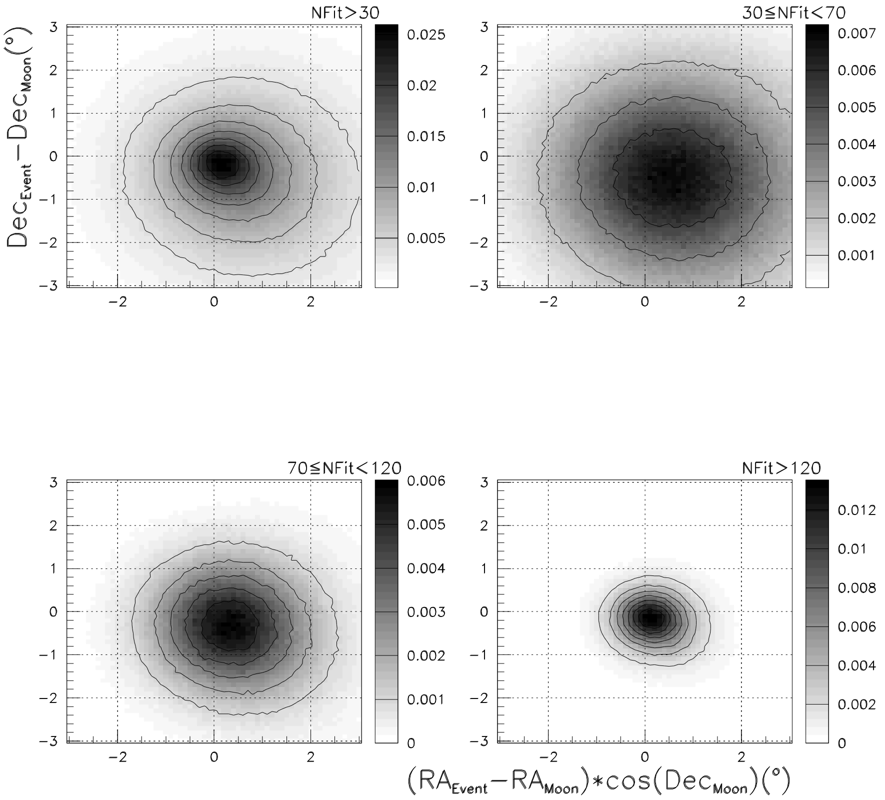

Figure 3.16: Simulated Milagrito moon anti-shadow, meaning the shape of the shadow if it were created by antiprotons, shown for each NFit band. This is the simulated shape of only those events that are blocked by the moon. The grey-scale given on the right of each plot indicated the number of events per $0.1° \times 0.1°$ bin. The events in this plot were not corrected for the $\Delta\theta$ systematic bias.

Chapter 4

Moon Shadow Analysis

Once the data were reconstructed, they were assembled into sky maps. The sky maps were then examined for evidence of a deficit of events from the shadowing of cosmic rays by the moon. This chapter describes the moon shadow analyses.

4.1 Understanding The "Source"

The moon is not like other astronomical objects. Its close proximity to the earth means that it passes through many different points in the sky. A distant object, such as a star or another galaxy, is always located at the same point in the sky, at least over the time scales of human lifetimes. The moon, on the other hand, oscillates through α and δ with a period of 28 days. This adds a slight complication to the analysis, which will be described in more detail in Section 4.2.1. It should also be mentioned that the moon is not a *source* at all, but a *sink*. Unlike all other analyses

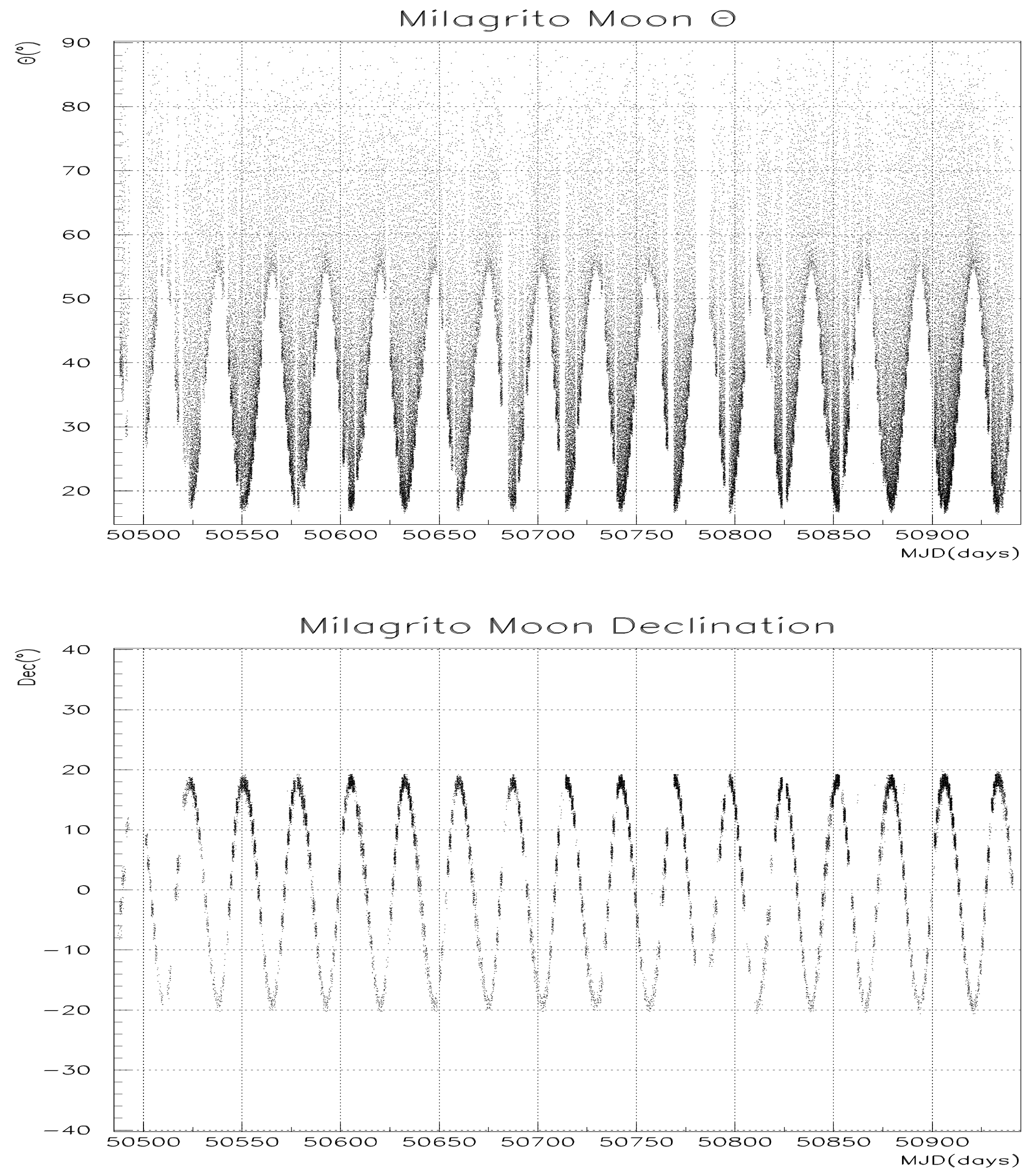

Figure 4.1: Zenith angle and declination of events from within 1° of the moon, shown as a function of modified Julian date, mjd. The maximum zenith angle and the declination of the moon vary sinusoidally with a period of 28 days.

using Milagrito, which look for excesses of events above the background of cosmic rays, the shadow analysis looks for a deficit of events below the background.

Figures 4.1-4.3 show the angular distributions of events from within 1° of the moon's position. Figure 4.1 shows the zenith angle, θ, and declination, δ, of the moon as a function of time. The oscillation of the moon's path can be clearly seen. The plots contains blank spaces, near mjd 50880, for example, when the experiment was down for short periods due to power failures. Figure 4.2 shows the angular distributions in θ, ϕ, δ, and α. The effect of the zenith angle dependence is clearly seen, with the θ and δ plots peaked high in the sky. Compare these plots to the simulated angular distributions, Figure 3.9. Figure 4.3 shows skymaps of the angular distribution of events. The top plot shows the events from the moon in local coordinates, and bottom plot shows the same in equatorial coordinates.

4.2 Signal Analysis

As mentioned above, the data were assembled into sky maps for analysis. The maps were centered on the moon's position, and the events were placed in the map according to their distance from the moon's position in equatorial coordinates. The map consisted of square bins, 0.1° on a side. In order to map equal areas of the sky into the bins no matter what the moon's position was, the axes used for the maps were $\Delta\delta = \delta_{Event} - \delta_{Moon}$ on the ordinate and $\Delta\alpha = (\alpha_{Event} - \alpha_{Moon}) \times \cos(\delta_{Moon})$ on the abscissa.

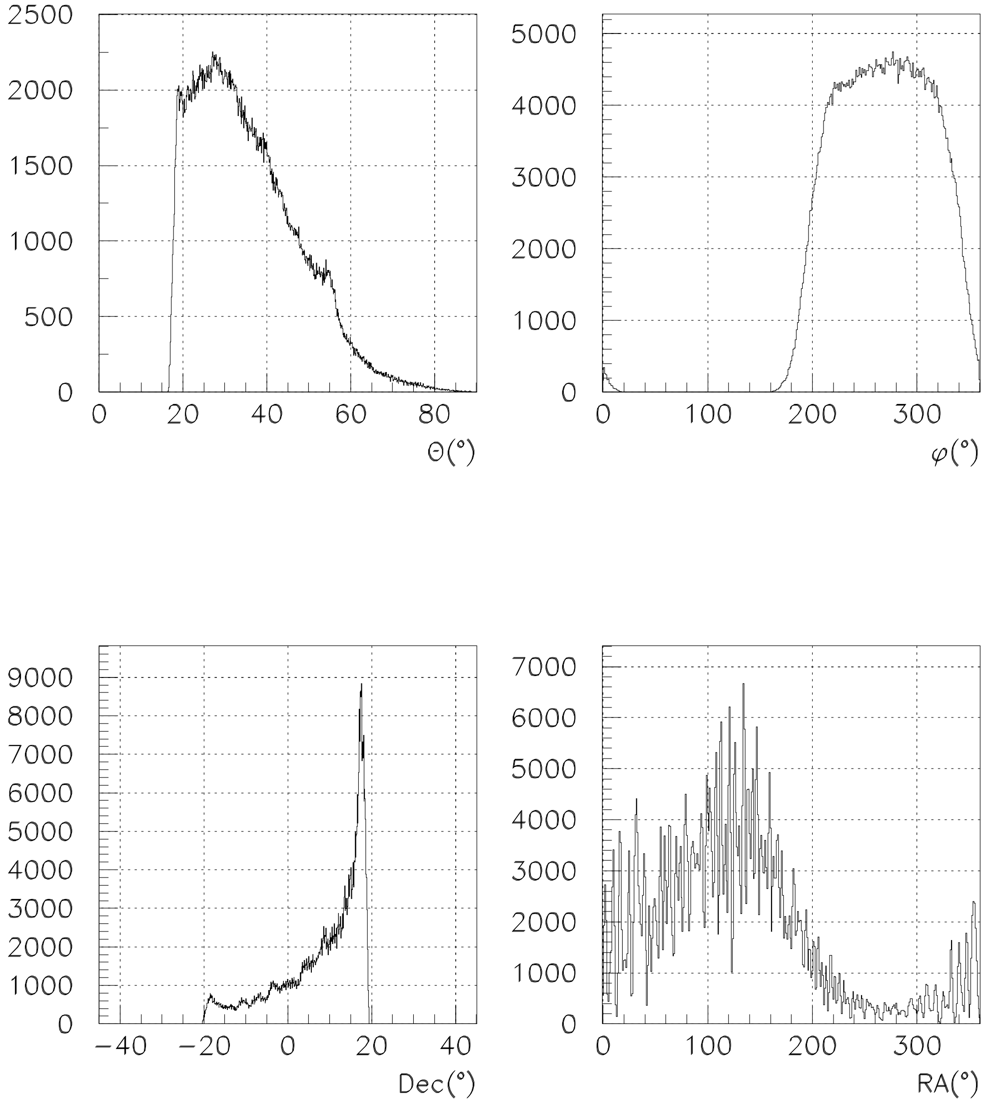

Figure 4.2: Angular distribution of events from within 1° of the moon. The top two plots show the events in zenith angle , θ, and azimuthal angle, ϕ, and the bottom plots show declination, δ, and right ascension, α.

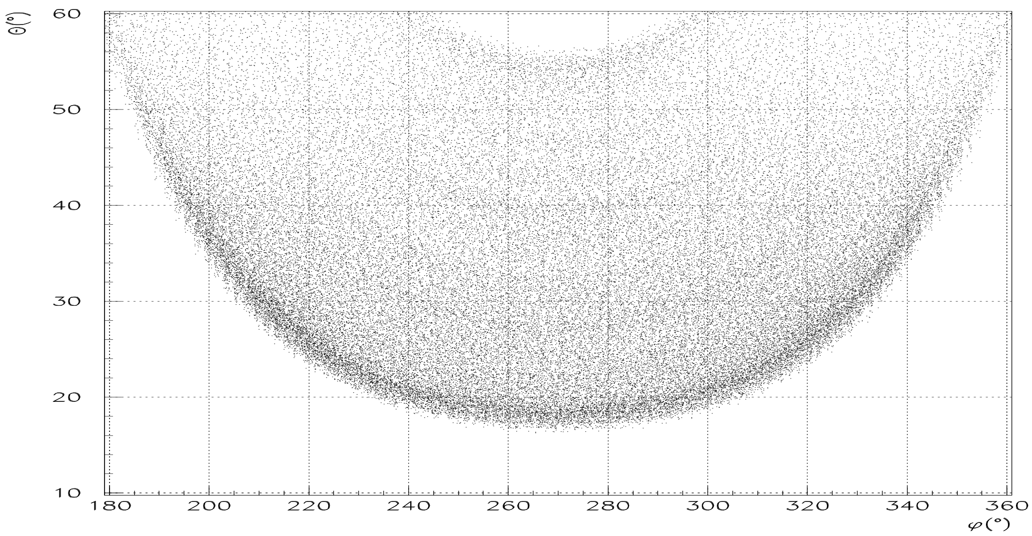

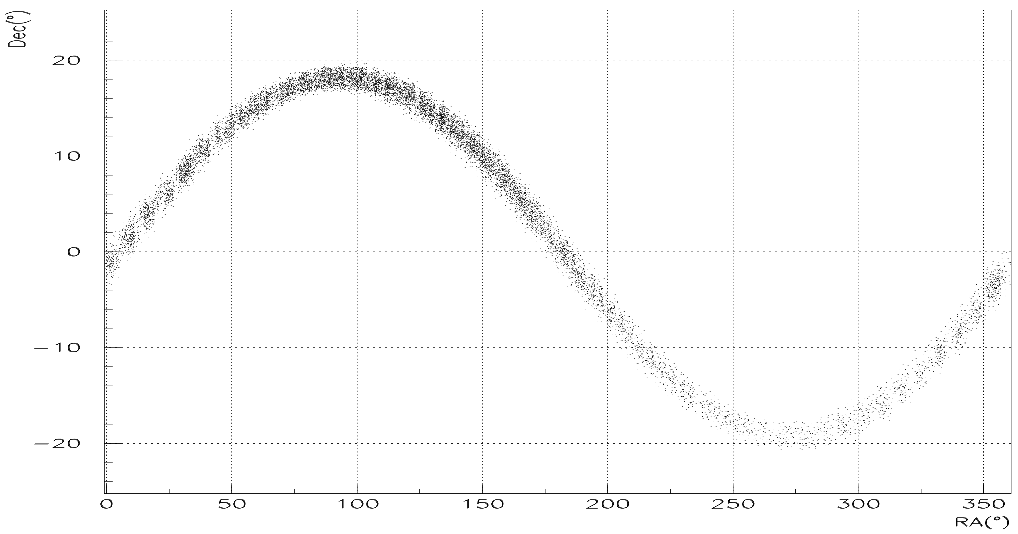

Figure 4.3: Angular distribution of events from within 1° of the moon, shown in θ versus ϕ in the top plot, and δ versus α in the bottom.

Once the background estimate was made (see Section 4.2.1), background maps were assembled in exactly the same way as the data maps. The two maps could then be compared and search techniques applied to look for a deficit in the data maps as compared to the background maps.

4.2.1 Background Estimation

The background estimation method used in this analysis [43] depends upon the fact that the flux of cosmic rays is isotropic. This leads to the assumption that any real detected event in local coordinates could have come at any detected time. All of the events detected in a short time interval (typically two hours) are used to generate a fake data set as follows. The measured local coordinates (θ, ϕ) of each real event are paired with the measured time of another real event chosen randomly from the time interval. This new (t, θ, ϕ) triplet constitutes a new, fake, background event. It is as if the fake event came from the same point in the sky as the first real event, but arrived at the time of the second event. To reduce statistical fluctuations, ten fake events are generated thus for each real event.

Because the effect of this method is to mix up the times of the events in the data sample, it is often called "time sloshing". It is the equivalent of randomly re-assigning a new right ascension to each event, but keeping the declination of the event unchanged. This is because the selection of a new time is equivalent to a rotation of the celestial sphere with respect to the earth. Transforming the original right ascension through the arc equivalent to the time difference between the two events is the same as selecting a new right ascension for the event.

This method naturally takes into account any systematic biases in estimating the background, except for time-dependent biases. Any interruptions in the data collection or other event rate variations, such as those due to extreme weather conditions, are compensated for because the fake data set has the same time distribution as the real one. The fake data set also has the same distribution in local coordinates as the real data have.

The only difficulty in this background calculation is that can lead to an underestimation of the significance of a source (or deficit). This is because it uses the data to assemble the background. In the presence of a true source, the data will have an excess of events due to the signal, and this excess will get added into the background estimate. But a true background estimate should not include any events from the source. This means that the estimated background will be slightly higher than it ought to be, and so the calculated significance will be slightly lower that it ought to be. In the case of a deficit of events, the estimated background level would be slightly lower than it should be due to this effect. Thus the calculated significance of the deficit will also be slightly lower in magnitude than it should be.

If the signal strength is small compared to the event density of the data, however, then the background estimation error is quite small. The effect of the background underestimation in the Milagrito moon data was studied, and found to be negligible.

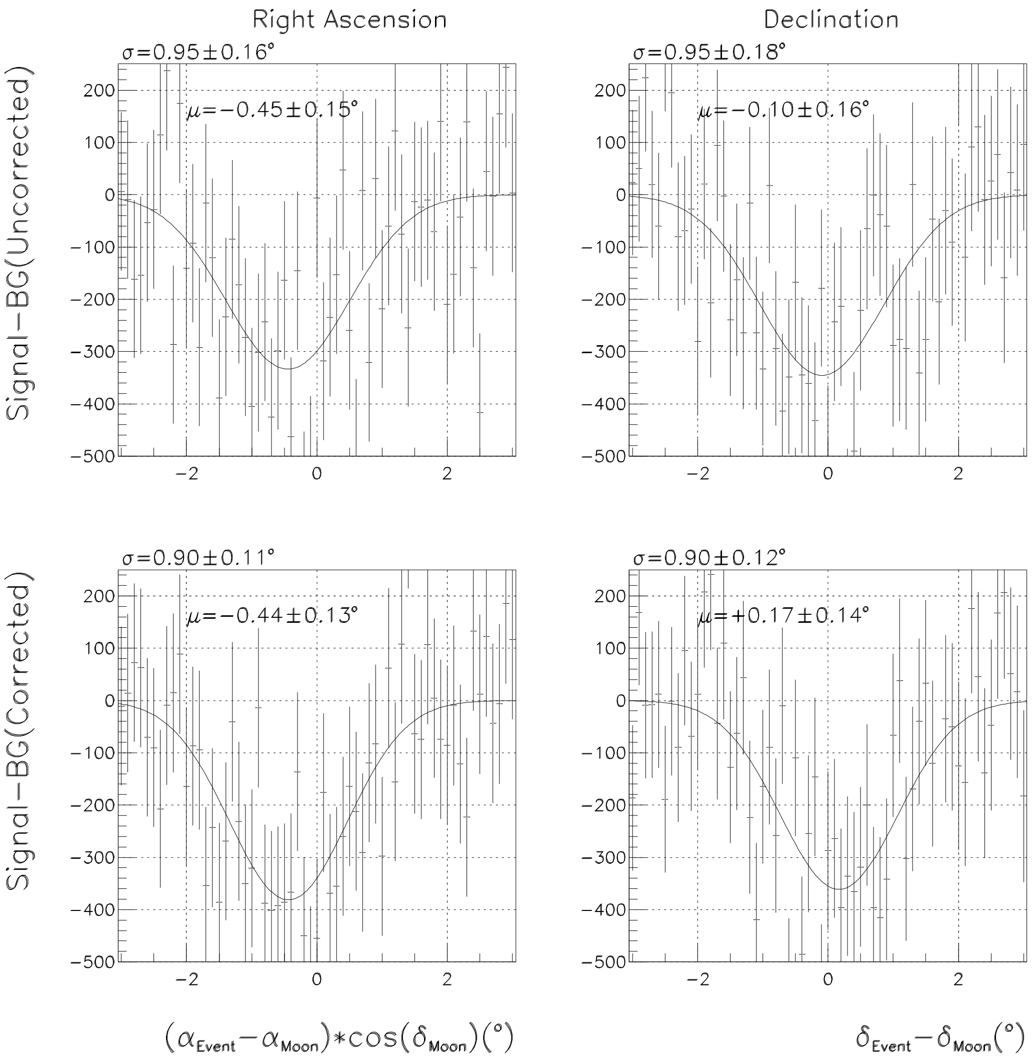

Figure 4.4: Projections of the background subtracted moon shadow data, shown for "uncorrected" and "corrected" data. The moon shadow deficit can be seen in each plot, and is fit to a Gaussian function. The top plots are the projections of the "uncorrected" moon shadow data, and the bottom plots are the projections of the "corrected" data. The left hand plots are the projections onto the α-axis, and the right hand plots are the projections onto the δ-axis.

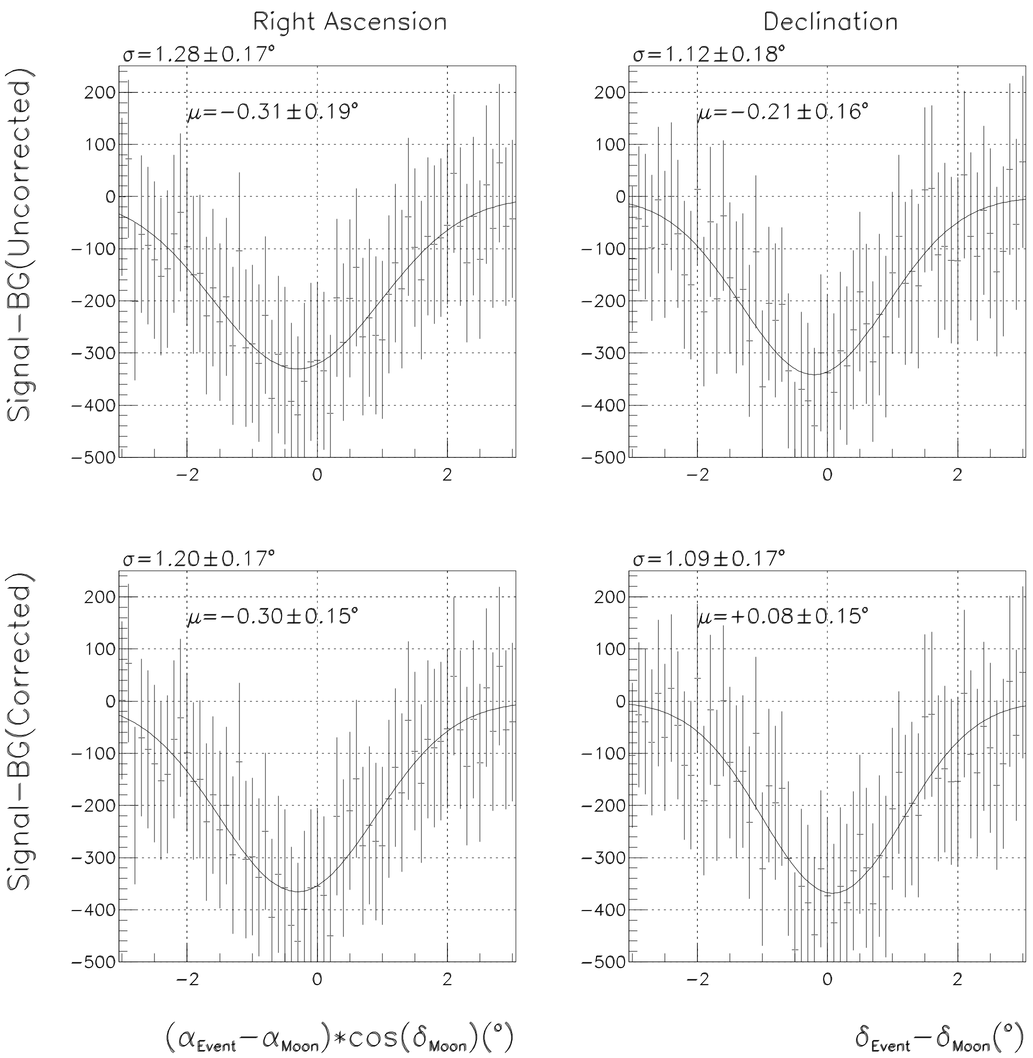

Figure 4.5: Projections of the simulated moon shadow, shown for "uncorrected" and "corrected" data. These plots were made by subtracting the simulated moon shape from an estimated background sample to simulate a "data" set, and then subtracting another background estimate from that simulated sample. See Figure 4.4 and the text for more discussion of the $\Delta\theta$ correction.

The Moon data set spans $\pm 20°$in right ascension, and so a swath $\pm 0.5°$in declination (roughly the extent of the moon's shadow) spread out across the length of the data set in right ascension contains more than five million events. The total deficit due to the moon shadow is approximately 30,000 events, so this deficit is spread out amidst nearly two hundred times that many events by time sloshing. As will be seen in Section 5.1, this effect is smaller than the uncertainty in the size of the deficit, and therefore negligible. Thus the low signal to noise ratio, which usually has a negative impact on an experiment, overcame this flaw in the background estimation method.

4.3 Data Map Projections

The easiest way to look for a deficit once the data and background maps are assembled is to make projections of the maps and simply subtract them. This was done and is shown in Figures 4.4 through 4.6. A band of $\pm 1.0°$in declination, centered about δ_{Moon}, was projected onto the α axis of the data and background maps and the projections were subtracted. The same was done with a projection in a 2.0° band of α projected onto the δ axis. The results were fit with a Gaussian function, with the parameters shown in the plots. The Gaussian gives a measure of the width of the deficit and the position of the peak.

Before looking for signals in the data, it behooves us to remove the known systematic errors from the data. As described in Section 3.2.2, the Milagrito Monte Carlo simulations indicate the presence of a systematic pointing error in θ. The effect was

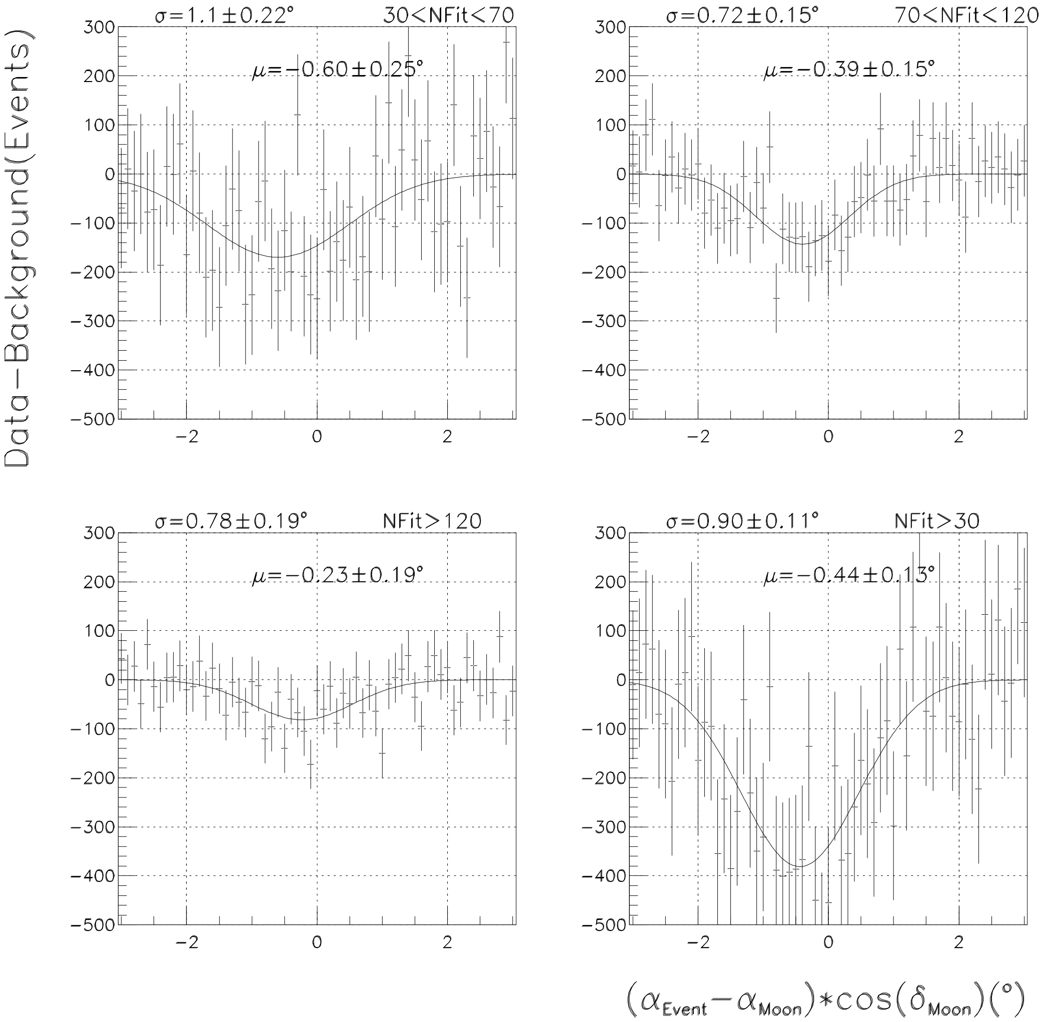

Figure 4.6: Projection onto the RA axis of a 2.0° band in declination of the moon shadow data, shown for for different nFit bands. The moon shadow deficit can be seen, and is fit to a Gaussian function.

parameterized and a corrective method was designed. Figures 3.11 and 3.10 indicate that the correction works for simulated data.

Figure 4.4 shows the projections for the moon shadow data, before and after the correction for the $\Delta\theta$ systematic bias. Each data map was handled in exactly the same way, with separate background maps made for each. The effect of the $\Delta\theta$ systematic bias, and its correction, can be seen: the widths of the best-fit Gaussians in the uncorrected plots are $\sim$ 10% wider than the corrected plots, and the peak of the shadow in the corrected plot has been pushed up in δ by the correction.

Figure 4.5 shows the projections of the simulated moon shadow sky maps. These should be compared to the corresponding plots of the projections of data, Figure 4.4. They are in good agreement, showing that the simulation reflects the moon shadow data accurately. Comparing Figure 4.5 to Figure 3.11 is also enlightening. It shows that the effect of the background on the shadow is to remove some of the features of the shadow shape. Figure 3.11 indicates that the shadow has a large tail on the negative side of the peak in α direction. This is due to the effects of the geomagnetic field. But fitting the background subtracted projection plots with Gaussian functions will not reflect this tail. If this information about the effect of the geomagnetic field is to be utilized, more sensitive techniques must be employed.

4.4 Smoothed Maps

The 2-dimensional sky maps may be analyzed directly. Smoothing the maps is one way to do this. The Milagrito moon shadow maps were smoothed using a square bin 2.1° on a side. This had the effect of drawing out features in the map that occur on scales of 2.1°, such as the moon shadow deficit. The data maps and background maps were smoothed in the same way, and a significance map was made by calculating the significance in each bin. Figure 4.7 shows the result. In this Figure, the significance maps are shown for the data before and after the $\Delta\theta$ correction. The statistical significance of the center of the deficit is 10.2σ. Similar plots for the simulated moon shadow are shown in Figure 4.8.

4.5 Deficit versus Distance Plots

Figure 4.9 shows the deficit of events as a function of distance from the expected center of the moon shadow. In each plot, the expected deficit is obtained by calculating the event density at the moon's nominal position and multiplying that by the apparent solid angle of the moon seen from the earth. Note that it is slightly different for the corrected and uncorrected data, but that the two are consistent. The deficit plots do not indicate an improvement in the width of the moon shadow due to the $\Delta\theta$, however a more significant deficit is found in the corrected data.

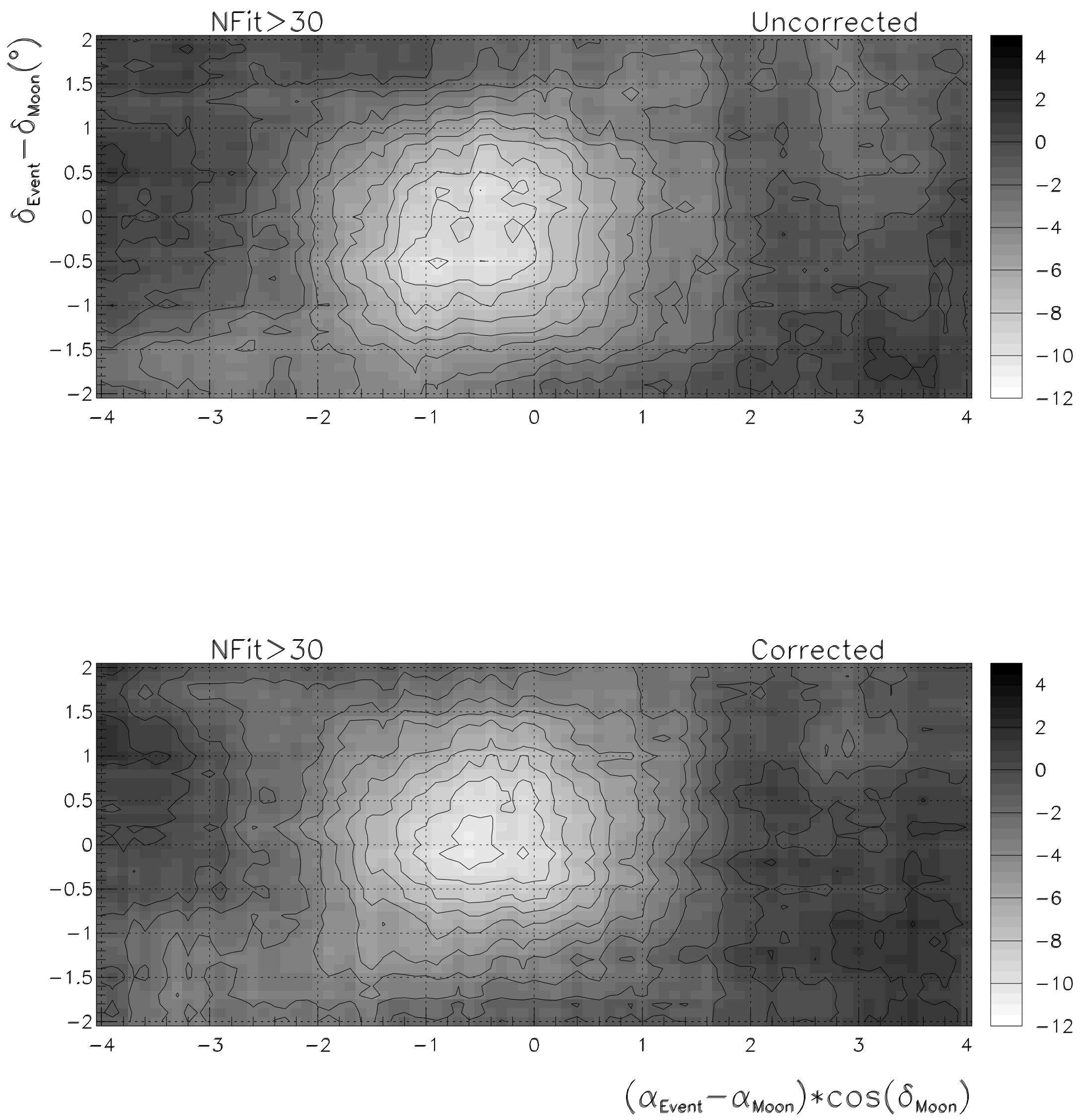

Figure 4.7: Significance of Milagrito moon shadow. Both plots are comprised of data up to $\theta = 45°$. The data were corrected for the $\Delta\theta$ *versus* θ offset, event by event, in the bottom plot. The upper plot is uncorrected. Both plots were smoothed using a square bin 2.1°on a side. The grey-scale given on the right of each plot indicates the significance in each 0.1°×0.1° bin.

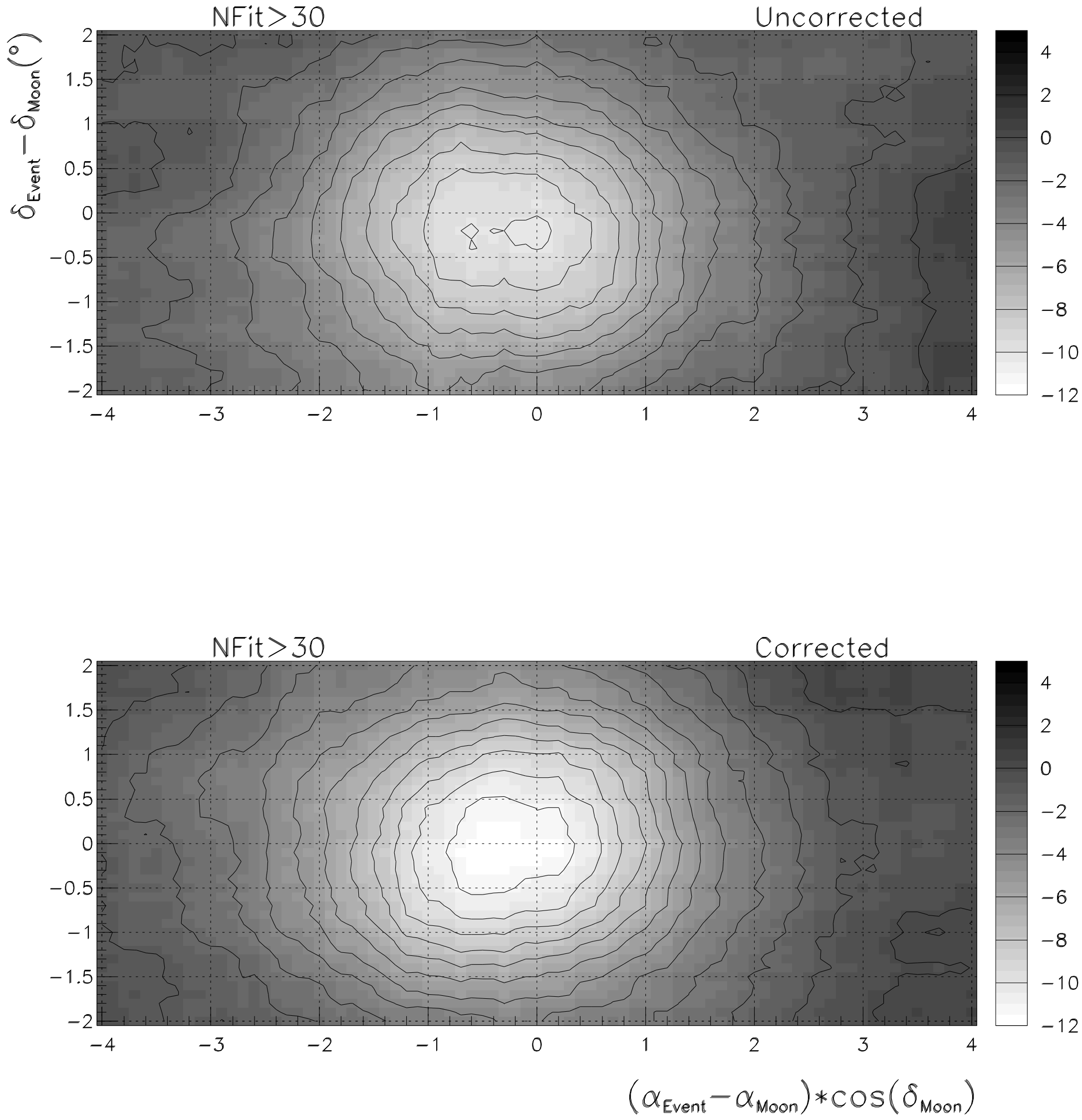

Figure 4.8: Significance of simulated Milagrito moon shadow. Both plots are comprised of simulated events up to $\theta = 45°$. The simulated events were corrected for the $\Delta\theta$ *versus* θ offset, event by event, in the bottom plot. The upper plot is uncorrected. Both plots were smoothed using a square bin 2.1°on a side. The grey-scale given on the right of each plot indicates the significance in each $0.1° \times 0.1°$ bin.

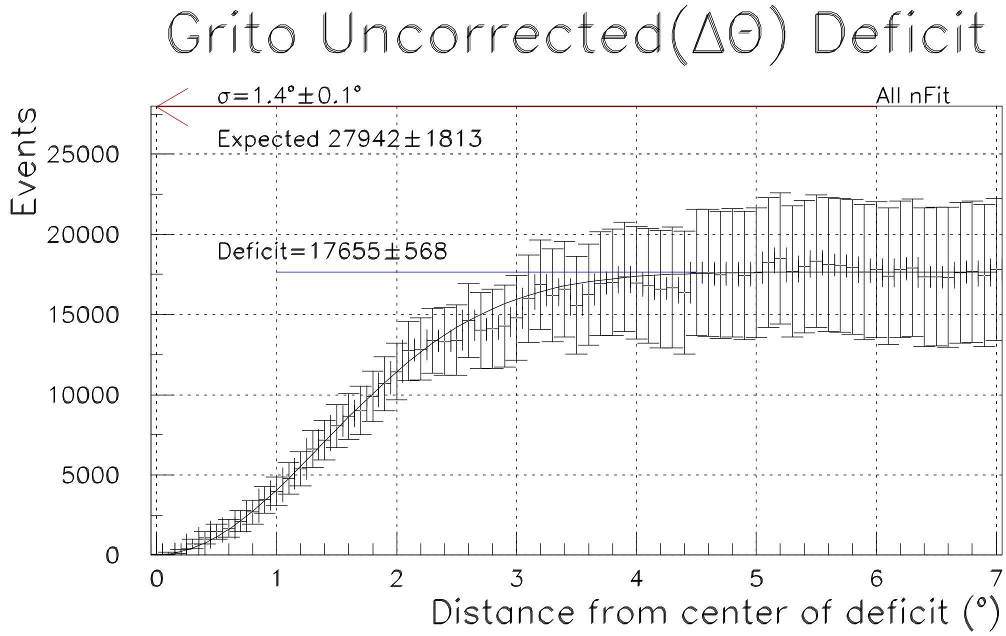

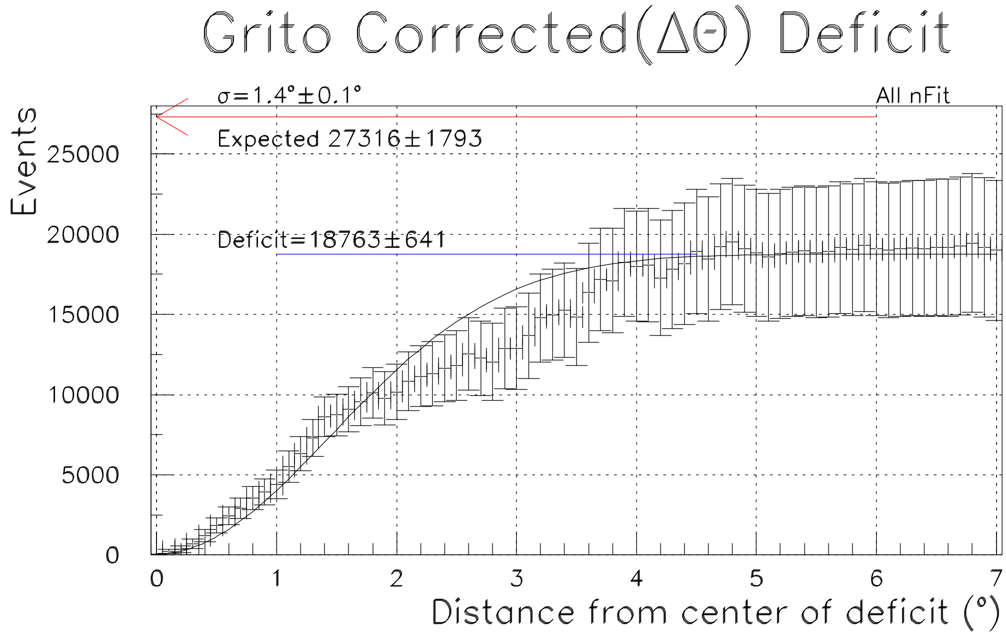

Figure 4.9: Deficit of events measured as a function of the angular distance from the center of the expected position of the shadow of the moon. The $\Delta\theta versus \theta$ corrections lead to a more significant deficit, but not to a noticeable improvement in the width of the deficit.

Width of Milagrito Moon Shadow		
Simulation (Corrected)		
Technique	*NFit Band*	*Width of Shadow*
Width of projection (δ)	30-69	1.67°±0.41°
Width of projection (δ)	70-119	0.98°±0.22°
Width of projection (δ)	120+	0.61°±0.09°
Width of projection (δ)	30+	1.08°±0.17°
Width of projection (α)	30-69	1.89°±0.41°
Width of projection (α)	70-119	1.10°±0.22°
Width of projection (α)	120+	0.56°±0.09°
Width of projection (α)	30+	1.20°±0.17°
Data (Corrected)		
Technique	*NFit Band*	*Width of Shadow*
Width of projection (δ)	30-69	1.09°±0.25°
Width of projection (δ)	70-119	0.65°±0.15°
Width of projection (δ)	120+	0.79°±0.20°
Width of projection (δ)	30+	0.90°±0.13°
Width of projection (α)	30-69	1.09°±0.22°
Width of projection (α)	70-119	0.72°±0.15°
Width of projection (α)	120+	0.78°±0.19°
Width of projection (α)	30+	0.90°±0.11°
Width of Deficit plot	All	1.4°±0.1°

Table 4.1: Width of the Milagrito moon shadow.

4.6 Angular Resolution

The width of the moon shadow has been used in the past as a measure of the average angular resolution of EAS arrays. This is because the moon shadow would appear as a perfectly round hole in the sky map if the detector had perfect angular resolution, and deviations from this ideal case are very easy to detect.

The width of the data map projections, or the width of the deficit plot, can be used as a measure width of the moon shadow as seen by Milagrito. These numbers

α offset of Milagrito Moon Shadow		
Technique	*NFit range*	*α offset*
Simulation	30-69	-0.49°±0.41°
Simulation	70-119	-0.21°±0.23°
Simulation	120+	-0.19°±0.08°
Simulation	30+	-0.30°±0.15°
Data	30-69	-0.60°±0.25°
Data	70-119	-0.39°±0.15°
Data	120+	-0.23°±0.19°
Data	30+	-0.44°±0.13°

Table 4.2: Position in α of the center of the Milagrito moon shadow.

are summarized in Table 4.1. The widths of the projections onto the α and δ axes are all listed, because they are affected in different ways by the magnetic field and the systematic bias. As mentioned already, the systematic bias causes a net offset in the moon shadow's position only in the δ direction. But the $\Delta\theta$ systematic effect does affect the widths in both the α and δ directions. The geomagnetic field, on the other hand, causes a net deflection only in the α direction, but affects the width of the shadow in both directions.

While it is an oversimplification to assign a single number to a complex quantity like the angular resolution, it can be a useful way to characterize the overall performance of an experiment. For that purpose, the overall angular resolution indicated by the projection plots for all events with NFit greater than 30 is 0.9°.

4.7 Effect of Geomagnetic Deflection

As described in Section 3.4, the α position of the centroid of the moon shadow is expected to vary with the energy of the detected events. It should be possible then to get some measure of the absolute energy scale of the detector by studying the position of the moon shadow.

Table 4.2 shows the position of the center of the deficit of the Milagrito moon shadow projection plots; the position is given by the means of the Gaussian functions used to fit the deficit. Values for the simulation and data are shown. The position of the center of the shadow is clearly a function of NFit; this NFit dependence is seen in both the data and the simulation. The data and simulation are consistent with each other, though they do not agree exactly.

Figure 4.10 shows the effect of a change in the energy scale on the position of the center of the moon shadow, and Milagrito's ability to detect it. Plotted in the figure are the means of the Gaussian functions from the fits to the data and simulation projections. Additional values from the simulation are plotted, with the overall energy scale of the events in the simulation varied. The same energy change was used for Figure 3.15, but that plot showed the position of the peak of the moon shadow shape itself varied with energy, while Figure 4.10 includes the effects of the background and its subtraction.

This plot requires additional explanation. Along the abscissa is plotted the overall energy scale. In the center is +0%, which means the energy scale was not modified

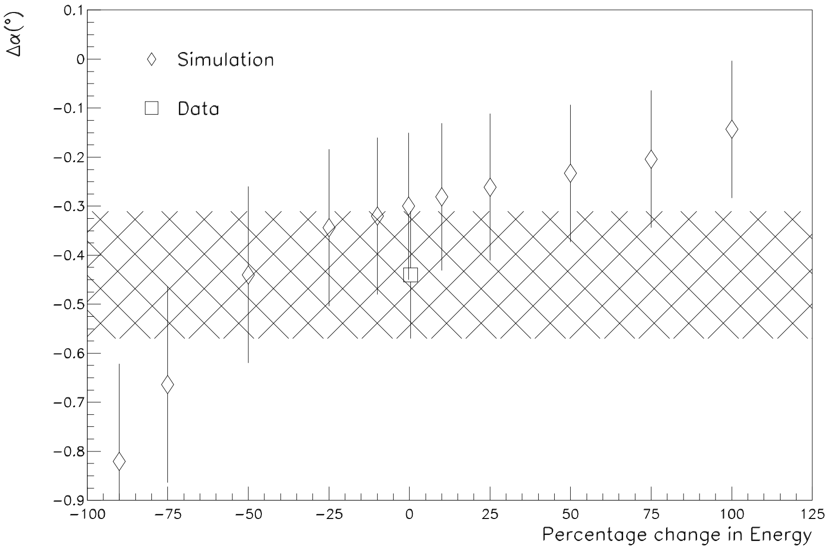

Figure 4.10: The α offset of the moon shadow. Plotted here are the values for the data and simulation, and additional points indicating the $\log \alpha$ offset for different overall energy scales. Refer to the discussion in the text.

at all; the simulation value plotted here is the full value discussed previously. At +50%, the energy of each simulated event was increased by 50% for the geomagnetic deflection calculation. The energy was not altered for the other portions of the simulation, however, so that the other properties of the events, such as the NFit and DELEO distributions, are the same as those for the +0% entry. The -50% entry had the energy of each event decreased by 50%, and so on. Note that the error bars for the points below 0% grow as the energy scale decreases, but they do not decrease above 0% as the energy scale increases. This is because the the detector effects, such as angular resolution and systematic offsets, were not changed by the variation in energy scale during the geomagnetic deflection portion of the simulation. Above 0%, the error bars are due only to these effects, but below 0%, the error bars are increased by the effects of the geomagnetic field.

The plot can be used to gauge the overall energy scale of Milagrito's triggered events. The cross-hatched area shows the 1σ region of the position of the moon shadow's center as measured from the data. The energy scales where the 1σ regions of the simulated shadow positions no longer overlap with the cross-hatched region can be declared inconsistent with the data. This gives the region of consistency for the overall energy scale of Milagrito. The region of consistency is large, as can be seen in the figure, indicating that Milagrito's ability to measure the absolute energy scale is poor. Figure 4.10 indicates that the overall energy scale of Milagrito is known within $\pm 85\%$. This topic is discussed again in Section 5.4.

Chapter 5

Maximum Likelihood Analysis of Moon Shadow

The traditional moon shadow analysis methods, described in Chapter 4, are not sensitive to the possible presence of two shadows in close proximity to each other within the data. In this case, "close proximity" means closer than half the smoothing size. The search for antimatter within the cosmic ray flux requires the ability to distinguish two shadows, since antimatter would appear as a second shadow deflected in the opposite direction along the right ascension, α, axis.

As discussed in Section 4.3, the moon data set is mapped onto a 2-dimensional region. The moon shadow appears as a deficit of events below the expected background cosmic rays, with the shape described in Section 3.4. Antiprotons in the cosmic ray flux would appear as an additional deficit, shaped like that shown in Figure 3.16,

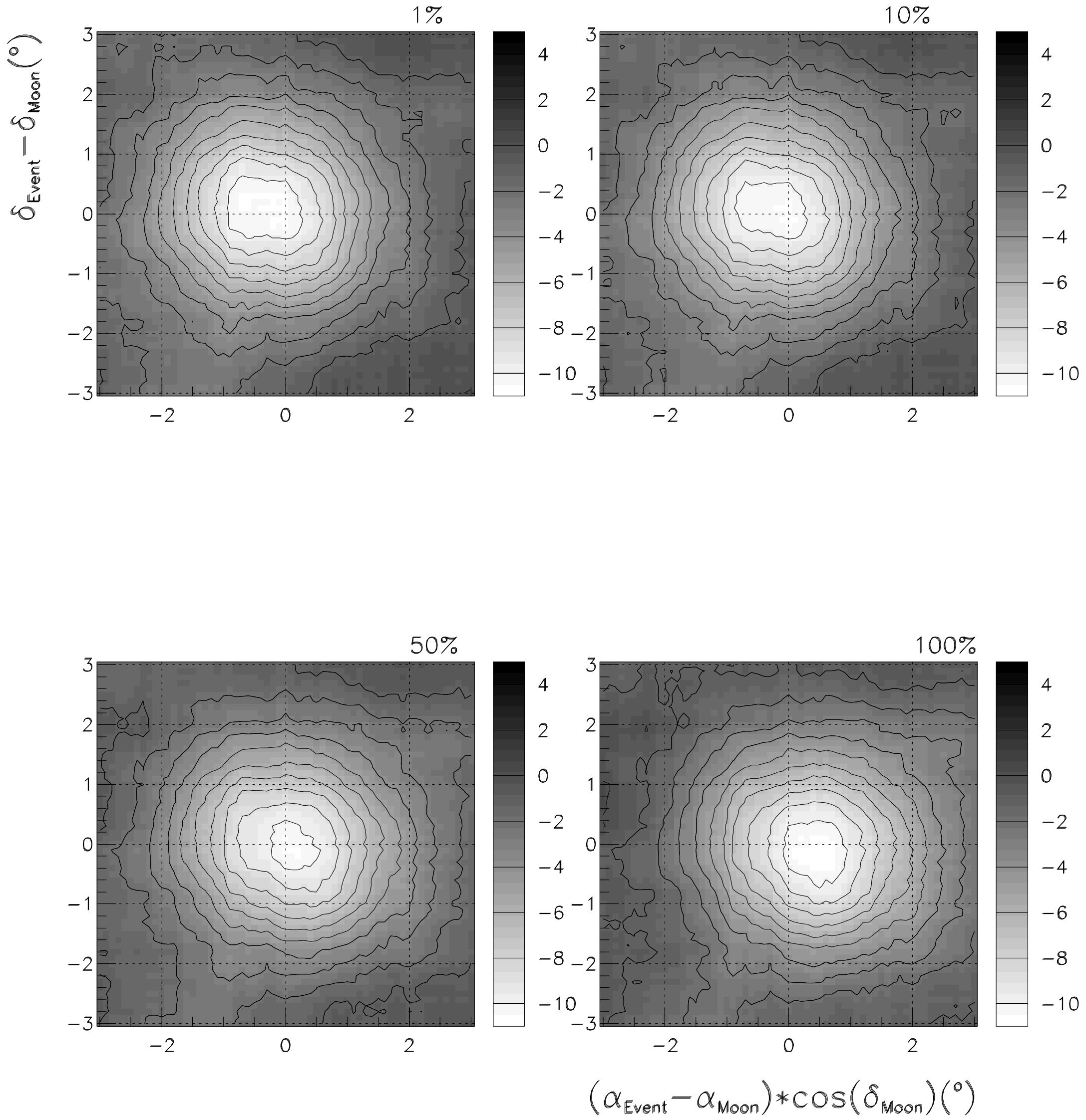

Figure 5.1: Simulated moon shadow significance shown as a function of NFit, with an anti shadow at various levels. The total number of events in the shadows, moon shadow plus moon anti-shadow, is held constant. Thus the number of events in the moon shadow in the 10% plot is 90% of the shadow in Figure 3.16, with the anti-shadow comprising the other 10% of the events. The 100% plot has no cosmic ray events in the shadow, just $\overline{p}$ events. The grey-scale shown to the right of each plot gives the significance in each $0.1^{\circ} \times 0.1^{\circ}$ bin.

within the moon data map. Figure 5.1 shows the simulated moon shadow with an antiproton shadow, or anti-shadow, added. The figure shows the smoothed significance maps of the shadow plus anti-shadow, with four levels of anti-shadow shown: 1%, 10%, 50% and 100%.

In the simulated skymaps that were used to make the plots in Figure 5.1, the fraction of events comprised of antiprotons was subtracted from the total number of shadow events, and the remaining fraction was comprised of the usual cosmic rays: 68% protons, 28% helium, and 4% nitrogen. Recall that the true size of the deficit due to the shadow of the moon is equal to the product of the event density and the apparent solid angle of the moon. Thus, if some significant fraction of the cosmic ray flux were actually comprised of antiprotons, then that fraction would form the anti-shadow, and the shadow deficit would be reduced by that amount.

Figure 5.2 shows the projections of a 2.0° band of declination onto the α axis made from the plots in Figure 5.1. Together, the anti-shadow figures clearly demonstrate how difficult it is to distinguish the presence of the anti-shadow. It is, in fact, not clear at all from these plots that there is a second shadow. The plots look just as they would if the position of the moon shadow itself were simply shifted and widened.

If the angular resolution of the detector were much better and the offset along the α axis were greater, it might be possible to distinguish two shadows within the data. Or if the mix of matter and antimatter were close to 50-50, then one might hope to distinguish two separate shadows with the methods outlined in Chapter 4. Figure 5.2

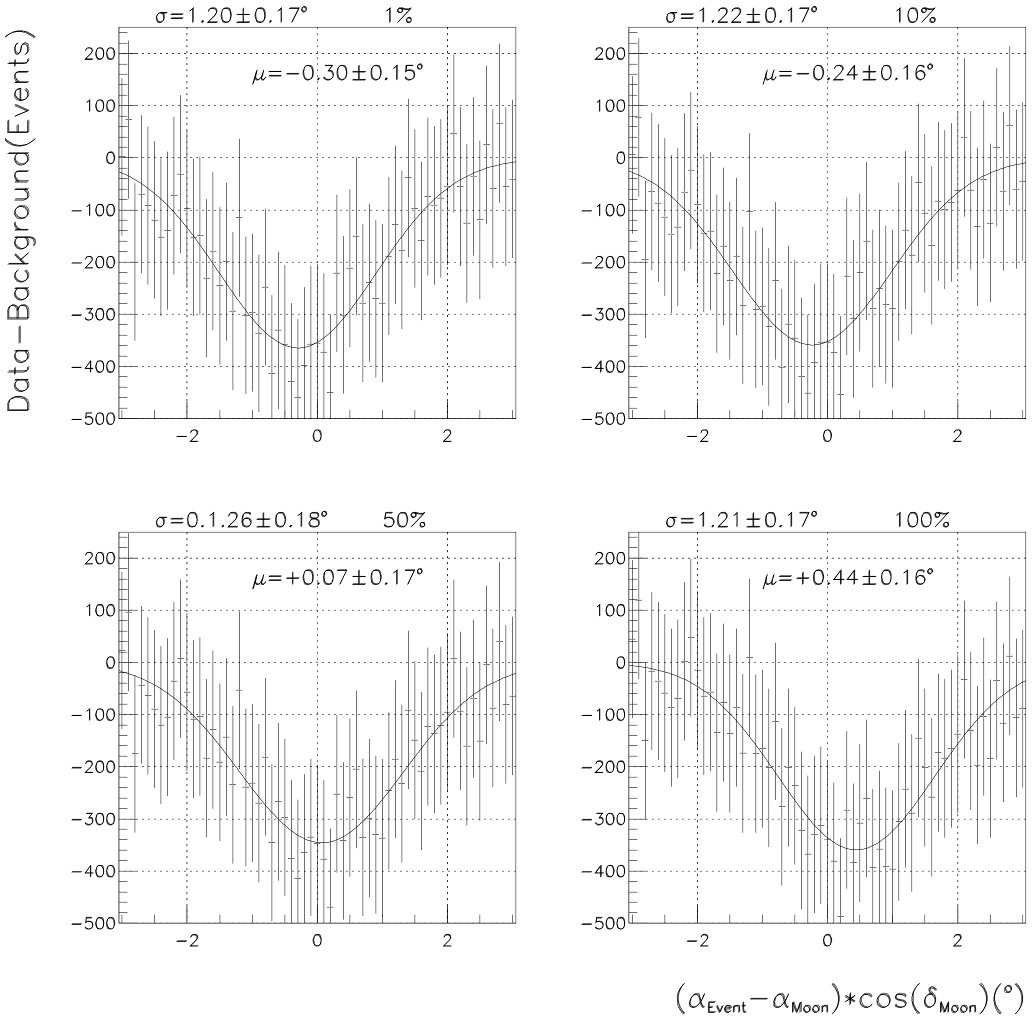

Figure 5.2: Projections of Figure 5.1 onto the α-axis. The deficit is fit to a Gaussian function, with the widths and means shown. The center of the shadow can be seen to move along the α-axis as more events are taken from the shadow and put into the anti-shadow. Note that the magnitude of the offset of the 100% plot is greater than the magnitude of the offset of the moon shadow plot, since the anti-shadow is comprised entirely of antiprotons, with no other species added. (See Sections 3.5,3.4.)

indicates that the width of the deficit is slightly greater in the 50-50 case than in the 10% case. But attributing the increased width to the presence of a second shadow would require much greater accuracy in the measurement of the widths; the indicated increase in width is significantly less than than the uncertainty in the measurement of the width.

Clearly, more powerful methods are needed. The task of searching for evidence of $\overline{p}$sconsists of searching for the different shadow shapes within the data. The method described below is a maximum likelihood approach to finding the shadow shapes within the data maps. The method is first used to study the moon shadow alone, then applied to the search for antiprotons.

5.1 Outline of Maximum Likelihood Technique

This section describes the mathematics of the maximum likelihood method used. The technique is adapted from [45]. General discussions of maximum likelihood methods are found in [46, 47]. The first use of the method is an analysis of the moon shadow alone, searching for one deficit due to the shadowing of cosmic rays.

Let each event be represented by a vector: $\vec{x_i} = (\alpha_i, \delta_i)$, and assume that there are two populations of events, background and signal. Let $Q(\vec{x_i})$ be the normalized probability distribution of the signal events, and $R(\vec{x_i})$ be the normalized probability distribution of the background events. Out of the total sample of N events, let n of them be signal, and (N-n) be background. Then the partial probability density of the

ith event is given by:

$$P(\vec{x_i}) = \frac{n}{N} Q(\vec{x_i}) + \frac{N-n}{N} R(\vec{x_i}), \tag{5.1}$$

with the requirement that

$$\sum_{i=1}^{N} P(\vec{x_i}) = 1. \tag{5.2}$$

The likelihood function is then given by:

$$\mathcal{L}(n, \vec{x_i}) \equiv \prod_{i=1}^{N} P(\vec{x_i}) = \prod_{i=1}^{N} \left\{ \frac{n}{N} Q(\vec{x_i}) + \frac{N-n}{N} R(\vec{x_i}) \right\}. \tag{5.3}$$

The likelihood function on its own is not particularly useful for quantifying the results of the analysis. The *likelihood ratio* function is therefore used. The likelihood ratio yields the relative probability of two hypotheses. In this case, the hypotheses are:

> *Hypothesis 1* There are two populations: background and signal, defined by the distributions $Q(\vec{x_i})$ and $R(\vec{x_i})$.
> *Hypothesis 2* Null Hypothesis: there is no deficit. (n = 0)

The likelihood ratio function is given by,

$$\mathcal{R}(n, \vec{x_i}) = \frac{\mathcal{L}(n, \vec{x_i})}{\mathcal{L}(0, \vec{x_i})} = \prod_{i=1}^{N} \left\{ \frac{n}{N} \left(\frac{Q}{R} - 1 \right) + 1 \right\}, \tag{5.4}$$

where $\mathcal{L}(0, \vec{x_i})$ is the likelihood function for the null hypothesis. For a deficit search, the number of events in the deficit, n, is expected to be negative.

For ease in calculations, the logarithm of the likelihood ratio function is calculated, rather than the likelihood ratio itself.

This method is well suited to a binned analysis. The probability functions for the two event populations can be calculated for each bin and kept in an array. The

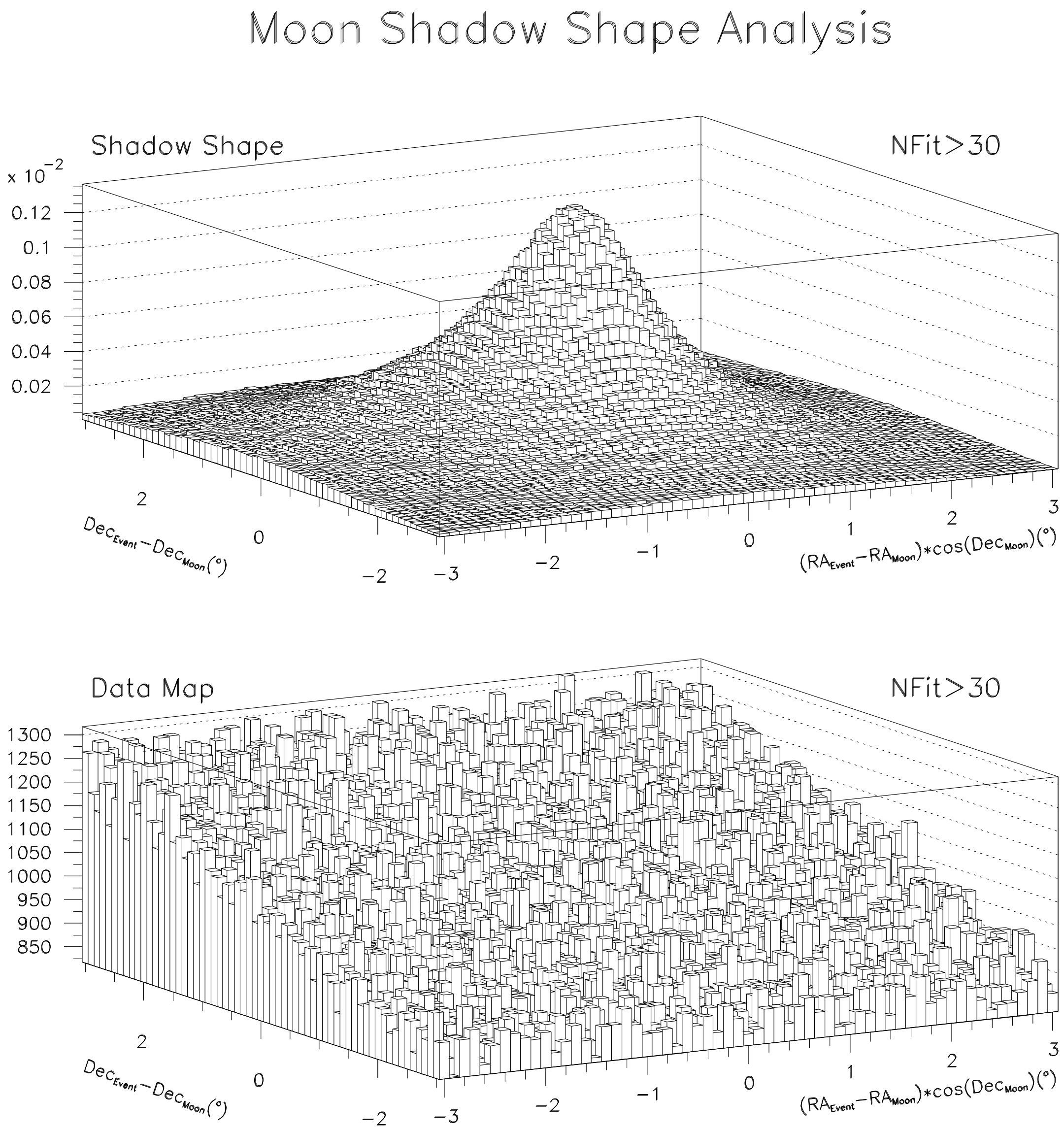

Figure 5.3: Conceptual diagram of how the maximum likelihood shape analysis works. The data map is scanned for the presence of the shadow shape.

events are mapped onto a binned area as usual, and it is assumed that a bin centered at $(\alpha_j,\ \delta_j)$ with n_j events in it is the same as n_j events located exactly at $(\alpha_j,\ \delta_j)$. If the bins are made finely enough, the error introduced by this can be made smaller than other errors in the experiment.

The analysis was performed using the $\Delta\theta$-corrected data and simulated events. The probability function for the signal population is taken directly from the $\Delta\theta$-corrected simulation, and normalized to unity over the area of the map. Specifically, the shadow shape shown in the bottom plot of Figure 3.10 is normalized and used to give the discrete values of $Q(\vec{x_i})$ in each bin. The probability function for the background population is found by simply normalizing the estimated background skymaps and using the values in each bin as the discrete values of $R(\vec{x_i})$.

Figure 5.3 illustrates the idea behind the likelihood shadow search method. The bottom plot in the figure is a portion of the data map shown in coordinates of $\Delta\delta$ versus $\Delta\alpha$. The nominal position of the center of the moon is (0,0); Section 4.2 describes how the skymaps were assembled. Contained within is the actual moon shadow deficit, but it is not evident to the naked eye. The top plot in the figure shows a portion of the simulated moon shadow shape, normalized to unity. The likelihood search calculates the probability that the data contains a deficit of that shape below the estimated background (not shown in the figure) rather than just the background itself. The method gives the relative probability between the two hypotheses; it answers the question "how much more likely is it that the data contain a deficit of given overall number of events and shape centered at the given location, rather than no deficit at all?"

The maximum likelihood ratio function is expected to be normally distributed, hence the log of the likelihood function should be parabolic. This introduces an easy error estimation method. The equivalent of a 1σ region in any of the function parameters is given by the interval over which the value of the log of the likelihood ratio function drops by 0.5 [47]. Note that the *value* of $\log \mathcal{R}$ drops by 0.5 over the 1σ interval, it is not a reduction by a factor of one half.

The parameter $2 \cdot \log \mathcal{R}$ is expected to be distributed like a χ^2 distribution, with the correct number of degrees of freedom. In the present moon shadow analysis, there are three degrees of freedom. This is used to calculate the statistical significance of the results.

5.2 Maximum Likelihood Search for the Moon Shadow

Figure 5.4 shows the result of the maximum likelihood search for the moon shadow. The top plot shows the significance as a function of α and δ. Each point in the plot is assigned the maximum significance below background of the entire shadow, with the centroid located at that point. Compare this plot to Figure 4.7, which shows the significance of the smoothed data maps. In Figure 4.7, each point is correlated with all the neighboring points within the smoothing bin. Thus it represents the statistical significance of the deficit of events in a $2.1^\circ \times 2.1^\circ$ region. In Figure 5.4, each point

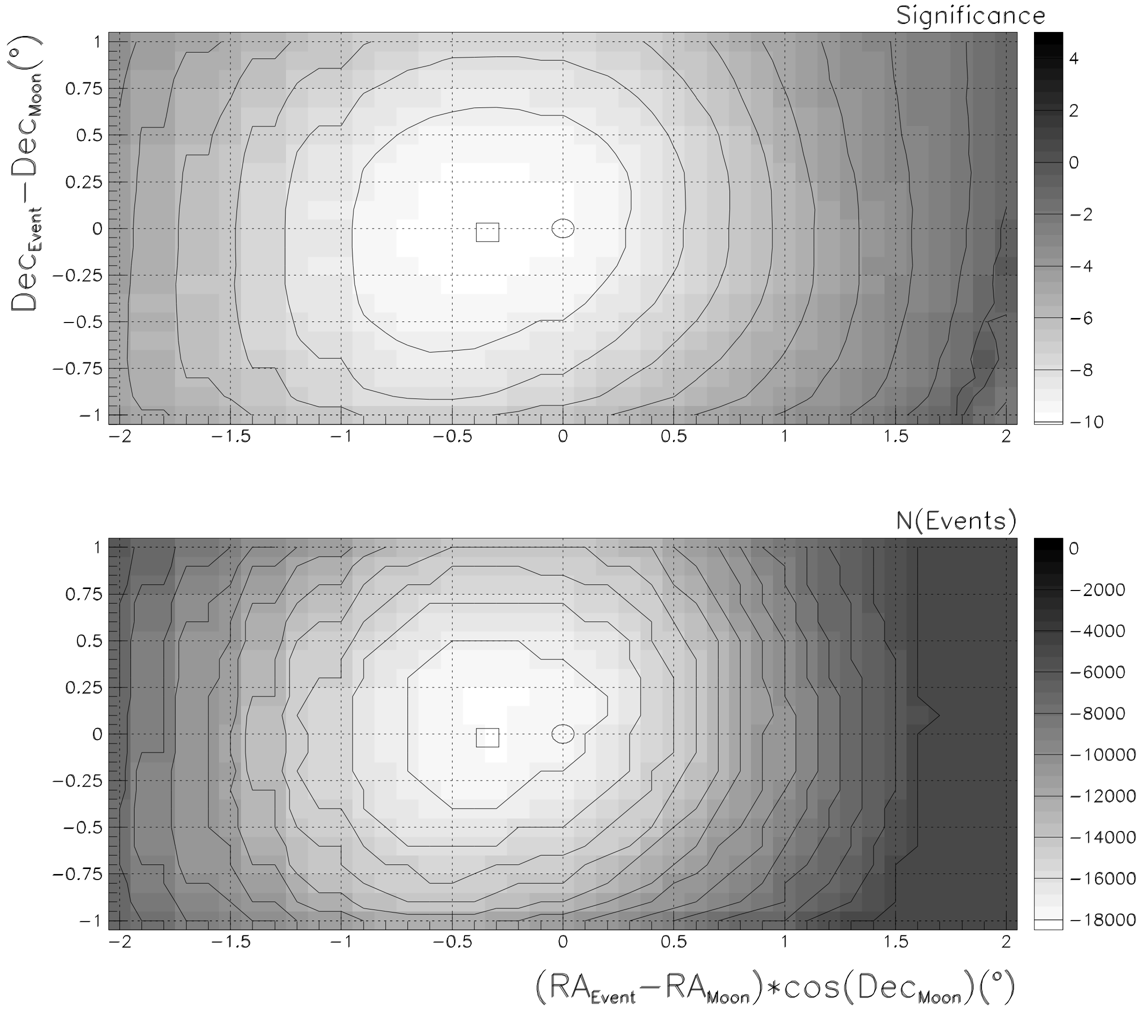

Figure 5.4: Results of the moon shadow shape analysis found using the maximum likelihood method, shown as a function of the position of the center of the deficit, for the Milagrito moon shadow data. The top plot shows significance, the bottom plot shows the number of events in the deficit. The square in each plot shows the position of the maximum value of $\log \mathcal{R}$, and the circle shows the nominal (undeflected) position of the moon. The events used to make each plot were $\Delta\theta$-corrected.

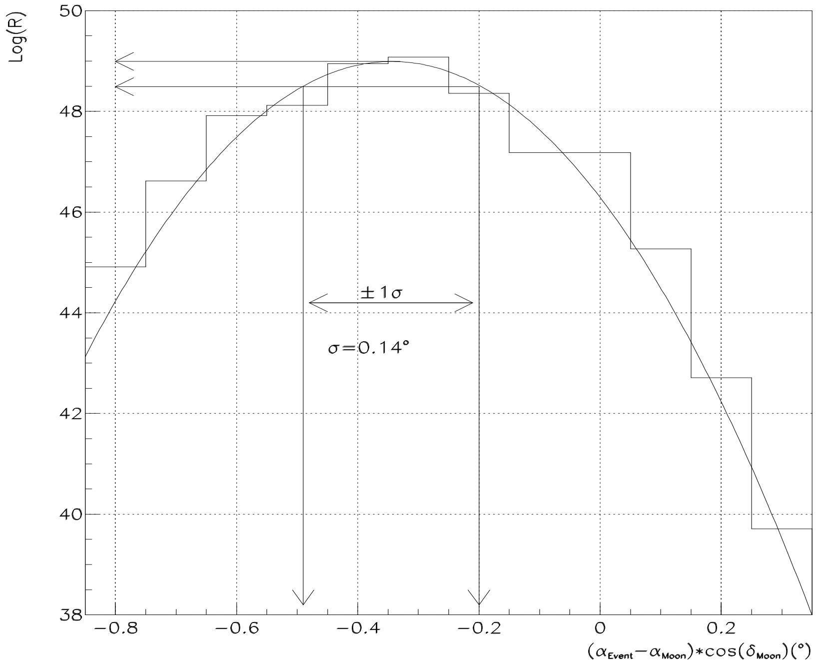

Figure 5.5: Behavior of $\log \mathcal{R}(\alpha)$ near the maximum, taken from the maximum likelihood analysis of the data. This is a projection of $\log \mathcal{R}(n, \vec{x_i})$ onto the α axis. The histogram was fit to a parabola, which is shown. The interval over which $\log \mathcal{R}$ drops by 0.5 is the 1σ region, thus the most likely position of the center of the shadow of the moon on the α axis is $-0.34 \pm 0.14°$.

represents the significance the deficit with the specified shape and number of events over the entire map.

The bottom plot in Figure 5.4 shows the number of events in the deficit as a function of α and δ. The value at any point in the bottom plot is the number of events in the deficit that maximizes the significance if the shadow were centered at that point.

Figure 5.5 shows the projection of $\log \mathcal{R}(n, \vec{x_i})$ onto the α axis. The plot illustrates how uncertainties in the measurements are found using the value of the logarithm of

Maximum Likelihood Moon Shadow Results				
Input	*NFit range*	α *offset*	δ *offset*	*Deficit*
Simulation	30-69	-0.47°±0.36°	+0.17°±0.35°	-15516 ± 2791
Simulation	70-119	-0.30°±0.30°	+0.04°±0.27°	-4792 ± 918
Simulation	120+	-0.25°±0.15°	+0.04°±0.11°	-2232 ± 260
Simulation	30+	-0.25°±0.13°	-0.09°±0.12°	-22132 ± 2090
Data	30-69	-0.55°±0.33°	+0.48°±0.33°	-10693 ± 1999
Data	70-119	-0.46°±0.19°	-0.03°±0.12°	-4366 ± 651
Data	120+	-0.54°±0.19°	-0.14°±0.15°	-1277 ± 207
Data	30+	-0.34°±0.14°	-0.02°±0.15°	-17834 ± 1785

Table 5.1: Position of and number of events in the Milagrito moon shadow, from the maximum likelihood technique.

the likelihood function. The interval over which the value of $\log \mathcal{R}$ drops by one half is the 1σ region. In the figure, $\log \mathcal{R}$ peaks at -0.34°, with a value of 49.1; the points in α at which the value of $\log \mathcal{R}$ is equal to 48.6 define the boundaries of the 1σ region of uncertainty for the measurement. This occurs at -0.48° and -0.20°; the region of uncertainty is 0.28° wide, thus the uncertainty (σ) is 0.14°. Because $\log \mathcal{R}$ is parabolic near the maximum, the uncertainty is symmetric.

The results of the maximum likelihood moon shadow analysis are summarized in Table 5.1. The uncertainties on the position of the deficit center are not significantly better than the uncertainties from the methods used in Chapter 4. The significance of the shadow is 9.9σ, very close to the significance found in Chapter 4 as well.

Figure 5.6 compares the significance maps of the data and simulation. This figure illustrates the power of the maximum likelihood search, but also highlights a weakness of the simulated moon shadow. In the figure, the significance of the simulated shadow is much higher than the significance of the data shadow. Comparing Figure 5.6 to Figure 4.7 shows that the significance of the simulated shadow found with the maximum likelihood method is $\sim 2\sigma$ higher than the significance of the simulated shadow found by smoothing the simulated skymaps. In both cases, the maximum likelihood calculation of the simulated moon shadow significance yields a more significant result. This is because the maximum likelihood technique uses for the assumed probability distribution the exact shape of the simulated shadow. This also means that the shape of the simulated shadow probably does *not* exactly match the shape of the true moon shadow. If it did, the significance of the data shadow would be comparable to the significance of the simulated shadow, since the assumed probability distribution would then match the deficit shape in both cases. The fact that the significance of each shadow is comparable in the smoothed skymaps indicates that the overall deficits of the two shadows are most likely comparable, but the shape of the true shadow probably does not exactly match the simulated shadows shape.

This can also explain why the number of events in the deficit is smaller in the data than in the Monte Carlo. Table 5.1 gives the number of events in the deficit for each NFit band in the simulated and data moon shadows. The maximum likelihood search performed on the simulated shadow recovers the correct number of events, but the number of events found in the data shadow is significantly smaller than expected. If the shape of the true shadow is significantly different than the shape of the simulated shadow, i.e., if one shadow shape had significantly larger tails than the other shadow shape, then the maximum likelihood technique would not maximize for the correct

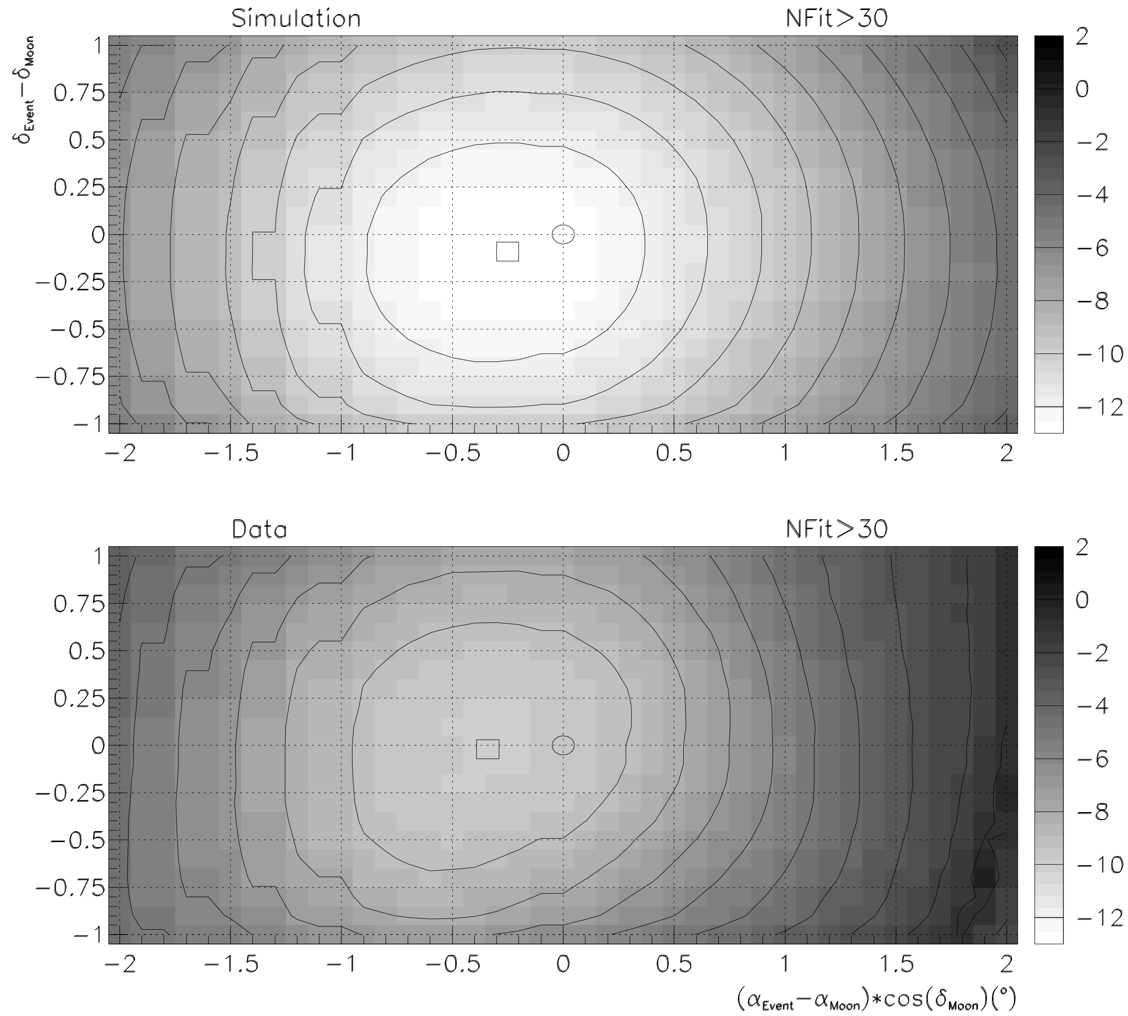

Figure 5.6: Results of the moon shadow shape analysis found using the maximum likelihood method, shown as a function of the position of the center of the deficit. These plots show the significance of the data and the simulation. The events used to make each plot were $\Delta\theta$ corrected. The square in each plot shows the position of the maximum value of $\log\mathcal{R}$, and the circle shows the nominal (undeflected) position of the moon. Using the maximum likelihood method, the significance of the simulated moon shadow deficit is 12.9σ and the significance of the Milgarito moon shadow 9.9σ below background.

number of events in the deficit. Note that either shadow could have the long tails and this would be true.

5.3 Absolute Pointing Ability of Milagrito

Table 5.1 gives the location of the centers of the deficit from the data and the simulation. The difference between the two locations is $0.09 \pm 0.19^\circ$ in α, $0.07 \pm 0.19^\circ$ in δ, and $0.11^\circ \pm 0.20^\circ$ in both dimensions. Assuming that the simulation correctly predicts the true location of the center of the deficit, the difference between the simulated deficit center and the observed deficit center indicates the overall absolute pointing error of Milagrito. In truth, the absolute pointing ability is probably better than this comparison would indicate, because the simulated shadow shape differs from the true shadow shape, as discussed in Section 5.2; the difference between the two deficit center locations could stem from the differences between data and simulation.

5.4 Energy Scale Measurement

The method described in Section 4.7 is employed to measure the overall energy scale of the detector, but the the positions of the shadows, for both simulation and data, now come from the maximum likelihood analysis. Figure 5.7 shows the results. Again, it is clear that the overall energy scale of Milagrito cannot be measured with great accuracy using the position of the moon shadow. By extrapolating the values

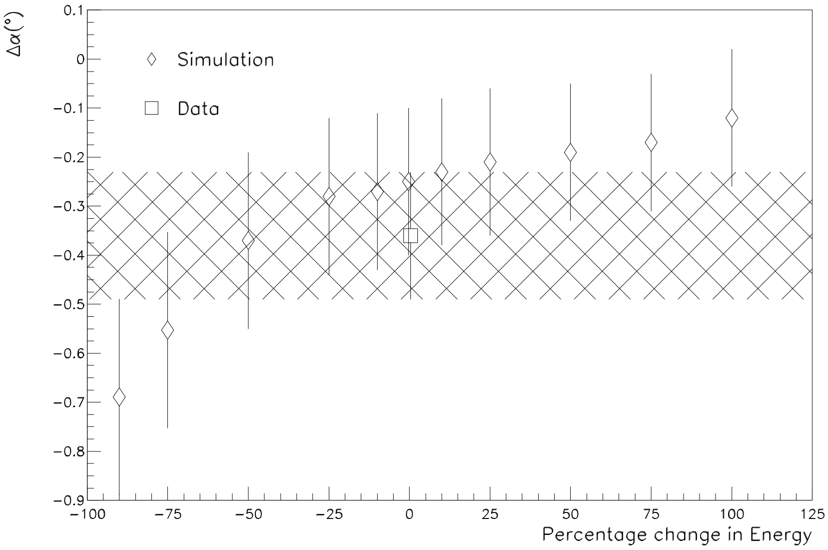

Figure 5.7: The α offset of the moon shadow, found using the maximum likelihood method. Plotted here are the values for the data and simulation, and additional points indicating the α offset for different overall energy scales. Refer to the discussion in the text.

shown in Figure 5.7, it can be concluded that the overall energy scale cannot be decreased by less than 90% of the nominal value or increased by more than ~110% of the nominal value and remain consistent with observations.

5.5 Antiproton Search

The search for the presence of antimatter in the cosmic ray flux can be incorporated naturally into the analysis with the maximum likelihood technique. As described at the beginning of this chapter, the presence of antimatter would create a second shadow alongside the moon shadow. To search for another shadow, an additional probability distribution, $Q_2(\vec{x_i})$, is added to the likelihood function,

$$\mathcal{L}(n_1, n_2, \vec{x_i}) \equiv \prod_{i=1}^{N} P(\vec{x_i}) = \prod_{i=1}^{N} \left\{ \frac{n_1}{N} Q_1(\vec{x_i}) + \frac{n_2}{N} Q_2(\vec{x_i}) + \frac{N - n_1 - n_2}{N} R(\vec{x_i}) \right\}, \quad (5.5)$$

where n_1 and n_2 are the number of events in the two shadow populations. Then the analysis proceeds as before. In the $\overline{p}$ search, $Q_1(\vec{x_i})$ represents the probability density of the moon shadow, which has n_1 events, and $Q_2(\vec{x_i})$ represents the probability density of the anti-shadow, which has n_2 events. If there is a component of antimatter in the cosmic ray flux, then both n_1 and n_2 would be negative.

The position of the anti-shadow with respect to the shadow was constrained for the $\overline{p}$ search. As described in Section 3.4, there is no expected offset in declination of the position of the center of the shadow after the $\Delta\theta$ correction is applied to the data. This should be true for an anti-shadow as well, because the systematic bias and its correction depend only upon the detector itself. It is only the offset in the right ascension position of the center of the shadow that is expected to change, because the direction of the deflection depends on the charge of the particles responsible for the shadow. So, the position of the anti-shadow is constrained to have the same position as the shadow in δ, but is reflected across the axis in α. The α position of the anti-shadow is not expected to be exactly opposite to the shadow's however, since the the anti-shadow is assumed to be comprised solely of antiprotons, with no anti-nuclei present. Based on the relative offsets of the proton-only shadow and the full shadow, the α position of the antiproton-only shadow was constrained to be $-1.2 \times \alpha_{shadow}$.

The results of the $\overline{p}$ search are shown in Figure 5.8. This figure plots the log

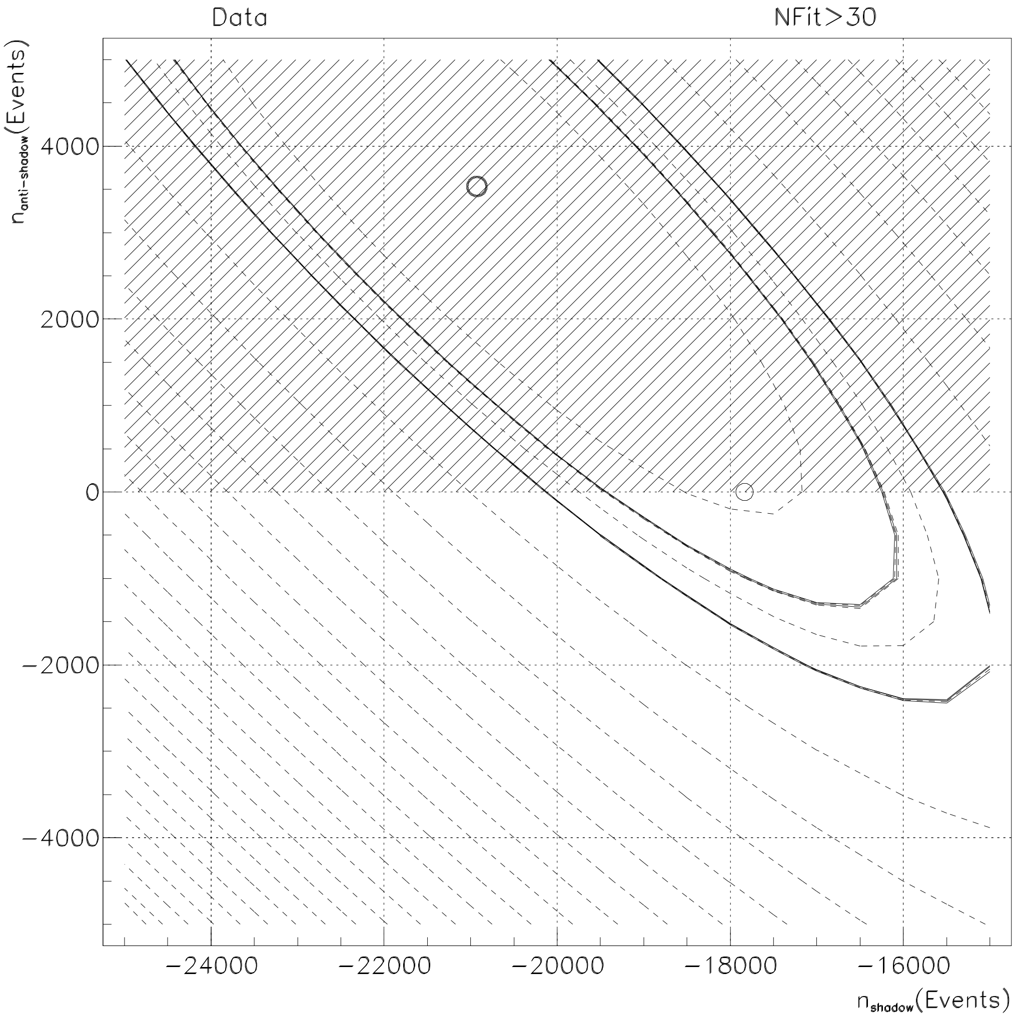

Figure 5.8: *Results of the $\overline{p}$ search.* Shown here are the contours of the logarithm of the likelihood ratio function for the Milagrito moon shadow $\overline{p}$ search, shown as a function of the number of events in the moon shadow deficit and the number of events in the moon anti-shadow deficit. In this plot, the non-physical region ($n_{anti-shadow} > 0$) is indicated by cross-hatching. The dark circle at (-20900, +3550) is the global maximum of the likelihood function, and the lighter circle at (-17830,0) is the maximum in the physical region. The solid lines show the 95% confidence level contours, based on the locations of the maxima mentioned above. The dashed lines show the σ contours.

of the likelihood ratio as a function of n_{shadow}, the number of events in the moon shadow deficit, and $n_{anti-shadow}$, the number of events in the anti-shadow deficit. For comparison with Equation 5.5, $n_{shadow} = n_1$, and $n_{anti-shadow} = n_2$. The dotted line contours are multiples of σ.

As can be seen in the plot, the maximum of the log of the likelihood ratio occurs in a non-physical region, i.e. an excess rather than a deficit of events for the anti-shadow. There are no sources of cosmic rays between the earth and the moon, so it is unreasonable to expect that $n_{anti-shadow}$ is positive. The shape of the contour lines in the plot can offer some explanation. The contours are highly eccentric ellipses, with the semi-major axes aligned on a diagonal of slope ~ -1. This indicates that taking a small number of events out of the shadow and putting them into the anti-shadow, or vice-versa, results in very similar values of $\log \mathcal{L}(n_1, n_2, \vec{x_i})$, i.e., the likelihood function requires conservation of events. It also indicates the limit of the sensitivity of this technique to finding two separate nearby shadow shapes within the data.

The inner of the two solid contours drawn in the plot is the 95% confidence interval based on the maximum value of the log of the likelihood ratio. In other words, the presence of two shadows being found in the parameter space outside this region can be excluded with 95% confidence.

If the maximum in the physical region is used, a new 95% confidence level contour can be drawn. This is also shown in Figure 5.8; the 95% C.L. contour for the physical region is the outer of the two solid contour ellipses. The 95% C.L. contour extends

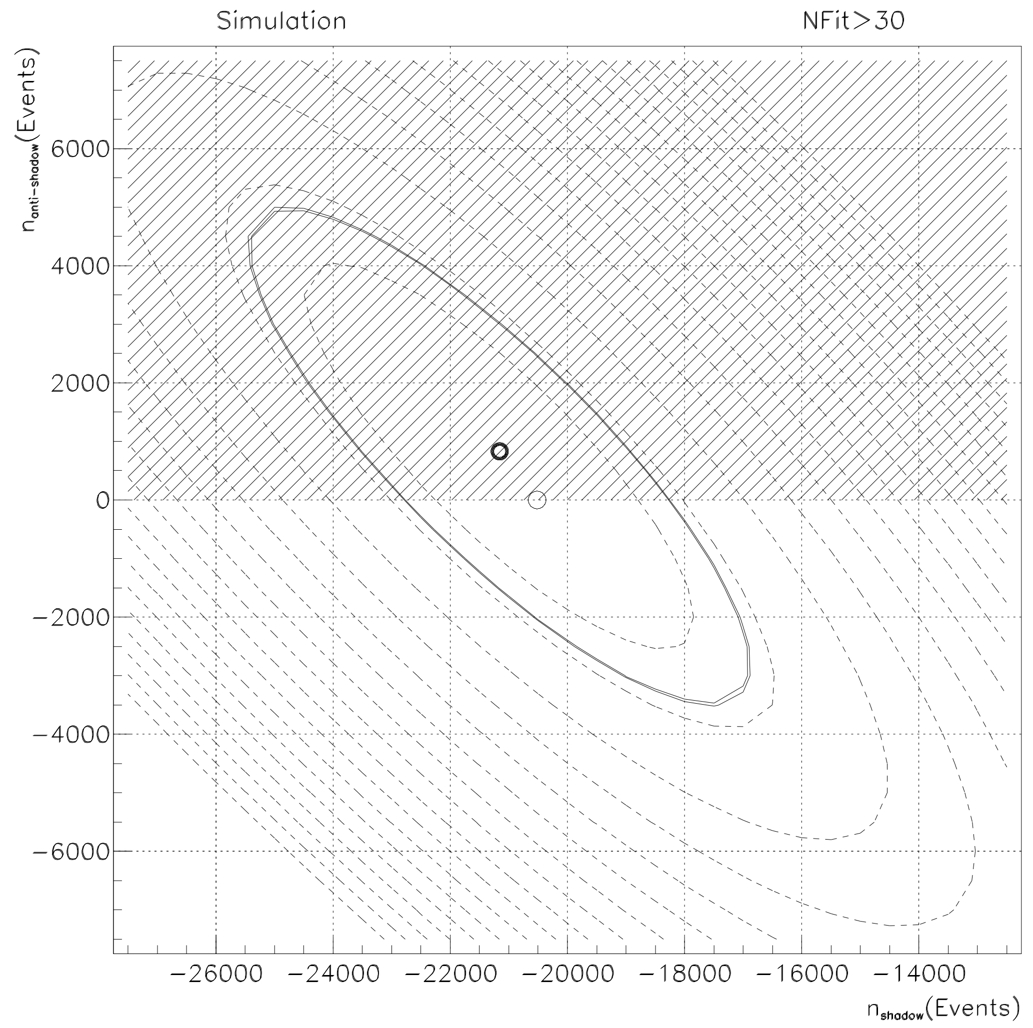

Figure 5.9: *Simulated $\overline{p}$ search.* Shown here are the contours of the logarithm of the likelihood ratio function for the simulated moon shadow, shown as a function of the number of events in the moon shadow deficit and the number of events in the moon anti-shadow deficit. In this plot, the unphysical region ($n_{anti-shadow} > 0$) is indicated by cross-hatching. The dark circle at (-21156, +830) is the global maximum of the likelihood function, and the lighter circle at (-20516,0) is the maximum in the physical region. The solid lines show the 95% confidence level contours, based on the locations of the maxima mentioned above. The dashed lines show the σ contours.

down to $n_{anti-shadow} = \sim -2400$ events. This is the 95% C.L. limit on the number of events in the anti-shadow deficit. Using this and the fact that the moon shadow contains -17834 ± 1785 events total, a 95% C.L. upper limit on the $\overline{p}/p$ ratio can be established. The 95% C.L. upper limit is $\sim$13% (=-2400/17834) on the $\overline{p}$/C.R. ratio, that is the ratio of $\overline{p}$sto all cosmic rays. Since the cosmic ray flux contains additional nuclear species, the limit on the $\overline{p}/p$ ratio must be larger than 13%. The simulations indicate that protons comprise 79% of the total moon shadow, or -14089 events. Using this number for n_{shadow} with the limit on $n_{anti-shadow}$ gives a 95% C.L. upper limit of 17% for $\overline{p}/p$.

Figure 5.9 shows the results of the $\overline{p}$ search performed on the simulated moon shadow. The maximum of $\log \mathcal{R}$ again appears in the non-physical region, but not as deep into it as in the data. This indicates that even with the correct shape of the deficit in the maximum likelihood function, there is still some interplay between the shadows. The two 95% C.L. contours practically overlap in this plot, and are therefore difficult to differentiate. They both set a limit of ~ -3500 events on $n_{anti-shadow}$. This yields a simulated 95% C.L. upper limit on the $\overline{p}/p$ ratio of 21%. The data give a slightly better upper limit on the $\overline{p}/p$ ratio because the position of the center of the shadow along the α-axis is displaced farther in the negative α direction in the data than in the simulation.

Figure 5.10 shows the results of the $\overline{p}$ search performed on the simulated moon shadow with a 15% anti-shadow mixed into the simulated moon shadow. The likeli-

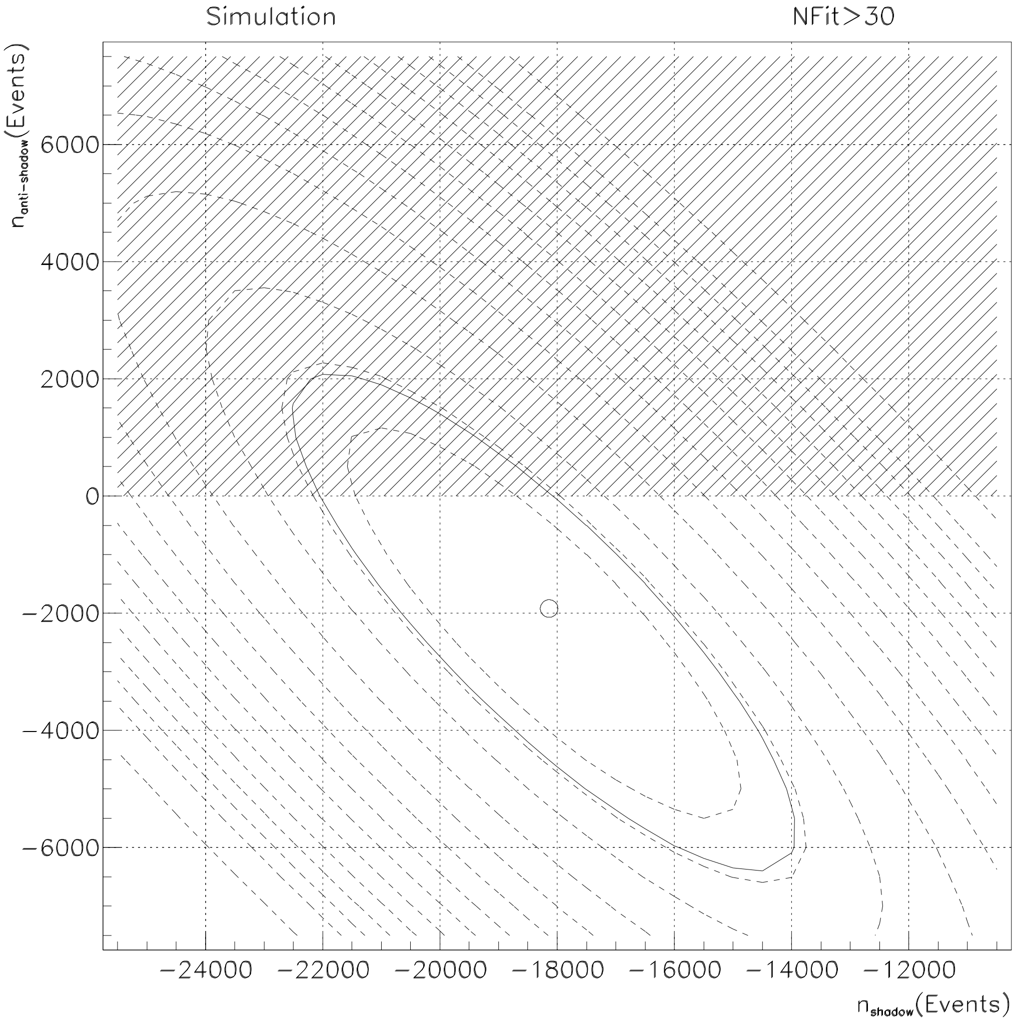

Figure 5.10: *Simulated $\overline{p}$ measurement.* Shown here are the contours of the logarithm of the likelihood ratio function for the simulated moon shadow, shown as a function of the number of events in the moon shadow deficit and the number of events in the moon anti-shadow deficit. A simulated anti-shadow was added to the simulated shadow, with the anti-shadow comprising 15% of the total deficit. In this plot, the unphysical region ($n_{anti-shadow} > 0$) is indicated by cross-hatching. The circle at (-18137,-1921) is the global maximum of the likelihood function. The solid line shows the 95% confidence level contour, based on the location of the maximum. The dashed lines show the σ contours. Using the results of this plot, the simulated $\overline{p}/p$ ratio measurement is 13%.

hood function is maximized at $(-18137, -1921)$, indicating that the maximum likelihood technique is capable of detecting an anti-shadow. With these numbers, the $\overline{p}/p$ measurement is 13%, whereas 15% was expected.

5.6 Comparison of results to existing limits

The observations of the moon and sun shadows in cosmic rays by the Tibet Collaboration are the only measurements that have been used to put a limit on the $\overline{p}/p$ ratio to date. Chantell *et al.* analyzed the Tibet moon shadow and established a 30% upper limit on the $\overline{p}$/(p+$\overline{p}$) ratio in $\sim$10 TeV cosmic rays [31]. Using the shadow of the sun, the Tibet Collaboration claimed an upper limit on the $\overline{p}/p$ ratio [32] in $\sim$10 TeV cosmic rays. Both of these results used non-quantitative arguments based on the appearance of the shadows to establish their limits.

Chantell *et al.* simulated the appearance of the moon shadow with varying levels of antimatter in the cosmic ray flux. A comparison was made between the position of the center of the observed moon shadow and the position of the center of the simulated shadow in plots similar to Figure 5.1, which combine simulated shadows and anti-shadows. Based on the comparisons, an upper limit of 30% on the $\overline{p}$/(p+$\overline{p}$) ratio was made for $\sim$10 TeV cosmic rays. This translates to an upper limit of 43% on the $\overline{p}/p$ ratio.

The Tibet result was based on a qualitative assessment of the appearance of the sun shadow. The center of the shadow of the sun was offset from the nominal (undeflected) position. Because there was no evidence of a comparable deficit deflected in the opposite direction from the nominal position, it was concluded that there was no anti-shadow. It was then reasoned that the $\overline{p}/p$ ratio was proportional to the ratio of the significances of the deficit at the center of the sun shadow and the oppositely deflected position. With an adjustment for the contribution of Helium nuclei, an upper limit of 22% was claimed on the $\overline{p}/p$ ratio for $\sim$10 TeV cosmic rays. This translates to an upper limit of 18% on the $\overline{p}$/(p+$\overline{p}$) ratio.

Neither result included a statement of the statistical confidence level. The Milagrito upper limit is stated at the 95% confidence level. The 95% C.L. upper limit of 17% on the $\overline{p}/p$ ratio for $\sim$3 TeV cosmic rays translates to a 95% C.L. upper limit of 15% on the $\overline{p}$/(p+$\overline{p}$) ratio.

Chapter 6

Sun Shadow Analysis

The sun has the same shadowing effect on the cosmic ray flux as it passes overhead as the moon does. Thus the shadow of the sun can be studied in the same way as the shadow of the moon. The sun shadow is more complicated, however, because of its complex magnetic field. The heliomagnetic field was not simulated, so the $\overline{p}$ search was not performed using the shadow of the sun.

6.1 The Sun's Movement In The Sky

The sun's position in the sky oscillates with a period of one year. This is illustrated in Figure 6.1. The plots show the zenith angle and declination of the sun as a function of time. Because of the motion of the sun's position and the geographic latitude of Milagrito, none of the data from the winter months is used in the shadow analysis, because the sun's altitude does not rise above 45° during these months.

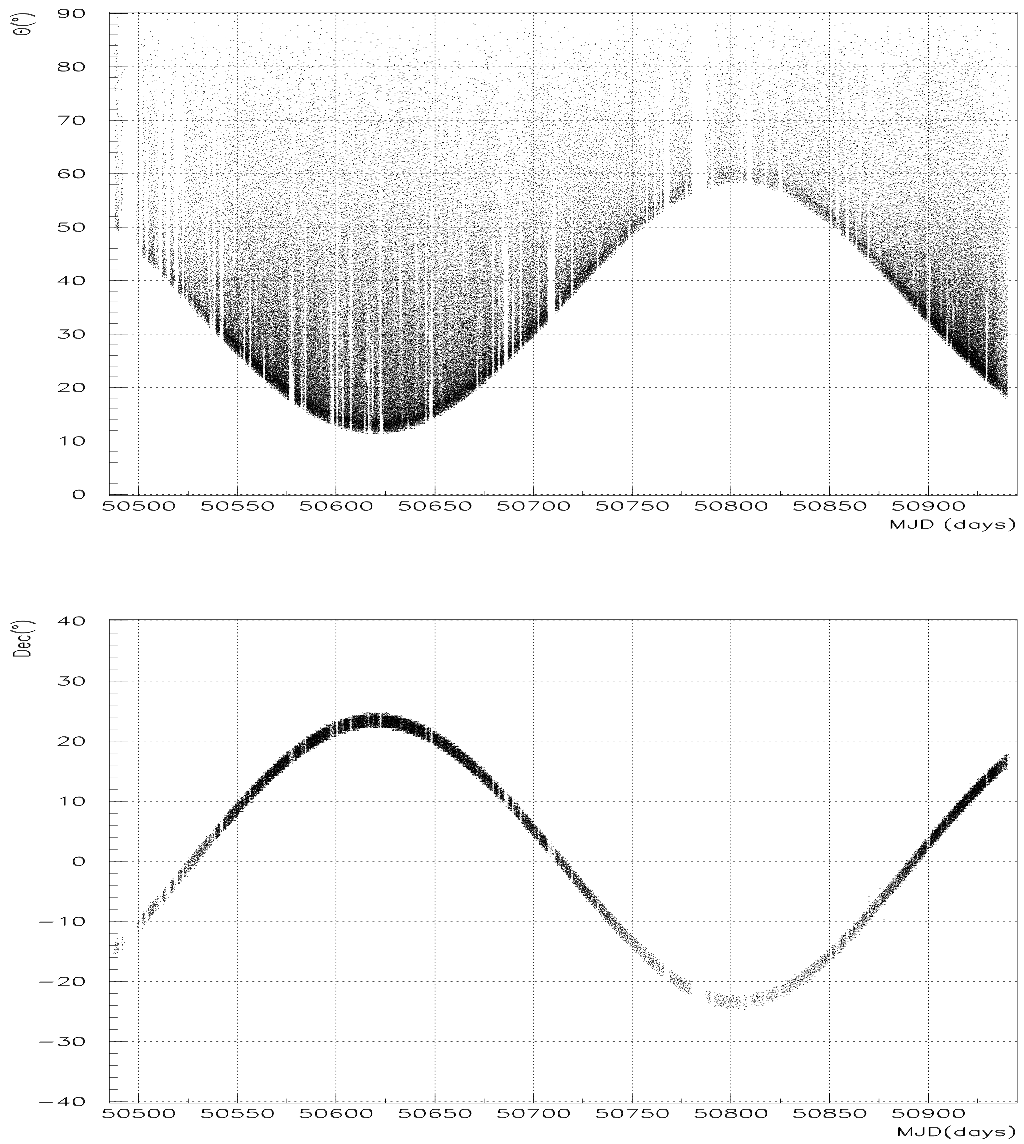

Figure 6.1: Zenith angle and declination of events from within 1° of the sun, shown as a function of modified Julian date, mjd. The minimum zenith angle (maximum altitude) of the moon varies sinusoidally with a period of one year. Note that during the winter, the maximum altitude of the sun does not go above 45°, so none of the data from these months is used in the shadow analysis.

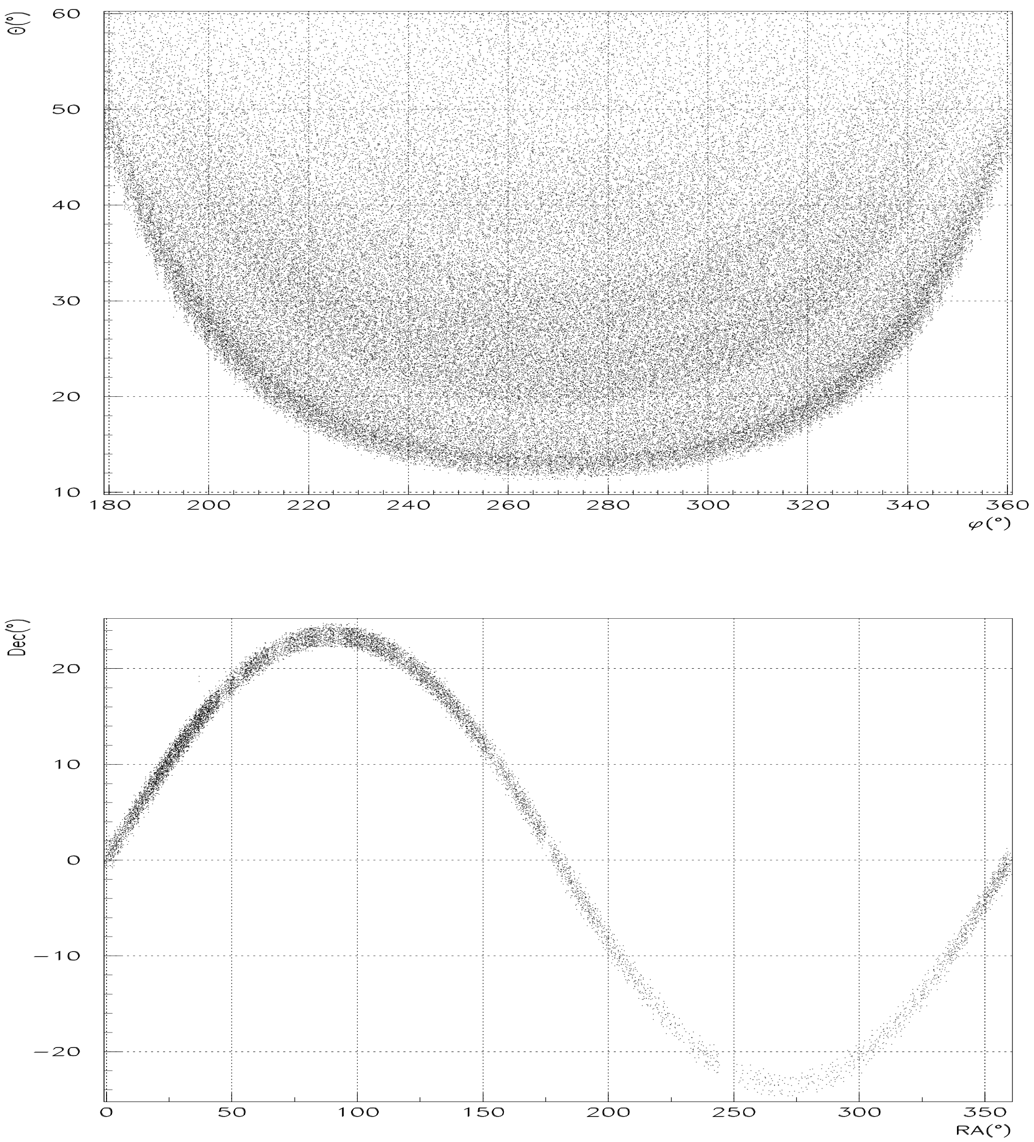

Figure 6.2: Angular distribution of events from within 1° of the sun, shown in θ versus ϕ, and δ versus α.

Figure 6.2 shows the angular distribution of events in $\theta-\phi$ space and $\delta-\alpha$ space. Compare these plots to Figure 4.2, and note that over the course of the year, the extremes of the sun's motion exceed the extremes of the moon's motion; the sun's altitude at transit rises higher in the sky than the moon's transit altitude during the summer, and the sun's altitude at transit is lower than the moon's transit altitude in the winter.

Figure 6.3 shows the angular distributions of the sun's position in each of the coordinates separately. These plots illustrate an artifact of the timing of Milagrito's observational lifetime: the sun went through $\sim 1 - 1/3$ periods of its motion while Milagrito was operational. This is seen clearly in the right ascension distribution. The motion of the sun is sinusoidal, which can be seen in the plot. But the amplitude of the sine wave from $0°$ to $\sim$50° is greater than the amplitude of the sine wave from $\sim$50° to 360°. This is because the sun traversed these positions in the sky (α=0°-50°) twice, while it passed through the rest of the sky only once. This is similarly seen in the declination and zenith angle plots. Both histograms show a bump somewhat below the sun's maximum altitude. This is because Milagrito was turned off in the spring of 1998, before the sun's position reached maximum altitude. Thus the second fraction of a period of the sun's motion did not include the time when the sun's altitude was at maximum. This means that the sun spent more time in the sky at lower altitudes during Milagrito's lifetime; Milagrito therefore observed more events from the direction of the sun while it was between 20° and 40° in θ than when it was

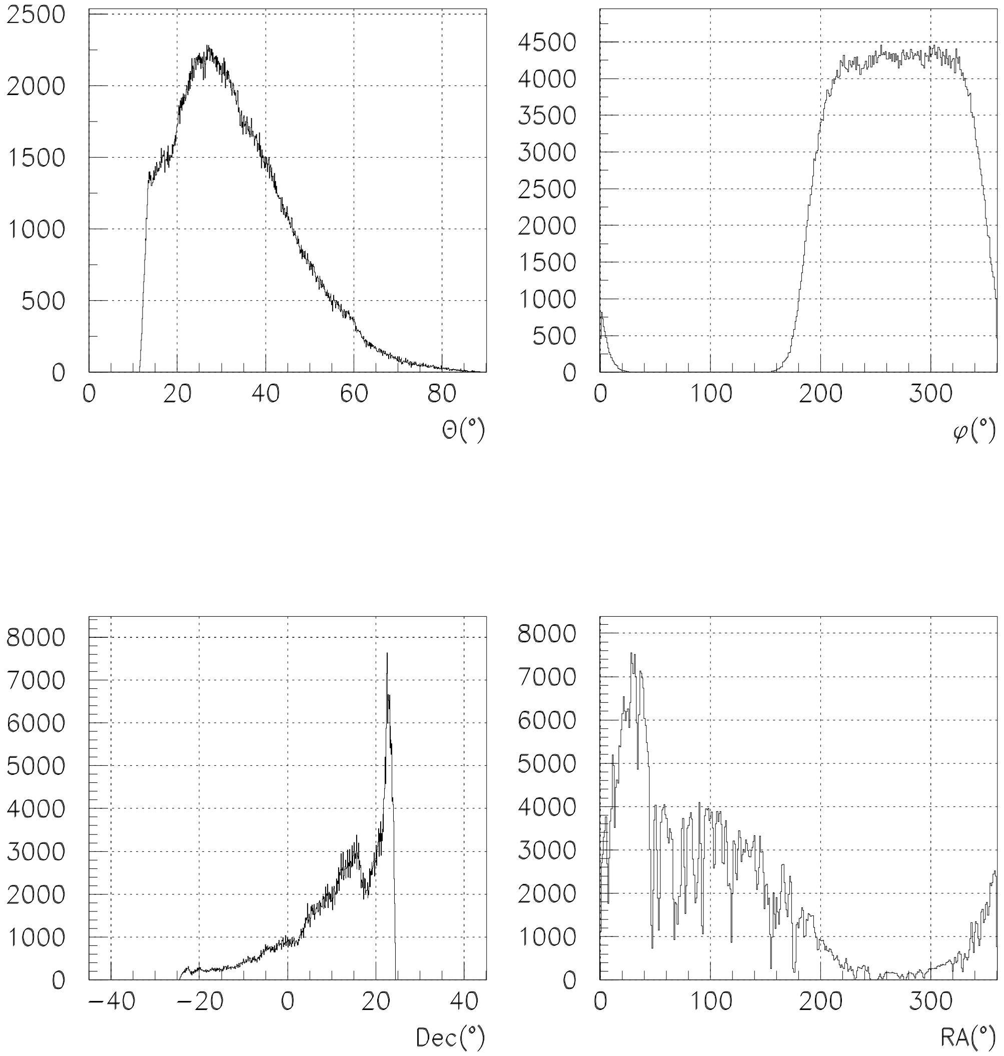

Figure 6.3: Angular distribution of events from within 1° of the moon. The top plots show the events in zenith angle, θ, and azimuthal angle, ϕ. The bottom plots show the events in declination and right ascension.

below θ=20°(or above altitude=70°). Note also that the increase in the number of events from the spring of 1998 more than doubles the previous numbers, because the event rate was higher at that time than it was in 1997 due to the increased water depth. (See Figure 2.6.)

This artifact of the timing of Milagrito's observations is not seen in the ϕ distribution in Figure 6.3. This is because the sun passed across the sky nearly uniformly in azimuth day after day, with the distribution only minimally affected by the altitude of the sun.

6.2 The Sun Shadow

The shadow of the sun was analyzed in the same manner that the moon shadow was analyzed. The methods are described in Chapter 4. Figure 6.4 shows the smoothed significance maps of the sun shadow. The figure shows the sun shadow corrected for the $\Delta\theta$ systematic pointing error, and uncorrected. The $\Delta\theta$ correction shifts the center of the deficit up in declination, and tightens the shadow. The significance of the deficit for NFit>30 is 10.1σ.

Figure 6.5 shows the significance of the sun shadow in four different bands of NFit. These plots show the $\Delta\theta$-corrected data. The position of the center of the deficit for each NFit band is given in Table 6.1.

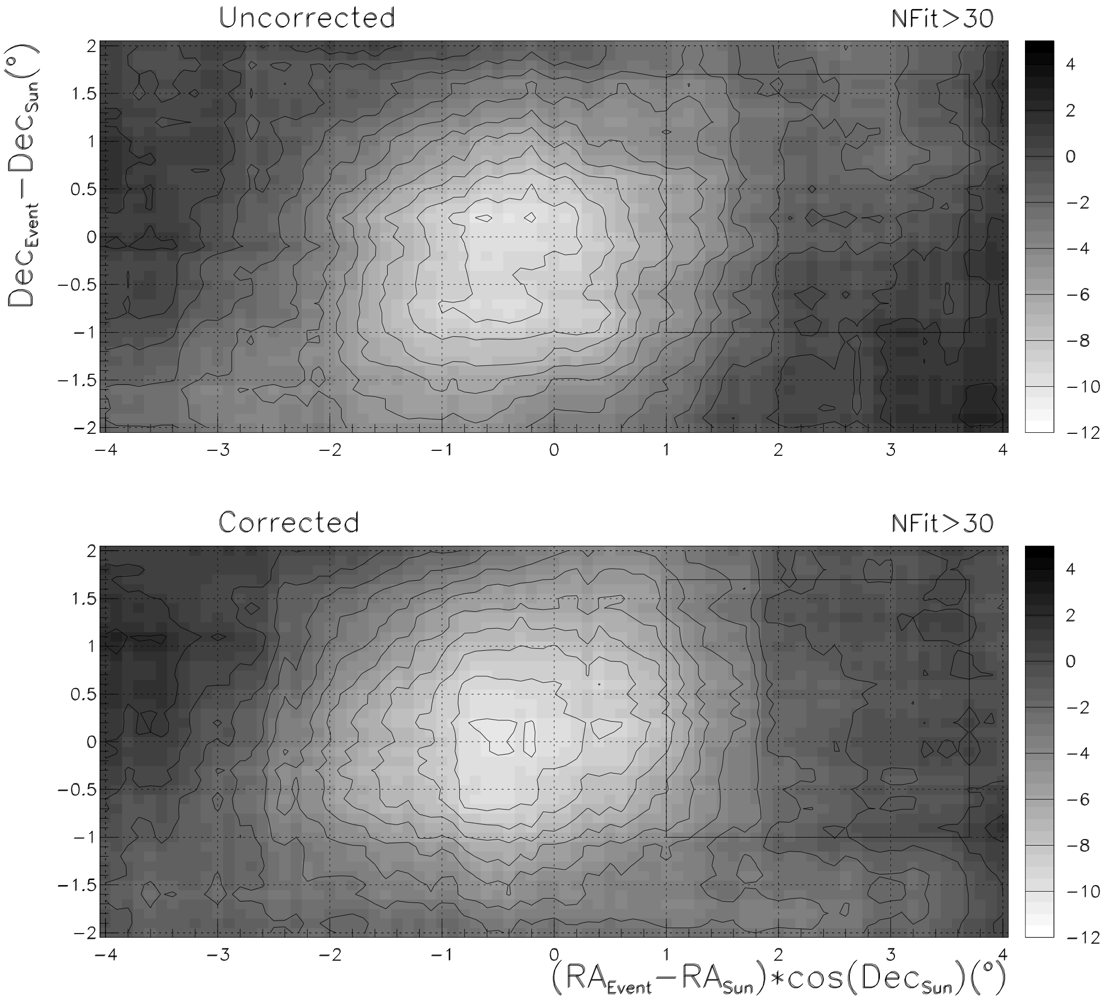

Figure 6.4: Significance of Milagrito sun shadow. Both plots are comprised of data up to $\theta = 45°$. The data were corrected for the $\Delta\theta$ *versus* θ offset, event by event, in the bottom plot. The upper plot is uncorrected. Both plots were smoothed using a square bin 2.1°on a side. The grey-scale given on the right of each plot indicates the significance in each 0.1°×0.1° bin.

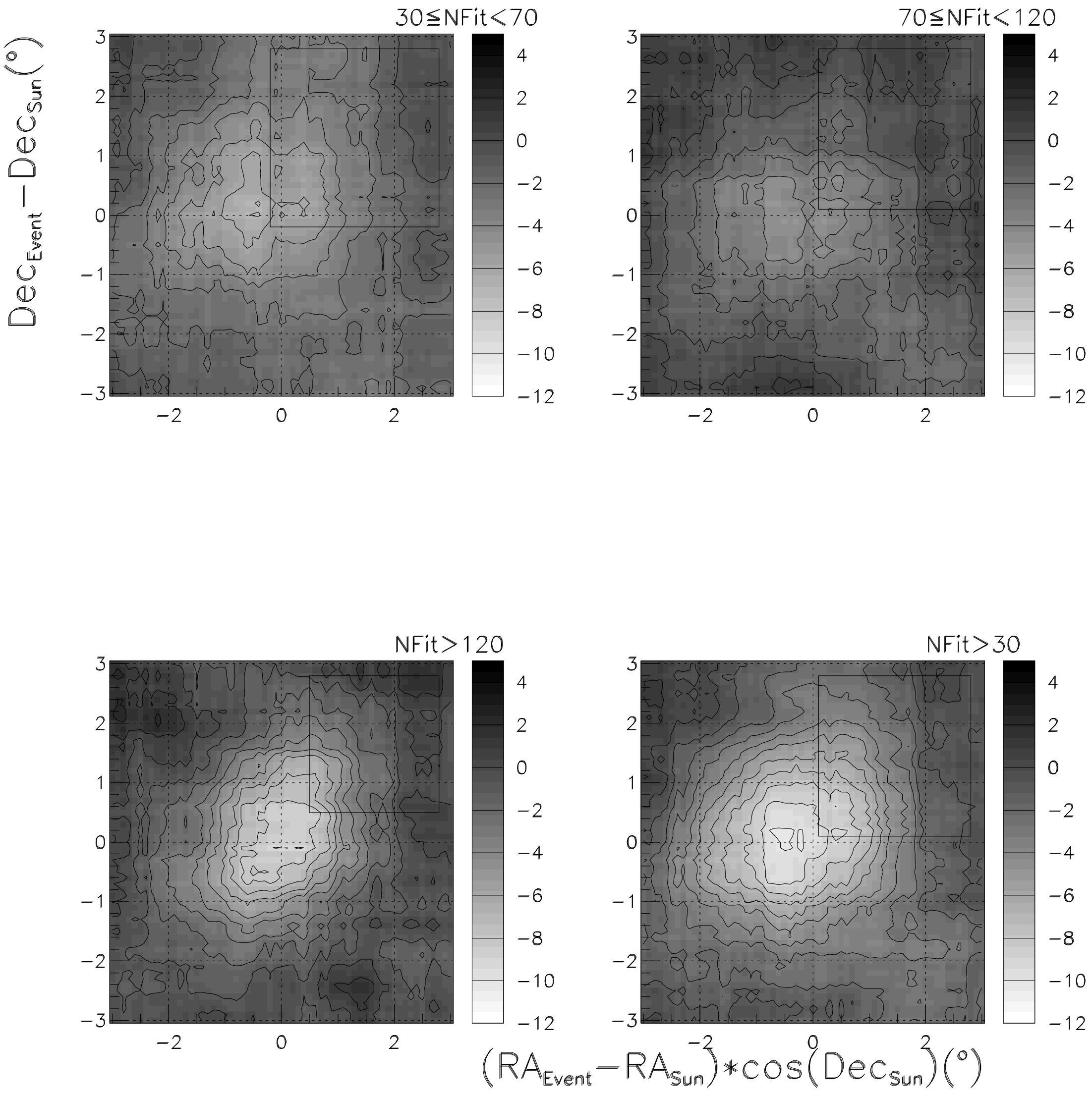

Figure 6.5: Significance of Milagrito sun shadow. The data were corrected for the $\Delta\theta$ *versus* θ offset, and are shown in four different bands of NFit. The grey-scale given on the right of each plot indicates the significance in each $0.1^\circ \times 0.1^\circ$ bin.

Sun Shadow Results			
Input	*NFit range*	*α offset*	*δ offset*
Simulation	30-69	-0.29°±0.81°	+0.45°±1.20°
Simulation	70-119	-0.43°±0.28°	-0.02°±0.27°
Simulation	120+	-0.14°±0.08°	+0.01°±0.08°
Simulation	30+	-0.19°±0.19°	+0.14°±0.19°
Data	30-69	-0.38°±0.37°	+0.20°±0.39°
Data	70-119	-0.29°±0.39°	-0.06°±0.36°
Data	120+	-0.09°±0.12°	-0.10°±0.13°
Data	30+	-0.29°±0.17°	+0.00°±0.17°

Table 6.1: Position of the Milagrito sun shadow.

6.3 Simulation

The heliomagnetic field was not simulated, so a true simulation of the Milagrito sun shadow could not be made. But a simulation of the shadow of the sun in the absence of heliomagnetic field effects was made. The results are shown in Figure 6.6 and the position of the center of the deficit of the simulated sun shadow is given in Table 6.1. The shadow is shown in four different bands of NFit. Note that the location of the center was found using projections of the skymaps, not the maximum likelihood method. This is because the shape of the simulated shadow is not expected to match the observed shadow, because the heliomagnetic field was not simulated. Although Milagrito ran during the solar minimum period and the position of the sun shadow was not expected to be shifted noticeably by the heliomagnetic field [48], there should still be some effect on the shape of the shadow. Since the maximum likelihood method relies heavily on the shape of the simulated shadow, it was not

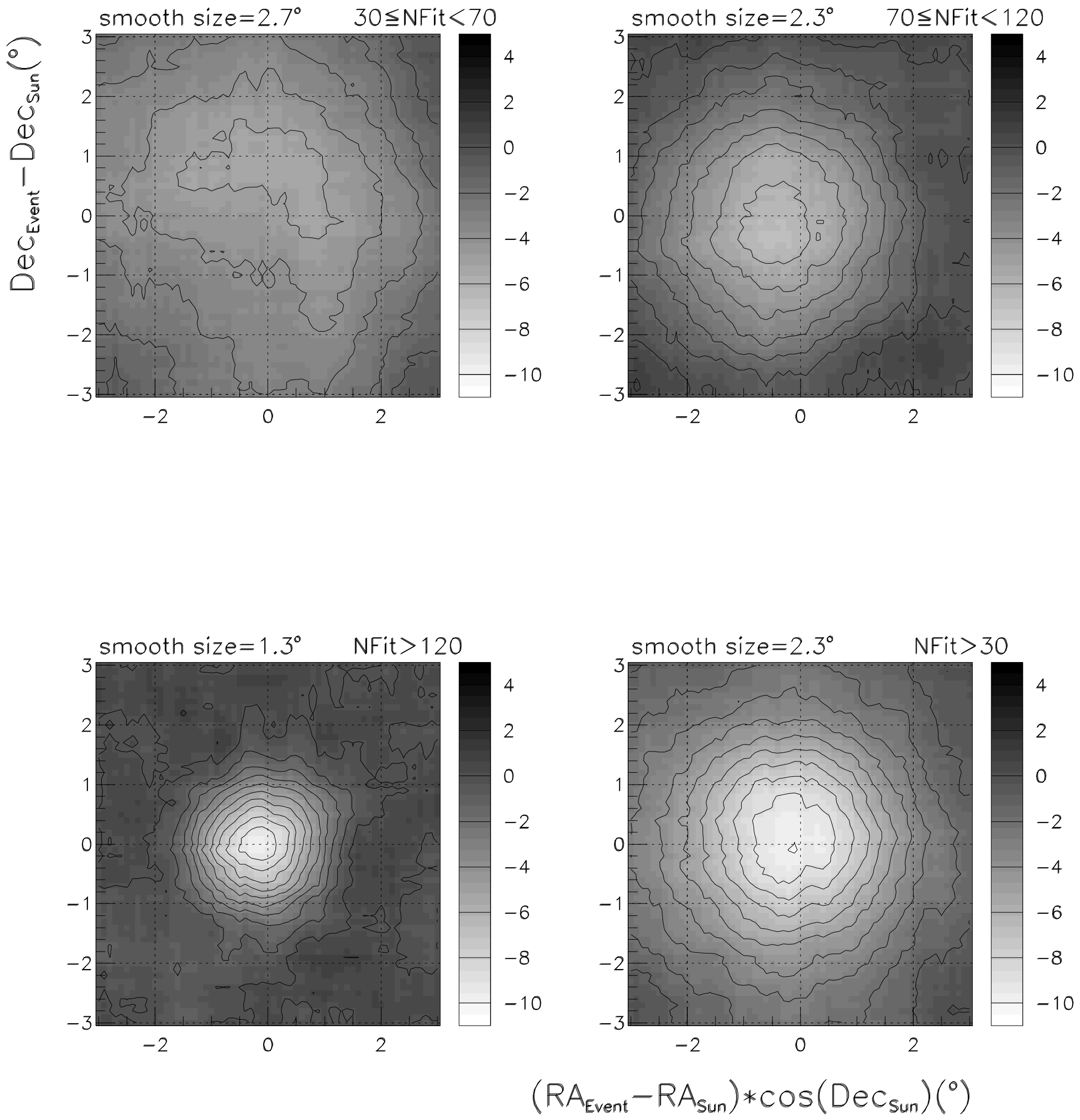

Figure 6.6: Simulated Milagrito sun shadow, shown for different nFit bands. The grey-scale given on the right of each plot indicates the significance in each $0.1° \times 0.1°$ bin.

suited to the analysis of the sun shadow without a full simulation that included the heliomagnetic field.

Table 6.1 indicates that the location of the center of the deficit does not differ significantly between the simulated shadow and the observed shadow. This confirms the expectation that the position should not be affected greatly by the heliomagnetic field since the observation was made during solar minimum [48]. But because the sun shadow is expected to be deflected less in α by the geomagnetic field, it is not as useful for the $\overline{p}$ search as the moon shadow. Considering this, and the fact that shape of the sun shadow is not expected to match the simulated shape, the $\overline{p}$ search was not done with the shadow of the sun.

Chapter 7

Conclusions

The study of the shadow of the moon in cosmic rays has been a useful tool for EAS arrays for many years. The Milagrito moon shadow has proven just as useful for the same purposes. But because Milagrito's energy range was lower than in previous EAS arrays, and with the use of a powerful analysis method, a new limit on the amount of antimatter in the cosmic ray flux has come from the study of the moon shadow.

7.1 Moon Shadow

The shadow of the moon was observed with the Milagrito detector at the 10.2σ level. Simulations indicate that the median energy of detected cosmic rays from the direction of the moon is 2.7 TeV.

7.1.1 Angular Resolution

The width of the moon shadow can be used to give a measure of the average angular resolution of the detector, although the true angular resolution of Milagrito is quite complex. The simulations indicate that the angular resolution is a strong function of NFit. Nevertheless an average angular resolution can be determined from the width of the moon shadow. By fitting the projections of the moon shadow deficit to Gaussian functions, the average angular resolution of Milagrito is estimated to be $0.90^\circ \pm 0.11^\circ$.

The ability to accurately reconstruct air showers with an EAS array depends on the ability to determine the position of the core of the shower. Because the size of the Milagrito pond was much smaller than the average lateral size of an air shower, the core resolution was poor. This caused Milagrito's angular resolution to be so poor. A new core-finding algorithm has been developed for the Milagro detector which can determine if the core of a shower impacted the ground away from the pond. This will greatly improve the core resolution, and therefore the angular resolution. More importantly, Milagro will be augmented with an array of outrigger detectors, which will aid in the core position measurement.

7.1.2 Systematic Pointing Errors

The position of the moon shadow can be used to test the pointing ability of EAS arrays. If the position of the shadow is significantly offset from the expected position, the difference can be attributed to a systematic bias in the reconstruction of air shower events. Such an effect was seen in the Milagrito data. The effect, described in detail in Section 3.2.2, caused the position of the moon shadow to be shifted downward on the δ axis. An offline correction based on Monte Carlo events was developed and applied to the data which worked adequately.

The Milagro detector was designed with conical baffles outfitted on every PMT. The baffles are mounted so that the cone opens upward, with the PMT situated in the apex, face-up. The inside of the baffle is silvered, and the outside is opaque. Thus light incident on the outside of the baffle is absorbed by the baffle, but light incident on the inside of the baffle is reflected into the PMT. This means that the PMTs are no longer triggered by horizontal light, and the collection area of each PMT as seen from above is increased. This has eliminated the cause of the systematic pointing error in Milagro. The Milagro moon shadow is consequently expected to be not offset on the δ axis the way the Milagrito moon shadow was before the application of the $\Delta\theta$ correction. The observed Milagro moon shadow shows no net defecletion in δ, as expected.

7.1.3 Energy Scale

The position of the moon shadow is expected to be shifted noticeably at TeV energies due to the effects of the geomagnetic field. This was observed in the Milagrito moon shadow. The amount of deflection depends on the energies of the cosmic ray primaries, and on the magnetic field itself. Comparison of the simulations with the Milagrito data gives a check on the consistency of the two. By adjusting the energies of the simulated primaries, the energy dependence of the position of the shadow can be tested. Using this technique, the Milagrito moon shadow gives a range of consistency of $\pm 85\%$ on the overall energy scale.

7.1.4 Antiproton Limit

By examining the Milagrito data for the presence of a second shadow, a search for an antimatter component of the cosmic ray flux can be made. The observations of the moon shadow with Milagrito showed no evidence of an anti-shadow, and established a 95% C.L. upper limit on the $\overline{p}/p$ ratio of 17% in cosmic rays of median energy 2.7 TeV. This limit translates to a 95% C.L. upper limit of 15% on the $\overline{p}/(\mathrm{p}+\overline{p})$ ratio in cosmic rays of median energy 2.7 TeV.

7.2 Sun Shadow

The shadow of the sun was observed at the 10.1σ level. The sun was in the solar minimum period during Milagrito's lifetime; the position of the center of the observed deficit did not differ significantly from expectations, indicating that the heliomagnetic field did not influence the position greatly.

Bibliography

[1] Cy Hoffman, personal communication.

[2] J.A. Simpson *et al.*. *Annual Rev. Nucl. Part. Sci.*, 33:323, 1983.

[3] C. Caso *et al.*. *Eur. Phys. J.*, 15, 2000.

[4] V.F. Hess. *Physics Z.*, 13:1084, 1912.

[5] T. Grivet-Mayer P. Auger, R. Maze. *C. R. Acad. Sci.*, 206:1721, 1938.

[6] M.S. Longair. *High Energy Astrophysics, Vol. 2, 2nd Ed.* Cambridge University Press, Cambridge, England, 1992.

[7] J.M. Ryan. *Proc. 26th ICRC*, SH:1.7.02, 1999.

[8] E. Fermi. *Nuclear Physics, compiled by Orear* et al.. University of Chicago Press, Chicago, IL, 1949.

[9] E. Fermi. *Phys. Rev.*, 75:1169, 1949.

[10] Thomas K. Gaisser. *Cosmic Rays and Particle Physics.* Cambridge University Press, Cambridge, England, 1990.

[11] Bruno Rossi. *High-Energy Particles.* Prentice Hall, New York, 1952.

[12] Tom Yang. *Search for High-Energy Emission from Gamma-Ray Bursts with a Large Water Cherenkov Detector.* PhD thesis, University of California, Santa Cruz, 1998.

[13] J.H. Hubbell *et al.*. *J. Phys. Chem. Ref. Data*, 9:1023, 1980.

[14] P. Cherenkov. *Phys. Rev.*, 52:378, 1937.

[15] J.D. Jackson. *Classical Electrodynamics.* Wiley & Sons, New York, 1975.

[16] Kenneth Greisen. *Ann. Rev. of Nucl. Sci.*, 10:63–108, 1960.

[17] D. E. Alexandreas *et al.*. *Nucl. Instr. and Meth.*, A311:350, 1992.

[18] M. Amenomori *et al.*. *Nucl. Instr. and Meth.*, A 288:619, 1990.

[19] T.C. Weekes. *Phys. Reports*, 160:1–121, 1988.

[20] G.W. Clark. *Phys. Rev. D*, 43:1735, 1957.

[21] D. E. Alexandreas *et al.*. *Phys. Rev. D*, 43:1735, 1991.

[22] M. Amenomori *et al.*. *Phys. Rev. D*, 47:2675, 1993.

[23] S. Orito *et al.*. *Phys. Rev. Lett.*, 84:1078, 2000.

[24] R.L. Golden S.A. Stephens. *Space Sci. Rev.*, 46:31–91, 1987.

[25] S.A. Stephens. *Proc. 18th ICRC*, 9:167, 1983.

[26] S.A. Stephens. *Astron. Astrophys.*, 149:1, 1985.

[27] M. Boezio *et al.*. *Astrophys. J.*, 487:415, 1997.

[28] R. Battiston, Feb. 1999. arXiv:astro-ph/9907152.

[29] S.P. Ahlen *et al.*. *Nucl. Instr. Meth.*, A 350:351, 1994.

[30] The AMS Collaboration. submitted to Phys. Lett. B. arXiv:hep-ex/0002048.

[31] M. Chantell *et al.*. *Nature*, 367:25, 1994.

[32] M. Amenomori *et al.*. *Proc. 24th ICRC*, 3:84, 1995.

[33] D. Pomarède *et al.*. *Astopart. Phys.*, 14:287–317, 2001.

[34] R. Biona *et al.*. *Phys. Rev. Lett.*, 51:27, 1983.

[35] *et al.*G.E. Allen. *Proc. 24th ICRC*, 1:914, 1995.

[36] R. Atkins *et al.*. *Nucl. Instr. and Meth.*, A449:478, 2000.

[37] Isabel Leonor. *Search for a TeV Component of Gamma-Ray Bursts Using the Milagrito Detector*. PhD thesis, University of California, Irvine, 2000.

[38] J. Knapp and D. Heck. *Extensive Air Shower Simulation with CORSIKA: A User's Guide*. Institut für Kernphysik, Forschungszentrum Karlsruhe, 1997.

[39] D. Heck *et al.*. *"CORSIKA: A Monte Carlo Code to Simulate Extensive Air Showers," tech report FZKA 6019.* Institut für Kernphysik, Forschungszentrum Karlsruhe, 1998.

[40] CORSIKA is available from its authors (`auth@ik3.fzk.de`).

[41] K. Werner. *Phys. Reports*, 232:87, 1993.

[42] GEANT C.P.L. *GEANT Reference Manual, Version 3.21.* CERN, Geneva, Switzerland, 1994.

[43] D. E. Alexandreas *et al.*. *Nucl. Instr. and Meth.*, A328:570, 1993.

[44] `http://www.ngdc.noaa.gov/seg/potfld/DoDWMM.shtml`.

[45] W. Kinnison. *A Search for* $\mu^+ \to e^+\gamma$. PhD thesis, University of Chicago, 1979.

[46] W.T. Eadie *et al.*. *Statistical Methods in Experimental Physics.* North Holland, Amsterdam and London, 1971.

[47] L. Lyons. *Statistics for Nuclear and High Energy Physicists.* Cambridge University Press, Cambridge, England, 1986.

[48] M. Amenomori *et al.*. *Astrophys. J.*, 541:1051–1058, 2000.